DEVELOPMENT OF A LAMINAR NAVIER-STOKES SOLVER FOR INCOMPRESSIBLE FLOWS USING STRUCTURED GRIDS

A THESIS SUBMITTED TO
THE GRADUATE SCHOOL OF NATURAL AND APPLIED SCIENCES
OF
MIDDLE EAST TECHNICAL UNIVERSITY

BY

AYHAN AKIN

IN PARTIAL FULFILLMENT OF THE REQUIREMENTS
FOR
THE DEGREE OF MASTER OF SCIENCE
IN
MECHANICAL ENGINEERING

APRIL 2006

Approval of the Graduate School of Natural and Applied Sciences

Prof.Dr. Canan Özgen
Director

I certify that this thesis satisfies all the requirements as a thesis for the degree of Master of Science

Prof.Dr. S. Kemal İder
Head of Department

This is to certify that we have read this thesis and that in our option it is fully adequate, in scope and quality, as a thesis for the degree of Master of Science.

Prof. Dr. M. Haluk Aksel
Supervisor

Examining Committee Members

Prof.Dr. Zafer Dursunkaya (METU, ME)

Prof.Dr. M. Haluk Aksel (METU,ME)

Prof.Dr. İ. Sinan Akmandor (METU, AEE)

Asst.Prof.Dr. Cüneyt Sert (METU, ME)

Asst.Prof.Dr. Tahsin Çetinkaya (METU, ME)

I hereby declare that all information in this document has been obtained and presented in accordance with academic rules and ethical conduct. I also declare that, as required by these rules and conduct, I have fully cited and referenced all material and results that are not original to this work.

Name, Last Name:

Signature:

ABSTRACT

DEVELOPMENT OF A LAMINAR NAVIER-STOKES SOLVER FOR INCOMPRESSIBLE FLOWS USING STRUCTURED GRIDS

Akın, Ayhan
M. S., Department of Mechanical Engineering
Supervisor: Prof. Dr. M. Haluk Aksel

April 2006, 126 Pages

A method to solve the Navier-Stokes equations for incompressible viscous flows is proposed. This method is SIMPLE (Semi-Implicit Method for Pressure Linked Equations) algorithm to iteratively solve the two-dimensional laminar steady momentum equations and based upon finite volume method on staggered grids. Numerical tests are performed on several cases of the flow in the lid-driven cavity, as well as of the flow after a backward-facing step with SIMPLE and SIMPLER (SIMPLE Revised) methods. Finally, results are compared qualitatively and

quantitatively with numerical and experimental results available in the literature for different Reynolds numbers to validate the methods.

Keywords: Navier-Stokes Equations, Incompressible Flows, SIMPLE Method, Finite Volume Method, Lid-driven Cavity, Backward-facing Step.

ÖZ

YAPILANDIRILMIŞ AĞLAR KULLANILARAK SIKIŞTIRILAMAYAN AKIŞLAR İÇİN LAMİNAR NAVIER-STOKES ÇÖZÜCÜNÜN GELİŞTİRİLMESİ

Akın, Ayhan
Yüksek Lisans, Makina Mühendisliği Bölümü
Tez Yöneticisi : Prof. Dr. M. Haluk Aksel

Nisan 2006, 126 Sayfa

Sıkıştırılamayan viskoz akışkanların Navier –Stokes denklemlerini çözmek için bir yöntem önerilir. Bu yöntem iki boyutlu laminar değişmeyen momentum denklemlerini tekrarlayarak çözen SIMPLE (Semi-Implicit Method for Pressure Linked Equations) algoritmasıdır ve karşı karşıya gelmeyecek şekilde yapılandırılmış ağlar üzerindeki sonlu hacim yöntemine dayanır. Sayısal testler kapağın sürüklediği boşluğun içindeki akışlar gibi arkaya bakan basamağın sonrasındaki akışların farklı durumları için SIMPLE ve SIMPLER (SIMPLE Revised) yöntemleri ile yapılır. Sonunda, sonuçlar bu yöntemleri onaylamak için nitel ve nicel olarak farklı Reynolds sayılarında literatürde bulunan sayısal ve deneysel sonuçlarla karşılaştırılır.

Anahtar Kelimeler: Navier-Stokes Denklemleri, Sıkıştırılamayan Akışlar, SIMPLE Yöntemi, Sonlu Hacimler Yöntemi, Kapağın Sürüklediği Boşluk, Arkaya Bakan Basamak.

ACKNOWLEDGEMENTS

I would like to express my gratitude to my parents, M. Bilge Akın and Sebahhattin Akın for their unfailing and loving support, financial supports and prayers to overcome many difficulties.

I would like to express my sincere appreciation to my thesis advisor, Prof. Dr. M. Haluk Aksel for his guidance, support during my research on this thesis. His ideas, discussions, wonderful advices play a very important role in the accomplishing this work. Also, I would like to express my deepest gratitude to Dr. İ. Sinan Akmandor, best teacher of my university life, for his helps to improve my skills and for his trusts thought my career.

My special thanks go to my unforgettable friends, Barbaros, Ender, Evren, Fuat, Mehmet, Serkan, Sertan, Volkan, to my squash partner, Hüseyin for their encouragements, supports, interests and helps. It is not possible to get more friendship than they provided to me.

I would like to thank my manager Mr. Nahit Kahraman from Zorlu Industrial and Energy for encouraging me to complete my studies, my director Mr. Vedat Gülen for giving permission to focus on my thesis. and Mr.Ayhan Arı for his supports and encouragements.

Many thanks to the Aerospace Engineering Department for computing support and to graduate assistant Mustafa Kaya for practical and scientific recommendations.

TABLE OF CONTENTS

LIST OF TABLES

TABLES

LIST OF FIGURES

FIGURES

LIST OF SYMBOLS

SYMBOLS

a	Coefficient of Discretisation Equation
A	Area
b	Mass source Term
b'	Mass Source Term in the Pressure Correction Equation
d	d-term in Pressure Correction Equation
D	Diffusion Conductance
F	Convective Mass Flux per Unit Area
h	Step height
H	Channel height
i	Specific Energy
k	Thermal Conductivity Coefficient
L	Width of the Cavity
$\max$	Maximum Value
$\bar{n}$	Normal Vector to the Wall
p	Pressure
p^*	Guessed Pressure Field
p'	Pressure Correction
Pe	Local Grid Peclet Number
Re	Reynolds Number
S	Source
t	Time Variable
T	Temperature
u	Velocity in x-Direction
u^*	Guessed Velocity in x-Direction

u' Velocity Correction in *x*-Direction

$\hat{u}$ Pseudo-Velocity in *x*-Direction

U_{avg} Average Inlet Velocity

U_{lid} Velocity of the Upper Lid

v Velocity in *y*-Direction

$v*$ Guessed Velocity in *y*-Direction

v' Velocity Correction in *y*-Direction

$\hat{v}$ Pseudo-Velocity in *y*-Direction

V Velocity Vector

w Velocity in *z*-Direction

x, y, z Cartesian Coordinates

x_L Channel Length

OTHER SYMBOLS

ρ Density

Γ Diffusion Coefficient

δ Displacement

μ Dynamic Coefficient of Viscosity

η Expansion Ratio

∇ Gradient Operator

ϕ General Flow Dependent Variable

α Parameter for Diffusion in QUICK scheme

λ Second Coefficient of Viscosity

τ Shear Stress

ΔV Volume

SUBSCRIPTS

1	Lower Attachment Point
2	Upper Detachment Point
3	Upper Attachment Point
E	East Side Node
EE	East Side Upstream Node
e	East Side Control Volume Face
i	Velocity Grid Point in x-Direction
I	Scalar Node in x-Direction
J	Total Flux
j	Velocity Grid Point in y-Direction
J	Scalar Node in y-Direction
n	North Side Control Volume Face
N	North Side Node
nb	Neighbor Cells
P	General Nodal Point
S	South Side Node
s	South Side Control Volume Face
u	x (Axial) Component
v	y (Tangential) Component
W	West Side Node
WW	West Side Upstream Node
w	West Side Control Volume Face

CHAPTER 1

INTRODUCTION

1.1 General

Over the last two or three decades; the need for the prediction of complex fluid flows arises in numerous engineering problems. Simulations of these flows can be overcome by mainly two ways. These are experimental calculation and theoretical formulation. Experimental investigations are preformed on both full-scale and small-scale models. In most cases, full-scale tests are impossible and significantly expensive. In addition to this, experiments on small-scale models can not exactly match with the full-scale models and decrease the usefulness of tests. Therefore, unlike experimental calculation, theoretical formulation is used widely in the industry having interest in fluid flow engineering. In theoretical investigation; mathematical model of the physical problems is examined. Mathematical model involves sets of differential equations which are governing fluid flows. If these equations can be solved by any numerical method, many physical phenomena in practical engineering problems can be predicted by means of computer-based simulation.

Most useful technique in a wide range of commercial areas is Computational Fluid Dynamics or CFD. CFD is the simulation of the fluid flows in engineering systems by using modeling and numerical methods. CFD codes are developed to solve the discretised governing equations according to reasonable numerical algorithms. Fluid flow problems can be tackled by these commercial CFD codes. The development of the CFD codes involves three stages.

First stage is the input of a flow problem. The physical problem to be modeled is selected. Then the geometry of the computational domain and fluid properties are defined in that domain. Grid is generated over the computational domain in order to sub-divide the domain into a number of non-overlapping sub-domains. Then numerical solution technique is applied to approximate the unknown flow variables in the discretised governing equations by means of mathematical applications. Finite volume method is one of the ways to approximate unknown fluid flow variables by special finite difference formulation. Finite volume method, which is the conservation of a general flow variable ϕ within the finite control volume, is used in this thesis and explained in Chapter 3 in detail. After obtaining the set of equations, some iterative solution algorithm is needed since the obtained mathematical model is non-linear and complex.
Finally, the last stage is the visualization of the obtained results. Output of the CFD code is displayed in order to evaluate the solved fluid flow.

1.2 Convection and Diffusion Transport Mechanisms

All fluid flow properties are transported by the effect of convection and diffusion. Therefore, mathematical modeling of the fluid flow deals with the general transport equation consisting these two transport terms. Most significant case is to successive modeling of the flow when both convection and diffusion affect the flow domain. Since the effects of the cross-wise convection-diffusion should be considered accurately in this case.

1.3 Incompressible Navier-Stokes Equations

The motion of the fluid particles can be described by Navier-Stokes equations. These are the continuity equation and the non-linear transport equations for conservation of momentum. For incompressible flows, Navier-Stokes equations do not provide an independent equation for pressure and also, continuity equation can not be used directly for calculation of pressure field.

1.4 Methods for Solving Incompressible Viscous Flow

Solving compressible Navier-Stokes equations is not simple since the mass and momentum conservation equations are coupled with the energy equation with help of the equation of state. On the other hand, solving incompressible Navier-Stokes equations is not also straightforward but rather difficult. Although the coupling of the energy equation to the mass and momentum equations does not exists anymore, the real complexity in solving incompressible flow equations comes out in the methodology of coupling the mass and momentum conservation equations and the calculation of the converged pressure field iteratively. If the correct pressure field is obtained, to calculate the velocity field is not difficult since pressure gradient is the term of the momentum equation and velocity field can be determined by the momentum equation for a given pressure field. There is not any equation for determining the correct pressure field directly. Since, the effect of the pressure field on the mass conservation is indirect that when the momentum equations are solved for the correct pressure field, resulting velocity field also satisfies the mass conservation. [3]

There are two approaches for solving the incompressible Navier-Stokes equations.

- Vorticity / stream function approach
- Primitive variables formulation

The methodology of the first approach is based on a stream function-vorticity formulation of the two-dimensional steady-state Navier-Stokes equations representing the incompressible fluid flows in two-dimensional domains [4]. Firstly the pressure terms are eliminated by cross-differentiating x-momentum and y-momentum equations. Then by using the definition of stream function and vorticity for steady and two-dimensional flows, the resulting combined equation is transformed into a form, known as the vorticity-transport equation. Similarly, the continuity equation can also be expressed in terms of the stream function and the vorticity. The resulting two equations can then be solved for the two dependent variables which are the stream function and vorticity. Upon convergence of the iterative process, pressure can be obtained separately by solving a Poisson equation. Although this approach has a wide usage, it is limited to two-dimensional flow problems only. Also the use of vorticity boundary conditions, which is required, is difficult to handle. Because of these difficulties, the other approach; primitive variables formulation is used. Primitive variables mean velocity and pressure as the dependent variable. The components of velocity and the pressure are discretised on the staggered grids by using finite volume method in the present study. Other techniques, based on the primitive variables formulations for solving the incompressible Navier-Stokes equations, are discussed in the next section.

1.5 Review of Literature

With vorticity / stream function approach, separated flows are studied and convergent solutions are obtained for any Reynolds number as discussed in detail by Burggraf [5]. Later various qualitative and quantitative comparisons have been made to determine effects of Reynolds number and grid size by Bozeman and Dalton [6].

Then Keller and Schreiber [7] achieved accurate solutions by using more efficient and reliable numerical techniques of higher-order accuracy. High-Reynolds number solutions with multigrid method is discussed and results for high Reynolds numbers and mesh refinements are presented by Ghia and Shin [8].

The primitive variable formulation is another approach for solving the incompressible Navier-Stokes equations. In the primitive variable formulations, three components of velocity and pressure are chosen as dependent variables and artificial compressibility is used. One of these methods based on the primitive variables is developed by Chorin [9]. When only the steady-state solution is sought, Chorin [9] introduced an effective way to overcome the difficulty inherent due to the constraint in the continuity equation by adding a time derivative of the pressure to the continuity equation [10]. This term is multiplied by an "artificial compressibility" coefficient. By this way, the velocity and pressure are coupled. At a given time level, the equation are advanced in pseudo-time by sub iterations until a converged velocity field is obtained at the next time level [3].

For the unsteady two-dimensional Navier-Stokes equations, Harlow and Welch [11] proposed a method employing the solution of the Poisson equation for the pressure so that the continuity equation is satisfied at each time step. Chorin [12] present a method that does not use the Poisson equation, by introducing an intermediate step in which the flow velocities are first obtained by solving momentum equations with pressure gradients being omitted. Then in order to obtain a divergence free velocity field, the velocities are corrected successively by the pressure gradients in the following time step until the continuity equation is satisfied [10].

Patankar [2] was developed a method based on SIMPLE algorithm (Semi-Implicit Method for Pressure Linked Equations) for laminar flow problems. In this algorithm the convection fluxes per unit mass F through cell faces are evaluated from guessed velocity components. Moreover, a guessed pressure field is used to solve the momentum equations. A pressure correction equation, deduced from the continuity equation, is solved to obtain a pressure correction field which is in turn used to update the velocity and pressure fields. To start the iterative process initial guesses for the velocity and pressure fields are used. As the algorithm proceeds, the aim must be progressively to improve these guessed fields. The process is iterated until convergence of the velocity and pressure fields [1]. Malalasekera and Versteeg [1] has been recently discussed the methodology of the SIMPLE algorithm and its variants for two-dimensional control volumes. SIMPLE algorithm is based on finite volume discretisation on staggered grid of governing equations.

1.6 Present Study

The present work aims at formulating and evaluating the SIMPLE algorithm and its variants for obtaining accurate numerical solutions to incompressible Navier-Stoke flows by means of finite volume method. This is done by solving two dimensional incompressible Navier-Stokes equations and continuity equation iteratively as explained in the previous section.

In this study, two-dimensional flow test problems are used to apply and evaluate the SIMPLE algorithm and its variants. These test cases are 'Lid-Driven Cavity' and 'Flow over a Backward-Facing Step'. In both cases, flows are considered as steady and laminar. Therefore, results of the lid-driven cavity are obtained up to a Reynolds number of 10000. On the contrary, the highest Reynolds number, used for the flow over a backward-facing step, is 800. While reaching the accurate result, qualitative comparisons are done with the published results in the literature.

Firstly differencing schemes, which are used to interpolate the property values in the discretised equations, are compared to determine which scheme is more accurate. Secondly, both uniform and clustered meshes with different sizes are used. Since grid size is a suitable compromise between desired accuracy and solution time cost. Grid independent solutions are obtained without the need to use an excessively fine grid. After achieving the better differencing scheme type and suitable grid size, both SIMPLE and SIMPLER (revised SIMPLE) are compared with Ghia's [8] solutions.

Since both 'Lid-Driven Cavity' and 'Flow over a Backward-Facing Step' test cases are examples of recirculating flows, vortices are occurred in the internal flow domains. Also; locations centers, sizes and strengths of the vortices are tabulated and compared with those presented in the literature.

The following chapters contribute the present study in detail. The governing equations for incompressible viscous flows are introduced in Chapter 2. Chapter 3 presents the discretisation process by means of the finite volume method and the solution procedure for discretised equations which is the SIMPLE algorithm and its variants. Computed results by SIMPLE and SIMPLER methods using two test problems are presented and evaluated in Chapter 4. A comparison with published results will be used to demonstrate the capability and accuracy of the present formulations and algorithms. Finally, Chapter 5 consists of discussions and conclusions, and recommendations for development of the algorithm are suggested for future research.

CHAPTER 2

GOVERNING EQUATIONS AND THEORETICAL FORMULATION

2.1 Governing Equations

Mathematical forms of the conservation laws of physics can be written in the conservative or divergence form for the 3-D unsteady flow of a compressible Newtonian fluid passing through infinitesimal control volume,

(a) Continuity Equation

$$\frac{\partial \rho}{\partial t} + div(\rho V) = 0 \tag{2.1}$$

(b) Momentum Equation

The *x*-component of the momentum equation is obtained by setting the rate of change of *x*-momentum of the fluid particle equal to the total force in the *x*-direction on the fluid element due to surface stress plus the rate of increase of *x*-momentum due to sources and is given by:

$$\frac{\partial (\rho u)}{\partial t} + div(\rho u V) = \frac{\partial (-p + \tau_{xx})}{\partial x} + \frac{\partial \tau_{yx}}{\partial y} + \frac{\partial \tau_{zx}}{\partial z} + S_{Mx} \tag{2.2.a}$$

The *y*-component of the momentum equation is given by;

$$\frac{\partial (\rho v)}{\partial t} + div(\rho v V) = \frac{\partial \tau_{xy}}{\partial x} + \frac{\partial (-p + \tau_{yy})}{\partial y} + \frac{\partial \tau_{zy}}{\partial z} + S_{My} \tag{2.2.b}$$

and the *z*-component of the momentum equation is;

$$\frac{\partial (\rho w)}{\partial t} + div(\rho w V) = \frac{\partial \tau_{xz}}{\partial x} + \frac{\partial \tau_{yz}}{\partial y} + \frac{\partial (-p + \tau_{zz})}{\partial z} + S_{Mz} \tag{2.2.c}$$

where ρ is the density, p is the pressure field, V is the velocity vector, μ is the dynamic coefficient of viscosity, S is the source per unit volume per unit time and u, v, w are the components of velocity vector in x, y and z, directions.

The normal stress is due to the pressure field and denoted by p. Moreover, the viscous stress, which is denoted by τ, and are proportional to the rates of angular deformation for Newtonian fluids. The viscous stress components in the momentum equations are:

$$\tau_{xx} = 2\mu\frac{\partial u}{\partial x} + \lambda divV \quad \tau_{yy} = 2\mu\frac{\partial v}{\partial y} + \lambda divV \quad \tau_{zz} = 2\mu\frac{\partial w}{\partial z} + \lambda divV \tag{2.3.a}$$

$$\tau_{xz} = \tau_{zx} = \mu(\frac{\partial u}{\partial y} + \frac{\partial v}{\partial x}) \quad \tau_{xy} = \tau_{yx} = \mu(\frac{\partial u}{\partial y} + \frac{\partial v}{\partial x}) \quad \tau_{yz} = \tau_{zy} = \mu(\frac{\partial u}{\partial y} + \frac{\partial v}{\partial x}) \tag{2.3.b}$$

where λ is the second coefficient of viscosity, μ is the dynamic coefficient of viscosity, and its effect is small in practice, for gases it can be taken as -2/3 μ.

(c) Internal Energy Equation:

$$\frac{\partial(\rho i)}{\partial t} + div(\rho iV) = -pdiv(V) + div(k\nabla T) + \Phi + S_i \tag{2.4}$$

where $i = i(\rho, T)$ is the specific internal energy, T is the temperature Φ is the dissipation factor and q is the heat flux vector.

Since the vector momentum equation states the rate of change of momentum of a fluid particle, it can be written as three scalar momentum equations for x, y and z, directions. Although there are five equations, namely continuity, three components of the momentum and energy equations, there are six unknowns in these five equations. These are three velocity components, density, pressure and temperature. One more equation is needed and this equation is equation of state which relates pressure to the density and temperature.

$$p = p(\rho, T) \tag{2.5}$$

With the addition of the equation state to the continuity, momentum and energy equations that are Equations (2.1), (2.2) and (2.4) which are also called as Navier-Stokes equations for a Newtonian fluid, modeling the fluid flow can be carried out for all types of flows.

For incompressible flows, it is assumed that there are no density variations and the density can be treated as constant. The rate of change of density in the continuity equation drops. Because of constant density, the energy equation is decoupled from the continuity and momentum equations and the equation of state is no longer needed. The fluid flow can now be modeled by using continuity and momentum equations. In this case, four partial differential equations can be solved for the four unknowns which are the three velocity components and pressure. Afterwards if the problem involves any heat transfer, energy equation is solved after correct flow field is obtained.

2.2 Conservation Equations in Cartesian Coordinates

The governing equations of steady incompressible flows in two-dimensional Cartesian coordinates are written as follows:

(i) Continuity Equation:

When the flow is steady, the time rate of change of the density, which is the first term in the left hand side of the equation (2.1), drops. The net flow of mass out of the flow element across its boundaries, which described by the second term in the left hand side, is so called convective term is expressed for two dimensional Cartesian coordinates. Then the continuity equation (2.1) becomes:

$$\frac{\partial}{\partial x}(\rho u)+\frac{\partial}{\partial y}(\rho v)=0 \tag{2.6}$$

(ii) Momentum Equations:

The first term on the left hand side of the equation (2.2) is the rate of change of velocity which drops when the flow is steady. When the body forces are also neglected, equation (2.2) becomes:

$$\nabla \bullet (\rho u V) = -\nabla p + \nabla \bullet \tau \tag{2.7}$$

After substituting Equation (2.3) into Equation (2.7), the momentum equation in the *x*-direction becomes:

$$\frac{\partial}{\partial x}(\rho uu)+\frac{\partial}{\partial y}(\rho vu)=-\frac{\partial P}{\partial x}+\frac{\partial}{\partial x}\left[2\mu\frac{\partial u}{\partial x}+\lambda\nabla\bullet V\right]+\frac{\partial}{\partial y}\left[\mu\left(\frac{\partial u}{\partial y}+\frac{\partial v}{\partial x}\right)\right] \quad (2.8)$$

The re-arranging the viscous terms in the above equation may be rearranged in the following way to yield:

$$\begin{aligned}\frac{\partial}{\partial x}\left[2\mu\frac{\partial u}{\partial x}+\lambda\nabla\bullet V\right]+\frac{\partial}{\partial y}\left[\mu\left(\frac{\partial u}{\partial y}+\frac{\partial v}{\partial x}\right)\right]&=\frac{\partial}{\partial x}\left(\mu\frac{\partial u}{\partial x}\right)+\frac{\partial}{\partial y}\left(\mu\frac{\partial u}{\partial y}\right)\\+\left[\frac{\partial}{\partial x}\left(\mu\frac{\partial u}{\partial x}\right)+\frac{\partial}{\partial y}\left(\mu\frac{\partial v}{\partial x}\right)\right]+\frac{\partial}{\partial x}(\lambda\nabla\bullet V)&=\nabla\bullet(\mu\nabla u)-S_u\end{aligned} \quad (2.9)$$

where S_u is defined as source term due to the smaller contribution of the viscous stress terms in the momentum equation.

Finally substituting Equation (2.9) into Equation (2.8), momentum equation in the *x*-directions is obtained as follows. Similarly the momentum equation in the *y*-direction can be obtained as.

(ii) Momentum Equation in the *x*-direction:

$$\frac{\partial}{\partial x}(\rho uu)+\frac{\partial}{\partial y}(\rho vu)=\frac{\partial}{\partial x}\left(\mu\frac{\partial u}{\partial x}\right)+\frac{\partial}{\partial y}\left(\mu\frac{\partial u}{\partial y}\right)-\frac{\partial p}{\partial x}+S_u \quad (2.10)$$

(iii) Momentum Equation in the *y*-direction:

$$\frac{\partial}{\partial x}(\rho uv)+\frac{\partial}{\partial y}(\rho vv)=\frac{\partial}{\partial x}\left(\mu\frac{\partial v}{\partial x}\right)+\frac{\partial}{\partial y}\left(\mu\frac{\partial v}{\partial y}\right)-\frac{\partial p}{\partial y}+S_v \quad (2.11)$$

2.3 Convection and Diffusion Problems

The general transport equation governs the physical behavior of a fluid flow and also satisfies the generalized conservation principle. If the dependent variable is denoted by ϕ, the general differential transport equation is given by:

$$\frac{\partial}{\partial t}(\rho\phi)+\nabla\bullet(\rho V\phi)=\nabla\bullet(\Gamma\nabla\phi)+S_\phi \quad (2.12)$$

where Γ is the diffusion coefficient and S_ϕ is the source term. The first and second term on the lfeft hand side of the general transport equation represent the unsteady and convection terms, respectively, while the first and second terms on the right hand side represent the diffusion and source terms, respectively. The dependent variable ϕ can represent the several different quantities, such as the velocity component, enthalpy [2]. It is obvious that flow properties are transported by means of convection and diffusion. For this reason, numerical modeling of fluid flow deals with the modeling of the two transport terms in the governing conservation equations. An important physical fact in the convection transport is that the flow property is convected in the strongest sense in the direction of the convecting velocity. In other words, the role of the convecting velocity is to sweep the influence of that property downstream in its direction. A larger convecting velocity means that the upstream information has a greater influence on the distribution of the flow property at a point along the direction of that convecting velocity. This physical fact should be appropriately taken into account in the modeling of the convection term. Meanwhile, the effect of diffusion is to disperse the influence of the flow variable in all directions [3].

According to above explanations, high convection and low diffusion indicate that the flow variable is distributed more in the stream wise direction with less variation of flow variable in the crosswise directions. On the other hand, with low convection and high diffusion, the transport of the flow variable is less characterized by dominant directions but it is more diffused [3].

Most important case occurs when the convection and the diffusion are both high. In this case, the distribution of the dependent variable is significant in the perpendicular directions normal to the streamlines of the flow, which is so called recirculating flows. Therefore to model such a flow accurately, the effects of the crosswise convection and diffusion terms should be taken into consideration in a domain discretised by a structured mesh.

When the general transport equation (2.13) is written for two-dimensional flow in Cartesian coordinates, it takes the following form:

$$\frac{\partial}{\partial t}(\rho\phi)+\frac{\partial}{\partial x}(\rho u\phi)+\frac{\partial}{\partial y}(\rho v\phi)=\frac{\partial}{\partial x}\left(\Gamma\frac{\partial\phi}{\partial x}\right)+\frac{\partial}{\partial y}\left(\Gamma\frac{\partial\phi}{\partial y}\right)+S_{\phi} \qquad (2.13)$$

CHAPTER 3

NUMERICAL ANALYSIS

3.1 Finite Volume Method

In the finite volume method, governing equations are integrated over each of the finite control volumes (smaller and non-overlapping subdomains) in the flow domain and obtained integrated transport equations are discretised by using finite difference type formulas. The resulting set of algebraic equations, are solved by using an iterative method. Thomas algorithm or the tri-diagonal matrix algorithm (TDMA), which is actually a direct method for the solution of one-dimensional problems, but it can be applied iteratively to solve multi-dimensional problems and is widely used in commercial CFD programs.

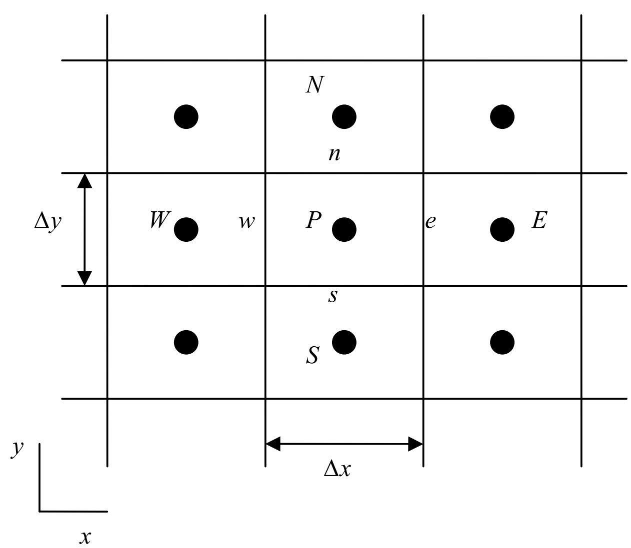

Figure 3.1 Two-dimensional control volumes in the x-y plane

Figure 3.1 shows a typical two-dimensional finite control volume over which the governing equations can be integrated.

3.2 Steady One-dimensional Convection and Diffusion

For steady one-dimensional convection and diffusion flow field without any sources, Equation (2.13) becomes:

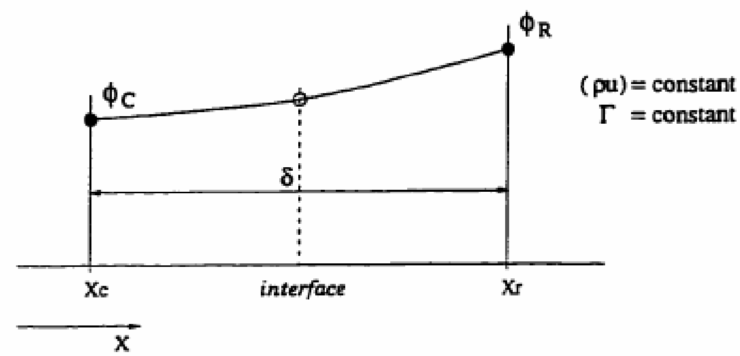

Figure 3.2 One-dimensional convection-diffusion profile [3]

$$\frac{\partial}{\partial x}(\rho u \phi) = \frac{\partial}{\partial x}\left(\Gamma \frac{\partial \phi}{\partial x}\right) \tag{3.1}$$

The flow should also satisfy the continuity equation:

$$\frac{\partial}{\partial x}(\rho u) = 0 \tag{3.2}$$

The one-dimensional control volume surrounding the general node P is shown in Figure 3.3. The nodes on the west and east sides of the node P are indicated by W and E, respectively. While the right and left faces of the control volume are indicated by w and e respectively.

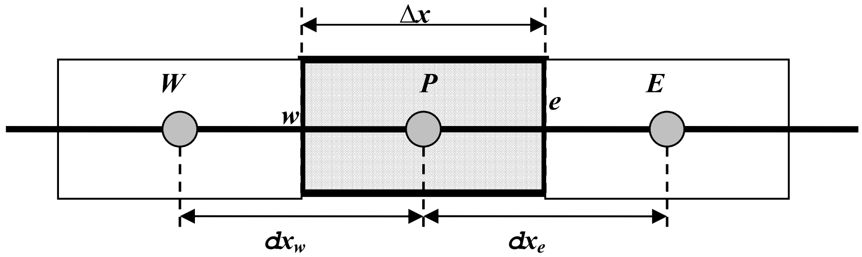

Figure 3.3 One-dimensional control volumes

The integration of transport equation (3.1) and continuity equation (3.2) over the control volume, shown on Figure 3.3, gives:

$$\int_{\Delta V} \frac{\partial}{\partial x}(\rho u \phi) = \int_{\Delta V} \frac{\partial}{\partial x}\left(\Gamma \frac{\partial \phi}{\partial x}\right) dV \tag{3.3}$$

$$\int_{\Delta V} \frac{\partial}{\partial x}(\rho u) = 0 \tag{3.4}$$

Then integration yields:

$$(\rho u A \phi)_e - (\rho u A \phi)_w = \left(\Gamma A \frac{\partial \phi}{\partial x}\right)_e - \left(\Gamma A \frac{\partial \phi}{\partial x}\right)_w \tag{3.5}$$

$$(\rho u A)_e - (\rho u A)_w = 0 \tag{3.6}$$

Here A is the cross-sectional area of the control volume face, ΔV is the control volume and Γ is the interface diffusion coefficient.

Introducing two new variables $F = \rho u$ and $D = \Gamma / \delta x$ to represent the convective mass flux per unit area and the diffusion conductance at the cell faces, respectively and assuming that $A_e = A_w = A$.

Peclet number, a non-dimensional measure of the relative strength of convection and diffusion, is defined as; $Pe = F/D$.

The cell face values of the variables F and D can be written as:

$$F_w = (\rho u)_w \quad \text{and} \quad F_e = (\rho u)_e \tag{3.7a}$$

$$D_w = \frac{\Gamma_w}{\delta x_w} \quad \text{and} \quad D_e = \frac{\Gamma_e}{\delta x_e} \tag{3.7b}$$

Then the integrated forms of convection-diffusion equation (3.5) and the continuity equation (3.6) can be written, respectively as:

$$F_e\phi_e - F_w\phi_w = D_e(\phi_E - \phi_P) - D_w(\phi_P - \phi_W) \tag{3.8}$$

$$F_e - F_w = 0 \tag{3.9}$$

To calculate the properties ϕ_e and ϕ_w at the faces, interpolation schemes are needed.

3.2.1 Central Differencing Scheme

Central differencing scheme is first natural approach. By using a piecewise linear profile of the dependent variable involving two neighboring points, the dependent variable and its derivative at cell faces in Figure 3.3 are approximated to compute the cell faces values for convective terms. This scheme is natural outcome of a Taylor-series formulation [2]. This scheme gives second-order accuracy. Then the cell face values of property ϕ are:

$$\phi_e = (\phi_P + \phi_E)/2 \qquad \text{and} \qquad \phi_w = (\phi_W + \phi_P)/2 \tag{3.10}$$

Substituting these values into Equation (3.8), assembling and introducing the coefficients of ϕ_W and ϕ_E as a_W and a_E, the discretised form of one-dimensional steady convection-diffusion becomes:

$$a_P\phi_P = a_W\phi_W + a_E\phi_E \tag{3.11}$$

where

$$a_W = D_w + \frac{F_w}{2}, a_E = D_e - \frac{F_e}{2} \text{ and } a_P = a_W + a_E + (F_e - F_w) \tag{3.12}$$

This formulation gives fairly accurate solutions for a class of low Reynolds number problems under specific conditions [3]. If east cell Peclet number Pe_e is greater than 2, the east coefficient will be negative [1]. This violates the Scarborough criterion (the positive coefficient rule) and cause physically impossible results or unstable numerical iterations.

For this reason, all early attempts to solve convection-dominated problems by the central-difference scheme were limited to low Reynolds number flows. Peclet number can be kept below two with small grid spacing. Because of these stability problems, this approach is not suitable for different flow calculations.

3.2.2 Upwind Differencing Scheme

Although central differencing scheme have second-order accuracy, for highly convective flows, that is for high Peclet number flows, unstable solutions are obtained. The basic reason for this behavior is that both upstream and downstream values have the same linear influence on the interface values in central differencing scheme whereas for high Peclet number flows, the upstream values have much stronger influence than the downstream values. For this reason, in upwind differencing scheme the value of ϕ at an interface is equal to the value of ϕ at the upstream grid point.

In Figures 3.4a and 3.4b, the nodes for the calculation of cell faces values are shown when the flow is positive and negative directions, respectively.

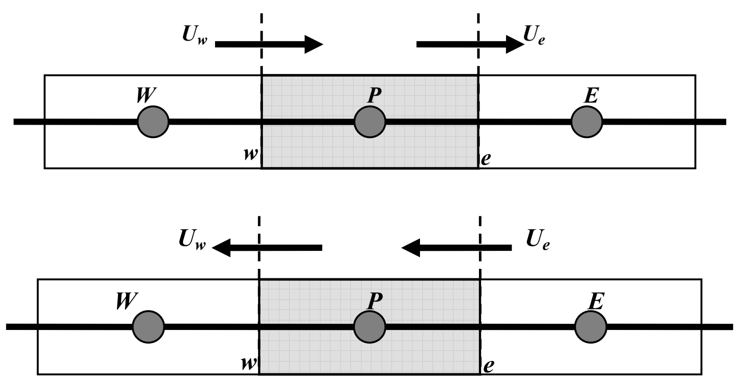

Figure 3.4 Control Volume when flow is in
(a) positive and (b) in negative direction [17]

When the flow is in the positive direction, the cell face values are given as:

$$\phi_e = \phi_P \qquad \phi_w = \phi_W \qquad \text{if} \qquad F_e, F_w > 0 \tag{3.13}$$

and when the flow is in the negative direction.

$$\phi_e = \phi_E \qquad \phi_w = \phi_P \qquad \text{if} \qquad F_e, F_w < 0 \tag{3.14}$$

If the equations (3.14) and (3.14) are introduced separately into Equation (3.8), then

$$a_P \phi_P = a_W \phi_W + a_E \phi_E \tag{3.15}$$

After assembling the obtained two equations and introducing the coefficients of ϕ_W and ϕ_E as a_W and a_E, for the discretised form of the equation becomes:

$$a_P = a_W + a_E + (F_e - F_w) \tag{3.16}$$

$$a_W = D_w + \max(F_w, 0) \text{ and } a_E = D_e + \max(0, -F_e) \tag{3.17}$$

Equation (3.17) takes care of both flow directions. The upwind scheme is only first-order accurate and is diffusive; therefore the introduced error is equivalent to the first-order Taylor-series truncation error.

From Equations (3.16) and (3.17), it is obvious that the coefficients are always positive. Therefore, all solutions are physically realistic, stable and no spurious wiggles occur in the solution.

A major drawback of this scheme is that it produces erroneous results when flow is not aligned with the grid lines and when Peclet number is less than or equal to 5. For flow calculations, first order upwind differencing scheme is not suitable and accurate. For this reason, a second-order upwind scheme and its variants are proposed which use more nodes in the flow direction to evaluate convective term more precisely. Researchers have concluded that for the evaluated test problems such as laminar lid-driven cavity, a second-order upwind scheme have been shown to give less numerical diffusion and, thus, a better accuracy than its first-order predecessor [3]. Also many researchers' give numerically accurate results with second-order upwind scheme for the two-dimensional lid-driven cavity for a wide range of Reynolds number.

3.2.3 Exponential Differencing Scheme

Exponential differencing scheme is based on the analytic solution of one-dimensional steady convection-diffusion equation (3.1). Γ and ρu are assumed as constant. If a domain $0 \le x \le L$ is used, boundary conditions at x=0 and L are:

At x=0 $\quad \phi = \phi_0 \quad$ (3.18a)

At x=L $\quad \phi = \phi_L \quad$ (3.18b)

The analytical solution is:

$$\frac{\phi - \phi_0}{\phi_L - \phi_0} = \frac{\exp(Pe.x/L) - 1}{\exp(Pe) - 1} \tag{3.19}$$

where $Pe = \rho u L / \Gamma$ is the Peclet number.

By replacing ϕ_0 and ϕ_L by ϕ_P and ϕ_E, respectively, the exact solution (3.19) can be used to represent ϕ between points P and E. Substituting the exact solution equation (3.19) into the equation (3.11) leads to the following equation:

$$\rho u \phi_e - \left(\Gamma \frac{\partial \phi}{\partial x} \right)_e = \rho u \left(\phi_P + \frac{\phi_P - \phi_E}{\exp(P_e) - 1} \right) \tag{3.20}$$

The standard form above equation is:

$$a_P \phi_P = a_W \phi_W + a_E \phi_E \tag{3.21}$$

where

$$a_P = a_W + a_E + (F_e - F_w) \tag{3.22a}$$

$$a_W = \frac{F_w \exp(F_w / D_w)}{\exp(F_w / D_w) - 1} \tag{3.22b}$$

$$a_E = \frac{F_e}{\exp(F_e / D_e) - 1} \tag{3.22c}$$

Due to analytic solution is applied; this scheme gives exact solutions for steady one-dimensional problems for any range of Peclet number and for any grid points. Although this scheme is quite accurate, it is not widely used. This scheme is not only computationally expensive but also is not exact for two- or three-dimensional situations. Instead of exponential scheme, the hybrid and power-law scheme are used in practice.

3.2.4 Hybrid Differencing Scheme

The hybrid differencing scheme is the combination of central and upwind differencing schemes. For small values of Peclet number $Pe < 2$, the central differencing scheme, which has second-order accuracy, is used. For large Peclet number $Pe > 2$, upwind scheme is employed for the convection term and the diffusion is set as zero. Since the hybrid scheme is dependent on the Peclet number, the local Peclet number is evaluated at the face of each control volume to calculate the net flux through each face.

The general form of discretised equation is:

$$a_P \phi_P = a_W \phi_W + a_E \phi_E \tag{3.23}$$

where

$$a_P = a_W + a_E + (F_e - F_w) \tag{3.24a}$$

$$a_W = \max\left[F_w, \left(D_w + \frac{F_w}{2}\right), 0\right] \tag{3.24b}$$

$$a_E = \max\left[-F_e, \left(D_e - \frac{F_e}{2}\right), 0\right] \tag{3.24c}$$

The scheme is fully conservative and since the coefficients are always positive it is conditionally bounded. The scheme produces physically realistic solutions and highly stable compared to higher order schemes [1].

The hybrid scheme can be applied to two- or three-dimensional problems, whereas the only disadvantage is that it possesses only first-order accuracy.

3.2.5 Power-Law Differencing Scheme

Patankar [2] proposed a power-law differencing scheme having a better accuracy compared to the hybrid scheme. Patankar [2] indicated that the power-law scheme is identical with hybrid scheme for $Pe > 10$. In this scheme, diffusion is set to zero when Peclet number is larger than 10. When the Peclet number is between 0 and 10, flux is calculated by using a polynomial.

The general form of equation is:

$$a_P \phi_P = a_W \phi_W + a_E \phi_E \tag{3.25}$$

where

$$a_P = a_W + a_E + (F_e - F_w) \tag{3.26a}$$

$$a_W = D_w \max\left[0, \left(1 - 0.1 |Pe_w|\right)^5\right] + \max[-F_w, 0] \tag{3.26b}$$

$$a_E = D_e \max\left[0, \left(1 - 0.1 |Pe_e|\right)^5\right] + \max[-F_e, 0] \tag{3.26c}$$

The power-law differencing scheme is more accurate for one-dimensional problems since it attempts to represent the exact solution more closely [1].

3.2.6 Higher-Order Differencing Schemes

In terms of Taylor series truncation error, the accuracy of hybrid and upwind schemes for cell Peclet numbers larger than 6, is first-order. Therefore these schemes do not give accurate results for flows in which the effects of transients, multi-dimensionality, or sources are important [13]. Higher order schemes can be used to get more accurate results because higher-order schemes include more neighbor points and this reduces the discretisation errors. Formulations that do not take into account the flow direction are unstable and, therefore, more accurate higher schemes, which preserve up-winding for stability and sensitivity to the flow direction, are needed [1].

Before considering the higher order schemes, the values of property ϕ_P for a range of Peclet number by various schemes are shown in Figure 3.5 with assumptions of $\phi_E = 1$, $\phi_W = 0$, the distances are equal δx_e and δx_w .

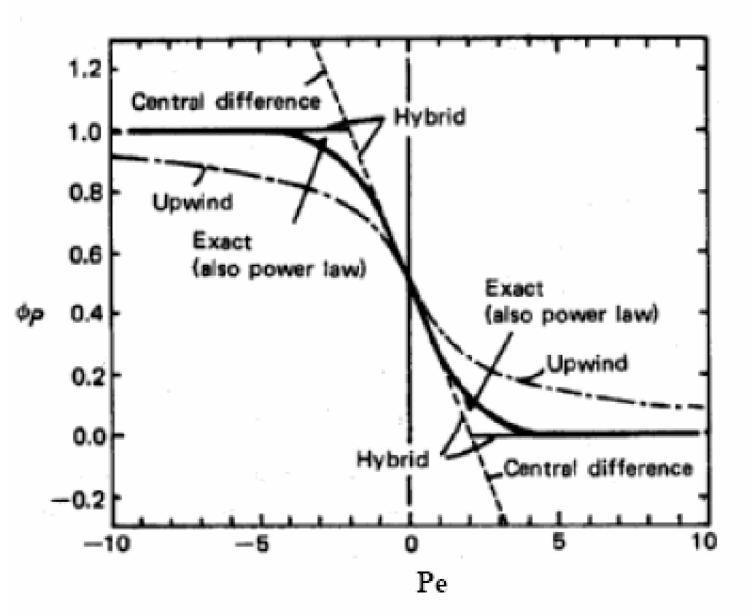

Figure 3.5 Prediction of ϕ_P for a range of Peclet number by various schemes [3]

All schemes expect central-difference scheme gives what may be termed a physically realistic solution.

3.2.7 Quadratic Upwind Differencing Scheme (QUICK)

Leonard [14] proposed a three-point upstream-weighted quadratic interpolation for cell face values, called the QUICK (Quadratic Upstream Interpolation for Convective Kinematics) scheme. This scheme is widely used and highly successful to solve the convection-diffusion problems.

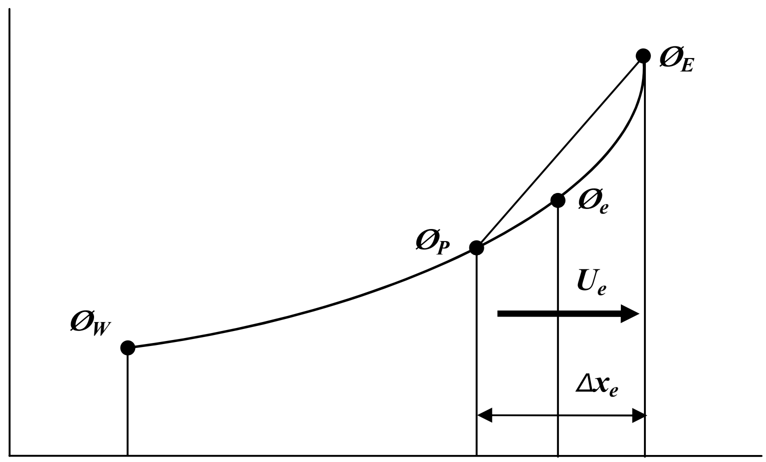

Figure 3.6 QUICK scheme parabolic profile for ϕ_e

The formulation of the QUICK scheme is shown in Figure 3.6 at an interface. The dependent variable at an interface is approximated by constructing the appropriate parabola using two adjacent neighboring nodes and one more node in the upstream direction [3].

When u_e is positive, the interface variable can be expressed as:

$$\phi_e = \frac{1}{2}(\phi_E + \phi_P) - \frac{1}{8}(\phi_W - 2\phi_P + \phi_E) \tag{3.27}$$

It is obvious that approximation is the linear interpolation between two neighboring points and corrected by a term proportional to the upstream curvature [3]. On uniform grid, this practice gives the same expression as central differencing scheme for diffusion [1]. However, Leonard [14] shows that its accuracy is greater than the central differencing scheme.

The QUICK scheme for one-dimensional convection-diffusion can be expressed in compact form as follows:

$$a_P\phi_P = a_W\phi_W + a_E\phi_E + a_{WW}\phi_{WW} + a_{EE}\phi_{EE} \tag{3.28}$$

where the central coefficient is

$$a_P = a_W + a_E + a_{WW} + a_{EE} + (F_e - F_w) \tag{3.29}$$

and the neighboring coefficients are

$$a_W = D_w + \frac{6}{8}\alpha_w F_w + \frac{1}{8}\alpha_e F_e + \frac{3}{8}(1-\alpha_w)F_w \tag{3.30a}$$

$$a_{WW} = -\frac{1}{8}\alpha_w F_w \tag{3.30b}$$

$$a_E = D_e - \frac{3}{8}\alpha_e F_e - \frac{6}{8}(1-\alpha_e)F_e - \frac{6}{8}(1-\alpha_W)F_w \tag{3.30c}$$

$$a_{EE} = \frac{1}{8}(1-\alpha_e)F_e \tag{3.30d}$$

with

$$\alpha_w = 1 \text{ For } F_w \rangle 0 \qquad \text{and} \qquad \alpha_e = 1 \text{ for } F_e \rangle 0 \tag{3.31a}$$

$$\alpha_w = 0 \text{ for } F_w \langle 0 \qquad \text{and} \qquad \alpha_e = 0 \text{ for } F_e \langle 0 \tag{3.31b}$$

Although higher order upwind-weighted methods are potentially quite stable, the QUICK scheme presented above can be unstable due to the appearance of negative main coefficients. Several researchers described an alternative approach in a way that negative coefficients are placed into the source term to prevent main coefficients from being negative. Hayase et al. [15] is one of the researchers who developed thiş approach by re-arranging the QUICK scheme and obtain more stable and the best convergence property. Systematic studies on the performance of the various QUICK schemes applied to the two-dimensional lid-driven cavity problem by Hayase et al. [15]. He clearly shows that the converged solutions of the various of QUICK schemes are identical to each other whereas number of iterations required to obtain converged solution differs. Although they are all derived from Leonard's [14] formulation, their respective stability characteristics show different behaviors. By the approach of Hayase et al [15], the coefficients are always kept positive so the requirements for boundedness, conservativeness and transportiveness are satisfied. [1]

Despite the QUICK scheme is more accurate than the other second-order schemes, undershoots and overshoots may occur near sharp transitions. Another difficulty is due to the application of the boundary conditions. For the cells near the boundaries, the scheme needs a value outside the flow domain, such as, cells adjacent to the wall. Because of the difficulties mentioned above, some modifications are done on the QUICK scheme and new schemes are introduced to eliminate the overshoots. Some of these modified schemes are ULTRA-QUICK, ULTRA-SHARP and QUICKEST.

3.3 Discretisation of General Transport Equation

The differential form of the general transport equation for two-dimensional flows is expressed by Equation (2.13). If the convection and diffusion terms in the same coordinate direction is combined as the total flux then,

$$J_x = \rho u \phi - \Gamma \frac{\partial \phi}{\partial x} \tag{3.32a}$$

$$J_y = \rho v \phi - \Gamma \frac{\partial \phi}{\partial y} \tag{3.32b}$$

where J_x and J_y are the total fluxes in the x and y directions.

Substituting Equations (3.32a) and (3.32b) into Equation (2.13), the corresponding conservation form of the general transport equation for two-dimensional flows can be written as:

$$\frac{\partial J_x}{\partial x} + \frac{\partial J_y}{\partial y} = S \tag{3.33}$$

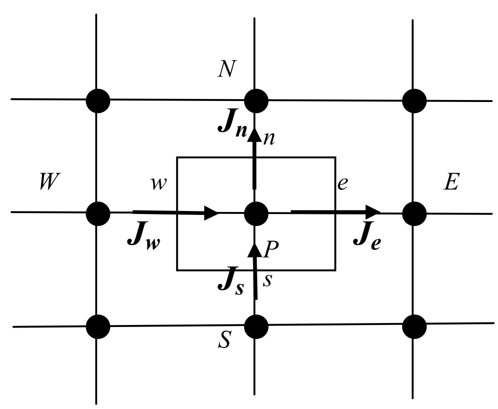

Figure 3.7 Two-dimensional control volumes

The integration of the general transport equation (3.33) over the control volume (Figure 3.7) for the grid point P results in the integral balance of general transport equation:

$$J_e - J_w + J_n - J_s = (S_u + S_P \phi_P)\Delta x \Delta y \qquad (3.34)$$

J_e, J_w J_n and J_s are integrated total fluxes both in the *x*-direction interface e and w and in the *y*-direction interface n and s over the control volume faces and given as:

$$J_e = \int_s^n J_{x.e}\, dy = J_e \Delta y \qquad J_w = \int_s^n J_{x,w}\, dy = J_w \Delta y \qquad (3.35)$$

$$J_n = \int_w^e J_{y.n}\, dx = J_n \Delta x \qquad J_s = \int_w^e J_{y.s}\, dx = J_s \Delta x \qquad (3.36)$$

3.3.1 Discretisation of Continuity Equation

The steady two –dimensional continuity equation in differential form can be written as:

$$\frac{\partial}{\partial x}(\rho u) + \frac{\partial}{\partial y}(\rho v) = 0 \qquad (3.37)$$

Substituting convective mass flux $F_x = \rho u$ and $F_y = \rho v$ into equation (3.37), it becomes:

$$\frac{\partial F_x}{\partial x} + \frac{\partial F_y}{\partial y} = 0 \qquad (3.38)$$

Similarly integrating equation (3.37) over the control volume in Figure 3.7, the integral balance of continuity equation is obtained:

$$F_e - F_w + F_n - F_s = 0 \qquad (3.39)$$

where F_e, F_w F_n and F_s are the mass flow rates through the faces of the control volume and assuming $A_e = A_w = \Delta y$ and $A_n = A_s = \Delta x$ then mass flow rates can be written as:

$$F_e = (\rho u)_e \Delta y \qquad F_w = (\rho u)_w \Delta y \tag{3.40a}$$

$$F_n = (\rho u)_n \Delta x \qquad F_s = (\rho u)_s \Delta x \tag{3.40b}$$

3.3.2 Discretisation of Momentum Equations in *x* and *y* Directions

To obtain discretised momentum equations, each velocity component *u* and *v* are replaced by the dependent variable ϕ in the general transport equation (2.13) respectively. After replacing ϕ with *v* for steady two-dimensional laminar flows, the conservation form of the *x*-momentum equation results as:

$$\frac{\partial}{\partial x}\left(\rho uu - \Gamma\frac{\partial u}{\partial x}\right) + \frac{\partial}{\partial y}\left(\rho vu - \Gamma\frac{\partial u}{\partial y}\right) = -\frac{\partial p}{\partial x} + S_u \tag{3.41}$$

where

$$J_{xx} = \rho uu - \Gamma\frac{\partial u}{\partial x} \tag{3.42a}$$

$$J_{yx} = \rho vu - \Gamma\frac{\partial u}{\partial y} \tag{3.42b}$$

If the total flux in *x*-momentum direction is shown with J_{xx} and two-directional total flux with J_{yx}, then Equation (3.41) becomes:

$$\frac{\partial J_{xx}}{\partial x} + \frac{\partial J_{yx}}{\partial y} = -\frac{\partial P}{\partial x} + S_u \tag{3.43}$$

Integration of Equation (3.33) over the two dimensional control volume in Figure 3.7 would give the integral balance of *x*-momentum equation:

$$J_e - J_w + J_n - J_s = (p_e - p_w) + (S_c + S_p u_p)\Delta x \Delta y \tag{3.44}$$

J_e, J_w J_n and J_s are integrated total fluxes over the control volume faces and can be written as:

$$J_e = \int_s^n J_{xx.e}\,dy = J_e \Delta y \qquad J_w = \int_s^n J_{xx,w}\,dy = J_w \Delta y \tag{3.45}$$

$$J_n = \int_w^e J_{yx.n}\,dx = J_n \Delta x \qquad J_s = \int_w^e J_{yx.s}\,dx = J_s \Delta x \tag{3.46}$$

$$p_e = \int_s^n p_{x.e} dy = p_e \Delta y \qquad\qquad p_w = \int_s^n p_{x,w} dy = p_w \Delta y \tag{3.47}$$

Since mass must be conserved, multiplying integral balance of the continuity equation (3.39) by u_P and subtracting from equation (3.44) yields:

$$\begin{aligned}&(J_e - F_e u_P) - (J_w - F_w u_P) + (J_n - F_n u_P) - (J_s - F_s u_P) = \\ &(p_e - p_w) + (S_c + S_p u_p)\Delta x \Delta y\end{aligned} \tag{3.48}$$

The assumption of uniformity over a control-volume face enables to employ one-dimensional practices for two-dimensional situation [2]. By this way the followings are obtained:

$$J_e - F_e u_P = a_E (u_P - u_E) \tag{3.49a}$$

$$J_w - F_w u_P = a_W (u_W - u_P) \tag{3.49b}$$

$$J_n - F_n u_P = a_N (u_P - u_N) \tag{3.49c}$$

$$J_s - F_s u_P = a_S (u_S - u_P) \tag{3.49d}$$

Then substituting Equations (3.49.a-d) into Equation (3.48) and rearranging the terms results in the final two-dimensional discretisation equation:

$$a_p u_P = a_E u_E + a_W u_W + a_N u_N + a_S u_S + b_u = \sum a_{nb} u_{nb} + b_u \tag{3.50}$$

The coefficients a_E, a_W, a_N and a_S represent the convection - diffusion influence at the four neighbor cell faces in terms of the mass flux F and diffusion conductance D and can be written as:

$$a_E = D_e A(|Pe_e|) + \max(-F_e, 0) \tag{3.51a}$$

$$a_W = D_w A(|Pe_w|) + \max(F_w, 0) \tag{3.51b}$$

$$a_N = D_n A(|Pe_n|) + \max(-F_n, 0) \tag{3.51c}$$

$$a_S = D_s A(|Pe_s|) + \max(F_s, 0) \tag{3.51d}$$

$$b_u = (p_e - p_w) + S_c \Delta x \Delta y \tag{3.51e}$$

$$a_p = a_E + a_W + a_N + a_S - S_p \Delta x \Delta y \tag{3.51f}$$

The mass fluxes are expressed Equations (3.40a) and (3.40b) also conductances in the above equations are defined by:

$$D_e = \frac{\Gamma_e \Delta y}{(\delta x)_e} \qquad D_w = \frac{\Gamma_w \Delta y}{(\delta x)_w} \tag{3.52a}$$

$$D_n = \frac{\Gamma_n \Delta x}{(\delta x)_n} \qquad D_s = \frac{\Gamma_s \Delta x}{(\delta x)_s} \tag{3.52b}$$

and the Peclet numbers are:

$$Pe_e = \frac{F_e}{D_e} \qquad Pe_w = \frac{F_w}{D_w} \qquad Pe_n = \frac{F_n}{D_n} \qquad Pe_s = \frac{F_s}{D_s} \tag{3.53}$$

The final unknown is the function $A(|Pe|)$ which can be chosen according to the desired scheme. If power-law scheme is chosen, then the function $A(|Pe|)$ becomes:

$$A(|Pe|) = \max\left(0, (1 - 0.1|Pe|)^5\right) \tag{3.54}$$

Patankar [2] stated that there are 'four basic rules' which the final discretisation equation should satisfy to get physically realistic solution and convergence. The final discretisation equation (3.50) obeys these 'four basic rules' by producing a diagonally dominant system of equations. The convection factors in the discretised continuity equation are assumed same as those in the discretised x-momentum equation to satisfy two of the 'four basic rules'. In this section 3.3.2, the x-momentum equation is discretised in the same manner the y-momentum equation can be also discretised.

3.4 Staggered Grid Arrangement

The discretised form of the *x*-direction momentum consists of the pressure gradient $-\frac{\partial p}{\partial x}$ which is integrated over the control volume and expressed as $(p_e - p_w)$. This is the pressure field which is net pressure force exerted on the control volume. Two-dimensional uniform grid arrangement is used and highly irregular 'checker-board' pressure field is assumed and illustrated in Figure 3.8.

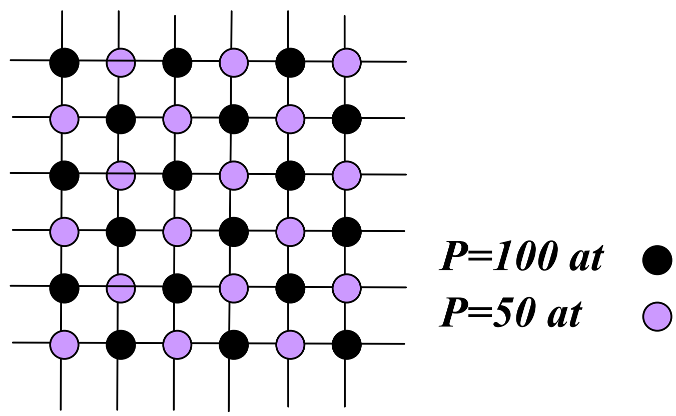

Figure 3.8 Checker-board Pressure Field

By using a piecewise linear profile for interface pressure gradient within the two grid points can be calculated. However, although the pressure field exhibits spatial oscillations, it is evaluated that all the discretised gradients are zero for all the nodal points. Therefore, highly non-uniform pressure field is considered as uniform pressure field and momentum equations remain unaffected by using zero pressure force. The similar difficulty, which is discussed by Patankar [2] is occurred in the discretisation of the continuity equation such as wavy velocity fields can satisfy the continuity equation whereas these velocity fields are not at all realistic.

The difficulty mentioned above can be overcome by using staggered grid arrangement, which is first used by Harlow and Welch [11], employing different grids for each dependent variable. In the staggered grid, the velocity components are evaluated at the faces of the control volume on the other hand scalar variables such as pressure, density, temperature etc., defined at the ordinary nodal points. In Figure 3.9, the staggered grid arrangement for two-dimensional flows is illustrated. The scalar variables, such as pressure, are stored at the nodes shown with (•). The *u*-velocities are defined by horizontal arrows; similarly *v*-velocities are calculated at vertical arrows.

With staggered grid arrangement, if the pressure gradient is calculated for the 'checker-board' pressure field, nodal pressure values produce non-zero pressure field. Therefore, by the staggered grid arrangement, the unrealistic results and oscillations are avoided. The other advantage of this staggered grid is that reasonable velocity fields occur to satisfy the continuity equation and, thus, prevent wavy velocity fields to satisfy the continuity equation. A further advantage is that it generates velocities exactly at the locations where they are required for the computation of the scalar transport convection-diffusion equations. Therefore, no interpolation is needed to calculate velocities at the scalar cell faces. [1]

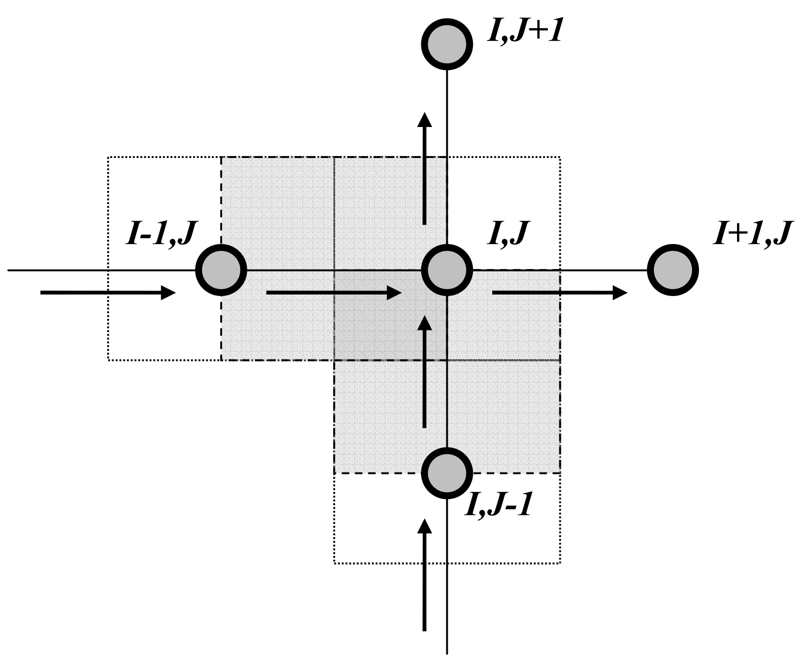

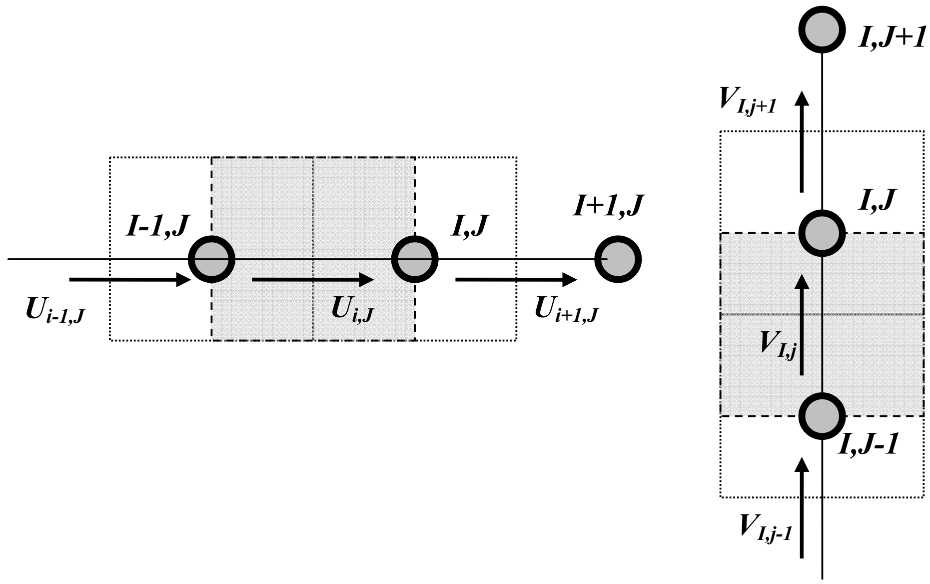

Figure 3.9 Staggered Grid Arrangements

By the staggered grid, all discretisation equations have its own control volume; therefore each equation is discretised on its own staggered control volume arrangement which is also shown in Figure 3.9.

The discretised momentum equations become:

$$a_{i,J}u_{i,J} = \sum a_{nb}u_{nb} + (p_{I-1,J} - p_{I,J})A_{i,J} + b_{i,J} \tag{3.55}$$

$$a_{I,j}v_{I,j} = \sum a_{nb}v_{nb} + (p_{I,J-1} - p_{I,J})A_{I,j} + b_{I,j} \tag{3.56}$$

To define grid nodes and cell faces, a subscript system is needed. Scalar nodes are shown with two capital letters such as point (I,J) in Figure 3.9. The *u*-velocities are identified at east and west cell faces of a scalar control volume so they are defined by a grid line and a cell boundary and indicated successively by a lowercase letter and a capital letter, such as (i,J). However v-velocities are indicated successively by a capital letter and a lowercase letter, such as (I,j).

The coefficients a_{nb}, $a_{i,J}$ and $a_{I,j}$ can be calculated with any differencing scheme. Also the convective flux per unit mass F and the diffusive conductance D at control volume cell faces are calculated according to new notation. The equations according to staggered grid arrangement have been discussed in detail by Malalasekera and Versteeg [1].

3.5 SIMPLE Algorithm

As mentioned before, SIMPLE is one of the approaches for solving incompressible flows iteratively. The method, which is explained by using the two-dimensional laminar flow equations in Cartesian coordinates, is described in Patankar and Spalding [2]. The procedure is to guess and to correct the pressure field in the flow domain. In the following sections, the SIMPLE method and its variants are briefly explained.

3.5.1 Momentum Equations

The procedure of the SIMPLE method starts by guessing the pressure field which is represented by $p*$. The momentum equations (3.55) and (3.56) are solved for the guessed pressure field. Then the momentum equations become:

$$a_{i,J}u^*_{i,J} = \sum a_{nb}u^*_{nb} + (p^*_{I-1,J} - p^*_{I,J})A_{i,J} + b_{i,J} \tag{3.57}$$

$$a_{I,j}v^*_{I,j} = \sum a_{nb}v^*_{nb} + (p^*_{I,J-1} - p^*_{I,J})A_{I,j} + b_{I,j} \tag{3.58}$$

The above discretised momentum equations are used to obtain the velocity field with $u*$ and $v*$ being the velocity components. Until the correct pressure field is applied, the calculated velocity components do not satisfy the continuity equation.

3.5.2 Correction Equations

In order to satisfy the continuity equation, converged velocity fields are needed, therefore the guessed pressure field should be improved. The correct pressure field is evaluated by the following equation where the guessed pressure field is corrected by the pressure correction p'.

$$p = p^* + p' \tag{3.59a}$$

Similarly, the corrected velocities u and v are obtained by adding velocity corrections u' and v' to imperfect velocity fields u^* and v^*, respectively.

$$u = u^* + u' \tag{3.59b}$$

$$v = v^* + v' \tag{3.59c}$$

The corrected velocity fields u and v are obtained when the correct pressure field p is applied to momentum equations. The discretised equations (3.55) and (3.56) are used to obtain the correct velocity field from the correct pressure field.

Subtracting Equations (3.57) and (3.58) from Equations (3.55) and (3.56), respectively and using the correction equations (3.59a), (3.59b) and (3.59c) results in:

$$a_{i,J} u'_{i,J} = \sum a_{nb} u'_{nb} + (p'_{I-1,J} - p'_{I,J}) A_{i,J} \tag{3.60}$$

$$a_{I,j} v'_{I,j} = \sum a_{nb} v'_{nb} + (p'_{I,J-1} - p'_{I,J}) A_{I,j} \tag{3.61}$$

Then dropping the terms $\sum a_{nb} u'_{nb}$ and $\sum a_{nb} v'_{nb}$, the velocity correction equations become:

$$u'_{i,J} = d_{i,J} (p'_{I-1,J} - p'_{I,J}) \tag{3.62}$$

$$v'_{I,j} = d_{I,j} (p'_{I,J-1} - p'_{I,J}) \tag{3.63}$$

where $d_{i,J} = A_{i,J} / a_{i,J}$ and $d_{I,j} = A_{I,j} / a_{I,j}$

Then substituting the above equations into the velocity correction equations (3.59b) and (3.59c) give the final form of velocity-correction formulas:

$$u_{i,J} = u^*_{i,J} + d_{i,J}(p'_{I-1,J} - p'_{I,J}) \tag{3.64a}$$

$$v_{I,j} = v^*_{I,j} + d_{I,j}(p'_{I,J-1} - p'_{I,J}) \tag{3.64b}$$

$$u_{i+1,J} = u^*_{i+1,J} + d_{i+1,J}(p'_{I,J} - p'_{I+1,J}) \tag{3.64c}$$

$$v_{I,j+1} = v^*_{I,j+1} + d_{I,j+1}(p'_{I,J} - p'_{I,J+1}) \tag{3.64d}$$

At this point, the equations, which are used to obtain the correct velocity components, are derived from momentum equations but as mentioned before velocity field should satisfy the continuity equation.

3.5.3 Pressure Correction Equation

Substituting the corrected velocities given by Equations (3.64a), (3.64b), (3.64c) and (3.64d) into the discretised form of the continuity equation (3.39) and doing some re-arrangements yields the pressure correction equation which is derived from the continuity equation as:

$$a_{I,J}p'_{I,J} = a_{I+1,J}p'_{I+1,J} + a_{I,J-1}p'_{I,J-1} + a_{I,J+1}p'_{I,J+1} + a_{I,J-1}p'_{I,J-1} + b'_{I,J} \tag{3.65}$$

where

$$a_{I,J} = a_{I+1,J} + a_{I-1,J} + a_{I,J+1} + a_{I,J-1} \tag{3.66}$$

and the coefficients are given by:

$$a_{I+1,J} = (\rho dA)_{i+1,J} \tag{3.67a}$$

$$a_{I-1,J} = (\rho dA)_{i,J} \tag{3.67b}$$

$$a_{I,J+1} = (\rho dA)_{I,j+1} \tag{3.67c}$$

$$a_{I,J-1} = (\rho dA)_{I,j} \tag{3.67d}$$

$$b'_{I,J} = \left(\rho u^* A\right)_{i,J} - \left(\rho u^* A\right)_{i+1,J} + \left(\rho v^* A\right)_{I,j} - \left(\rho v^* A\right)_{I,j+1} \tag{3.67e}$$

The mass source term $b'_{I,J}$ in the pressure correction equation (3.65) comes out from the starred velocity field, therefore if the mass source term is zero, it means that the continuity equation is satisfied and no need to correct the pressure. In addition to this, a mass source term represents how well the mass conservation is satisfied at each iteration so this quantity is often used as the indicator for convergence of the numerical solution [3].

The terms $\sum a_{nb}u'_{nb}$ and $\sum a_{nb}v'_{nb}$ are omitted while obtaining the velocity correction equations. This omission does not affect the final solution because of the pressure correction and velocity corrections will all be zero in a converged solution [1]. The omitted terms include the influence of the pressure correction on velocity; pressure corrections at nearby locations can change the neighboring velocities and thus cause a velocity correction at the point under consideration [2]. Because of omitting this influence, this method is considered as semi-implicit.

The pressure correction equation can likely diverge if under-relaxation is not used. The under-relaxation can be applied not only to the pressure correction equation (3.59a) but also velocity components can be improved by under-relaxation. But the main important thing is to apply optimum relaxation factor to accelerate the convergence and essential relaxation factor is flow dependent.

3.5.4 Solution Procedure

The discretised equations governing the flow field are non-linear. In the SIMPLE method, these non-linear equations are coupled by an iterative scheme. The non-linearity comes out from the coefficients and the source terms in the discretised equations because these are functions of the dependent variables whereas this can be handled by solving these terms independently and sequentially. This means that these terms are calculated from previous iteration values of the variables. By this way, these non-linear discretised equations are converted into the linear algebraic equations.

In addition to this, considering all control volumes in the flow domain leads to a tri-diagonal system of simultaneous algebraic equations. This system of equations for one dependent variable at a given time step are solved by iterative or indirect methods. For the two dimensional flows, Successive Line Over-Relaxation (SLOR) method is used to solve linear algebraic system of equations. SLOR method sweeps the two-dimensional flow computational domain line by line, in both directions. Then, Thomas algorithm or the Tri-Diagonal Matrix Algorithm (TDMA), which is widely used, is applied iteratively to each line sweep [3]. This line-by-line calculation procedure is repeated several times until a converged solution is obtained.

3.5.5 SIMPLE Algorithm Summary

The sequence of operation of the SIMPLE algorithm for steady two-dimensional laminar flows is shown in Figure 3.10 and is summarized as follows:

1. Guess the initial flow field (starred pressure and velocity components).
2. Solve the momentum equations (3.57) and (3.58) in order to obtain starred velocities.
3. Solve the pressure correction equation (3.65).
4. Correct the pressure by Equation (3.59a).
5. Calculate the velocities from their starred values by using correction equations (3.59b) and (3.59c).
6. Solve the other discretisation equation for other variables ϕ's. If the variable does not affect flow field, it is better to calculate it after obtaining the converged solution.
7. Using the pressure field obtained in the previous step as an initial guess, repeat steps 2-6 until a converged solution is obtained.

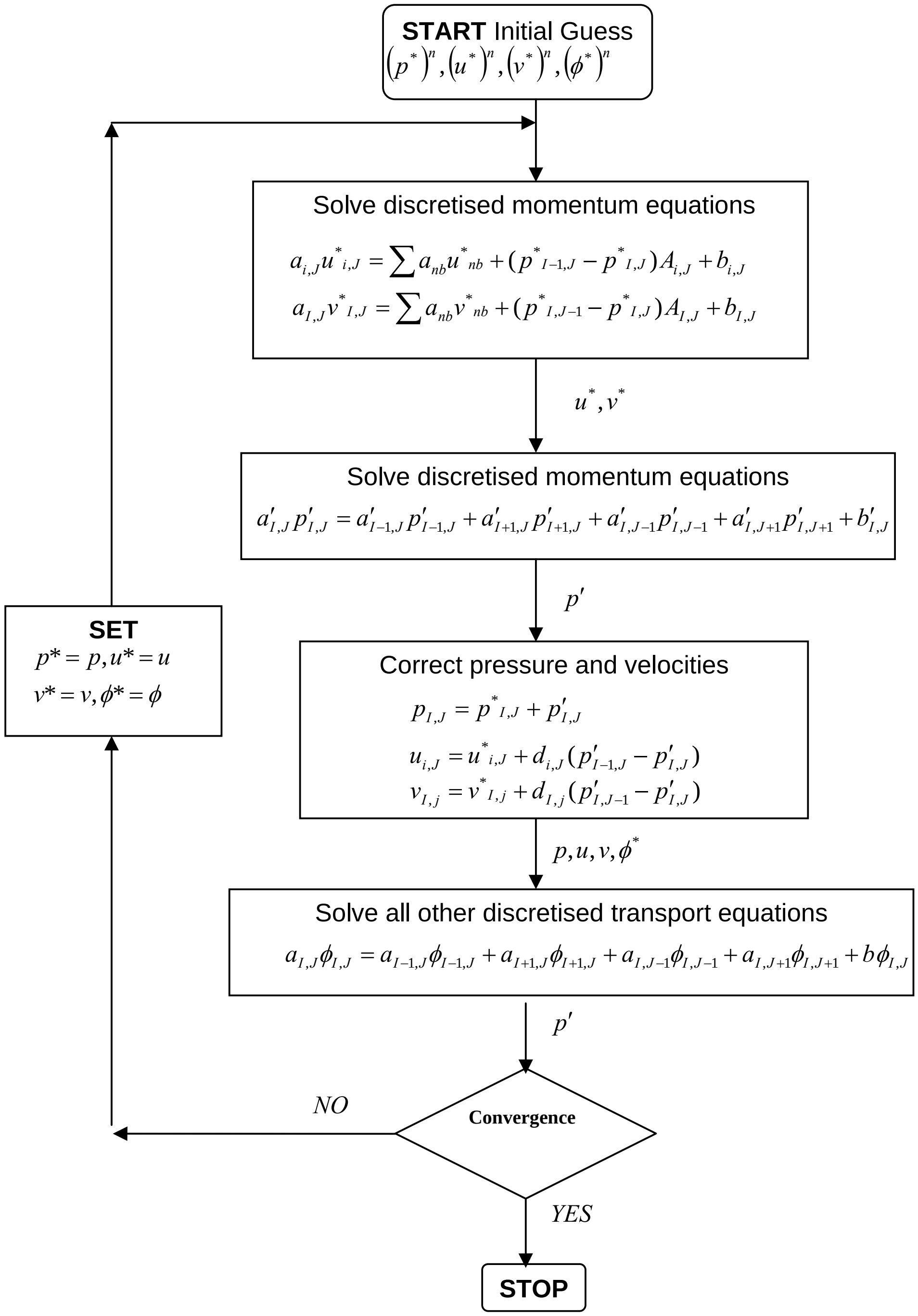

Figure 3.10 The SIMPLE Algorithm

3.6 Variants of SIMPLE Algorithm

The need for improving the convergence rate, increasing computational efficiency and accelerating the coupling process between velocity and pressure arises a number of modifications on the coupling process of the SIMPLE algorithm which is described by Patankar and Spalding [2]. Also several different algorithms have been proposed and developed by various researchers. The variants of SIMPLE algorithm, discussed in this section, are SIMPLER, SIMPLEC and SIMPLEV algorithms.

3.6.1 The SIMPLER Algorithm

To improve the convergence rate of the SIMPLE algorithm, revised SIMPLE is introduced by Patankar and Spalding [2]. Since omitting terms $\sum a_{nb}u'_{nb}$ and $\sum a_{nb}v'_{nb}$ removes neighbor velocity corrections from the velocity-correction equation, only pressure correction contributes the velocity correction equation. In this case, it is reasonable to suppose that the pressure-correction equation does a fairly good job of correcting the velocities, but a rather poor job of correcting the pressure.

In the SIMPLER algorithm, the discretised continuity equation (3.39) is used to derive a discretised equation for pressure, instead of a pressure correction equation as in the SIMPLE method [1].

In the SIMPLER method, the discretised momentum equations are obtained by rearranging Equations (3.55) and (3.56) as follows:

$$u_{i,J} = \frac{\sum a_{nb}u_{nb} + b_{i,J}}{a_{i,J}} + \frac{A_{i,J}}{a_{i,J}}\left(p_{I-1,J} - p_{I,J}\right) \tag{3.68}$$

$$v_{I,j} = \frac{\sum a_{nb}v_{nb} + b_{I,j}}{a_{I,j}} + \frac{A_{I,j}}{a_{I,j}}\left(p_{I,J-1} - p_{I,J}\right) \tag{3.69}$$

First terms in right hand side of above equation are defined as pseudo-velocities $\hat{u}$ and $\hat{v}$:

$$\hat{u}_{i,J} = \frac{\sum a_{nb} u_{nb} + b_{i,J}}{a_{i,J}} \tag{3.70}$$

$$\hat{v}_{I,j} = \frac{\sum a_{nb} v_{nb} + b_{I,j}}{a_{I,j}} \tag{3.71}$$

Substituting these into Equations (3.57) and (3.58) yields:

$$u_{i,J} = \hat{u}_{i,J} + d_{i,J}\left(p_{I-1,J} - p_{I,J}\right) \tag{3.72a}$$

$$v_{I,j} = \hat{v}_{I,j} + d_{I,j}\left(p_{I,J-1} - p_{I,J}\right) \tag{3.72b}$$

where $d_{i,J} = {A_{i,J}}/{a_{i,J}}$ and $d_{I,j} = {A_{I,j}}/{a_{I,j}}$

Then substituting the corrected velocities $u_{i,J}$ and $v_{I,j}$ in Equations (3.72a), (3.72b) and similarly $u_{i+1,J}$ and $v_{I,j+1}$ into the discretised form of the continuity equation (3.39) and doing some rearrangements results in the pressure equation which is derived from the continuity equation as.

$$a_{I,J} p_{I,J} = a_{I+1,J} p_{I+1,J} + a_{I,J-1} p_{I,J-1} + a_{I,J+} p_{I,J+1} + a_{I,J-1} p_{I,J-1} + b_{I,J} \tag{3.73}$$

where

$$a_{I,J} = a_{I+1,J} + a_{I-1,J} + a_{I,J+1} + a_{I,J-1} \tag{3.74}$$

and the coefficients are given by:

$$a_{I+1,J} = (\rho dA)_{i+1,J} \tag{3.75a}$$

$$a_{I-1,J} = (\rho dA)_{i,J} \tag{3.75b}$$

$$a_{I,J+1} = (\rho dA)_{I,j+1} \tag{3.75c}$$

$$a_{I,J-1} = (\rho dA)_{I,j} \tag{3.75d}$$

$$b_{I,J} = \left(\rho\hat{u}A\right)_{i,J} - \left(\rho\hat{u}A\right)_{i+1,J} + \left(\rho\hat{v}A\right)_{I,j} - \left(\rho\hat{v}A\right)_{I,j+1} \tag{3.75e}$$

Equation (3.73) is same as Equation (3.65) in the SIMPLE method whereas the difference is the mass source term is calculated by using pseudo-velocities in the

SIMPLER method. Although the pressure equation and pressure correction equation are identical, there is one major difference: No approximations have been introduced in the derivation of pressure equation. [2]. Thus correct velocity fields leads to correct pseudo-velocities which results in correct pressure field at once [2].

The sequence of operations of the SIMPLER method can be summarized as follows:

1. Guess the initial velocity field.
2. Calculate pseudo-velocities by using Equations (3.70) and (3.71) from the values of neighbor velocities.
3. Solve pressure equation (3.73) to obtain the pressure field.
4. Using this pressure field as the starred pressure fields solve the momentum equations (3.57) and (3.58).
5. Solve the pressure correction equation (3.65).
6. Calculate the velocities from their starred values by using correction equations (3.59b) and (3.59c)and $v_{I,j+1}$ c) but do not correct the pressure.
7. Solve the other discretisation equations for other ϕ variables. If the variable does not affect flow field, it is better to calculate it after obtaining the converged solution.
8. Using the pressure field obtained in the previous step as an initial guess, repeat steps 2-7 until a converged solution is obtained.

3.6.2 The SIMPLEC Algorithm

The SIMPLEC is the SIMPLE-Consistent algorithm of Van Doormal and Raithby (1984), as explained by Malalasekera and Versteeg [1]. Its only difference from the SIMPLE algorithm is the velocity correction equation. The SIMPLE algorithm omits the neighbor velocity correction terms whereas

SIMPLEC algorithm omits less significant ones than those omitted in the SIMPLE algorithm.

In the SIMPLE algorithm the *x*-momentum equation (3.60) can be written as:

$$\left(1-\frac{\sum a_{nb}}{a_{i,J}}\right)u'_{i,J}=\frac{1}{a_{i,J}}\sum a_{nb}(u'_{nb}-u'_{i,J})+(p'_{I-1,J}-p'_{I,J})\frac{A_{i,J}}{a_{i,J}} \tag{3.76}$$

The SIMPLE algorithm neglects the terms $\sum a_{nb}u'_{nb}$ whereas the SIMPLEC algorithm omits the terms $\frac{1}{a_{i,J}}\sum a_{nb}\left(u'_{nb}-u'_{i,J}\right)$. The SIMPLEC algorithm assumes $\left|u'_{nb}-u'_{i,J}\right|\langle\langle\left|u'_{nb}\right|$ therefore, the SIMPLEC algorithm becomes more accurate than the SIMPLE algorithm by neglecting the terms $\frac{1}{a_{i,J}}\sum a_{nb}\left(u'_{nb}-u'_{i,J}\right)$.

Then *u*- and *v*-velocity correction equations of SIMPLEC algorithm are given by:

$$u'_{i,J}=d_{i,J}(p'_{I-1,J}-p'_{I,J}) \tag{3.77}$$

$$v'_{I,j}=d_{I,j}(p'_{I-1,J}-p'_{I,J}) \tag{3.78}$$

where

$$d_{i,J}=\frac{A_{i,J}}{a_{i,J}-\sum a_{nb}} \text{ and } d_{I,j}=\frac{A_{I,j}}{a_{I,j}-\sum a_{nb}} \tag{3.79}$$

The operation sequence of the SIMPLEC algorithm is identical to SIMPLE algorithm except that the *d*-terms are evaluated by using Equation (3.79).

3.6.3 The SIMPLEV Algorithm

The SIMPLEV (SIMPLE-Vincent) algorithm is an improved version of the SIMPLE algorithm where the under-relaxation and temporal terms are removed from pressure correction equation of the SIMPLE algorithm [16]. Anjorin and Barton [16] studied the SIMPLEV method and compared it with SIMPLE method. Not only the number of iterations performed to obtain converged solutions is compared, but also how quickly the converged solution is obtained for different under-relaxation factors and for different grid sizes are discussed. Results have shown that the higher efficiency of the SIMPLEV algorithm strongly depends on the under-relaxation factor. Solution of pressure correction equation is the fastest in the SIMPLEV for all cases except for grid systems with a large number of nodes, reducing the efficiency of SIMPLEV. All calculations in the SIMPLEV algorithm converged more rapidly [16].

3.7 Implementation of Boundary Condition for Pressure

The pressure field obtained by solving the pressure correction equation does not give absolute pressures [2]. If all the normal velocities are given or known at the boundaries, knowing the pressure at these boundaries does not affect the interior pressures. Because of the SIMPLE algorithm, which is an iterative procedure for incompressible flows where equation of state can not be used, converged solution does not result in unique absolute pressure field. The absolute pressure field of the converged solution is only dependent on the initial guessed pressure in the flow domain. A channel flow problem in Figure 3.11 is a simple example.

At the inlet, velocity profile is given. Then it is assumed that inlet velocity profile is fully developed for the chosen Reynolds number and channel length is sufficient for the outlet velocity to be fully developed. Because of the conservation of mass, inlet mass flow rate is equal to the exit mass flow and the flow at the outlet boundary is calculated without requiring the pressure field at the outlet when the converged solution is obtained.

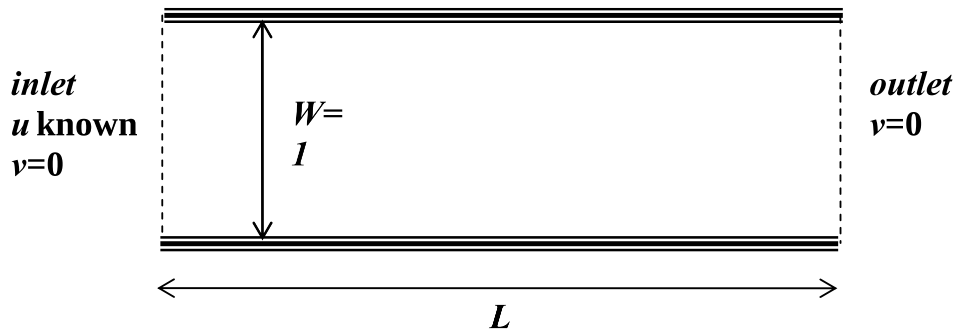

Figure 3.11 Two-dimensional channel flow with given inlet velocity profile

By this way, without inlet and outlet pressure fields, the velocity field at the outlet is calculated. Boundary pressure can be computed by extrapolation using the interior pressure values [3]. For this reason, a pressure value at a certain boundary can not be specified and leads initial guess to determine the 'level' of the resulting pressure field during the iterative procedure [3].

CHAPTER 4

NUMERICAL RESULTS AND TESTING OF THE ALGORITHMS

4.1 Benchmark Solutions

In the previous chapter, not only the SIMPLE method and its variants for solving Navier-Stokes equations but also different discretisation schemes, are explained and derived to govern incompressible fluid flows.

In this chapter, the numerical methods described in the previous chapter are tested and benchmarked by applying them to solve two classic benchmark test problems. These are 'Lid-Driven Cavity' and 'Flow over a Backward-Facing Step'. Both are internal flows and are tested for the case of two dimensional steady laminar incompressible flows. The SIMPLE method and its variants are validated and compared for different numerical techniques at different Reynolds numbers by using appropriate grid size and reasonable discretisation schemes. 'Lid-Driven Cavity' problem, which is tested and compared by various researchers, is the model of recirculating flow in a square cavity which is driven by the motion of the upper lid.

The second case is the flow over a backward-facing step which is a long channel flow where a fully developed inflow expands suddenly due to the changes in the geometry. Therefore, laminar separation and recirculation occur in the flow domain.

4.2 Two-Dimensional Lid Driven Cavity

The first test case for evaluating the numerical methods is the two-dimensional lid-driven cavity, which is one of the simplest and excellent test cases because of its geometry and boundary conditions and the existence of the several relatively large recirculating regions.

4.2.1 Definition of Problem Characteristics

The two-dimensional lid-driven cavity is shown in Figure 4.1. The fluid motion in the square cavity is driven by the uniform translation of the upper lid.

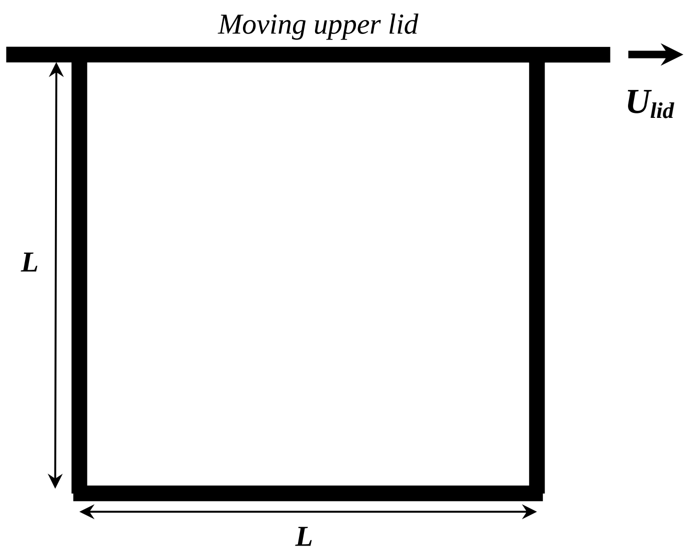

Figure 4.1 Two-dimensional lid-driven cavity

The moving upper lid creates adverse pressure gradient and influences the fluid in the cavity. Then the boundary layer separates from the solid walls and forms recirculating vortices. With the assumption of laminar flow in the cavity, a non-dimensional parameter, to describe the flow in the cavity, known as Reynolds number is defined as:

$$Re = \frac{U_{lid} L}{\nu} \tag{4.1}$$

where ν is the kinematic viscosity, L is the width of the square cavity and U_{lid} is the velocity of the upper sliding lid.

The steady two-dimensional lid-driven cavity has been studied and results are compared for a range of Reynolds numbers.

The staggered grid arrangement is used on the square flow domain. The schemes used in the discretisation equations require the values at the boundaries or outside the boundaries. For this reason, the boundary conditions have to be implemented.

As the pressure boundary condition, the pressure gradient normal to the solid boundaries is set to zero in the pressure correction equation.

$$\frac{\partial p}{\partial \bar{n}} = 0 \tag{4.2}$$

where $\bar{n}$ is normal to the wall.

As the velocity boundary condition for velocities, no slip boundary condition is applied to stationary walls to set the velocity values to zero. This condition can directly be applied if there is a velocity grid point on the solid boundary. Due to the staggered grid arrangement, sometimes velocity grid points are not located on the solid boundaries. If there are no velocity grid points on the solid boundary, then the velocity values are obtained by a simple linear interpolation from the neighboring grid points.

Then the boundary conditions for *u*-velocity in the lid-driven cavity used in the SIMPLE method becomes:

$$\begin{gathered} u(1, j) = u(nx, j) = 0 \quad u(i,1) + u(i,2) = 0 \\ u(i, ny) + u(i, ny-1) = 2U_{lid} \end{gathered} \tag{4.3}$$

Similarly boundary conditions for *v*-velocity are:

$$\begin{gathered} v(1, j) + v(2, j) = 0 \qquad v(i,1) = v(i, ny) = 0 \\ v(nx, j) + v(nx-1, j) = 0 \end{gathered} \tag{4.4}$$

4.2.2 Historical Background of the Lid-Driven Cavity

Steady separated flows are discussed over last decades in the case of the need for the simulation of complex fluid flows arises in engineering problems. Lid-Driven cavity is a SIMPLE physical problem for which numerical solutions of the Navier-Stokes equations describing the fluid motion can be obtained. As mentioned before, incompressible flows can be solved either by employing primitive variables or by vorticity-stream function formulation.

Burggraf [5] obtained both analytical solution and accurate numerical results for the structured steady separated flows for the Reynolds numbers ranging from 0 to 400 by using modified relaxation method. Then Bozeman and Dalton [6] made a numerical study for viscous flow in a cavity by using four different finite-difference schemes to solve governing equations to determine the effects of the grid sizes for Reynolds numbers 100 and 1000. Also numerical results for different aspect ratios (cavity height to width ratio) are present in this study. Bozeman and Dalton [6] found out that the nature of the vortex formed in the cavity depends on both the aspect ratio and Reynolds number. This study showed that for low Reynolds numbers vortex is located about three-quarters of the cavity height from the bottom and at mid-width. Most of the vortex strength is concentrated in the upper vortex (primary vortex) and with much smaller strength of two small counter rotating vortices (secondary vortices) located at each bottom corners [6]. As the Reynolds number increases, primary vortex moves to the center of the cavity and vortex becomes stationary with further increases in Reynolds number. Burggraf [5] mentioned that the secondary vortices were viscosity-dominated in contrast with the relatively non-viscous primary eddy. The secondary vortices occupy very small portion of the cavity and for this reason, the grid size should be increased to observe these vortices. However, the increase in the grid size increases the number of numerical iterations. For the numerical stability, the grid size must be decreased as the Reynolds number increases. This is one of the main problems in the numerical studies. Therefore, to observe the secondary vortices without increasing insufficiently the number of numerical iterations, most accurate grid size must be applied at higher Reynolds numbers. At Reynolds numbers as high as 10000, solutions are presented by Ghia and Shin [8] with uniform mesh refinement by using multigrid method. In this case, flow becomes highly unsteady, so uncertainties and inconsistencies in numerical solutions occur which cause turbulence. Keller and Schreiber [7] also achieved accurate numerical results over a range of Reynolds numbers. The researches that are mentioned above, have all used vorticity – stream function approach to solve the flow in the lid-driven cavity problem. However, in this study, primitive variable approach is considered by using the SIMPLE method. Thompson and Ferziger [19] used primitive variable approach and power-law scheme with an adaptive multigrid technique for the solution of incompressible Navier-Stokes equations. Solutions are obtained and tabulated for lid-driven cavity with Reynolds numbers up to 5000. Also in the study of Bruneau and Jouron [20], the steady Navier-Stokes equations are solved by primitive variables in the two-dimensional lid-driven cavity by means of a multigrid method. Results are obtained for Reynolds numbers as high as 15000 and it was stated that during the steady solution, the stability is lost for Reynolds numbers higher than 5000. Gjesdal and Lossius [21] performed numerical tests with the SIMPLE method and its variants for varying combinations of under-relaxation factors.

The solution technique using the SIMPLE method and its variants are applied to solve incompressible Navier-Stokes equations in this study. The results are discussed and compared with the ones obtained from above mentioned researches to illustrate how accurate the methods are for the first test case problem 'lid-driven cavity' at different Reynolds number.

In addition to this, the precise results, which are obtained by using different schemes and different grid arrangements, will also be shown to evaluate which scheme and mesh arrangement give better results.

4.2.3 Numerical Results over Various Reynolds Numbers

The steady two-dimensional lid driven cavity flow have been investigated for a range of Reynolds numbers, such as Re=100, 400, 1000, 5000 and 10000. Constant property laminar flow is assumed. For the initial guess, zero velocity and pressure field are applied. Uniformly spaced staggered grids are used unless otherwise noted.
For the SIMPLER method, while solving the discretised momentum equations, each calculation is continued until the residual for the *x*-momentum and *y*-momentum equations becomes smaller than 10^{-13}. In addition to this, the maximum value of the residual for the pressure correction equation is defined as 10^{-11}. At the correction step of the velocities, code is terminated when the error on *u* and *v* velocities become less than 10^{-6} or when 20000 iterations were exceed if otherwise is mentioned. Error*u* and error*v* is defined as the summation of the absolute difference between *u* and u^* at the each node divided with summation of the absolute value of *u* at each node.
Finally to compare the results with the ones in the literature, the appearance of the primary, secondary and the tertiary vortices, location of their centers and velocity profiles for *u* and *v* along the vertical and horizontal centerlines are presented.

4.2.3.1 Results for *Re*=100

In Figures 4.2 and 4.3, the *u*-velocity profiles along the vertical centerline and the *v*-velocity along the horizontal centerline are shown. The SIMPLER method and 129x129 uniformly spaced staggered grid arrangements is used for all three solutions which are carried out by upwind, hybrid and power law schemes. All three solutions are in agreement with the results of Ghia [8]. Also, the solution with the upwind scheme is acceptable at the extrema points of the *u*- and *v*- velocities when the Reynolds number is low.

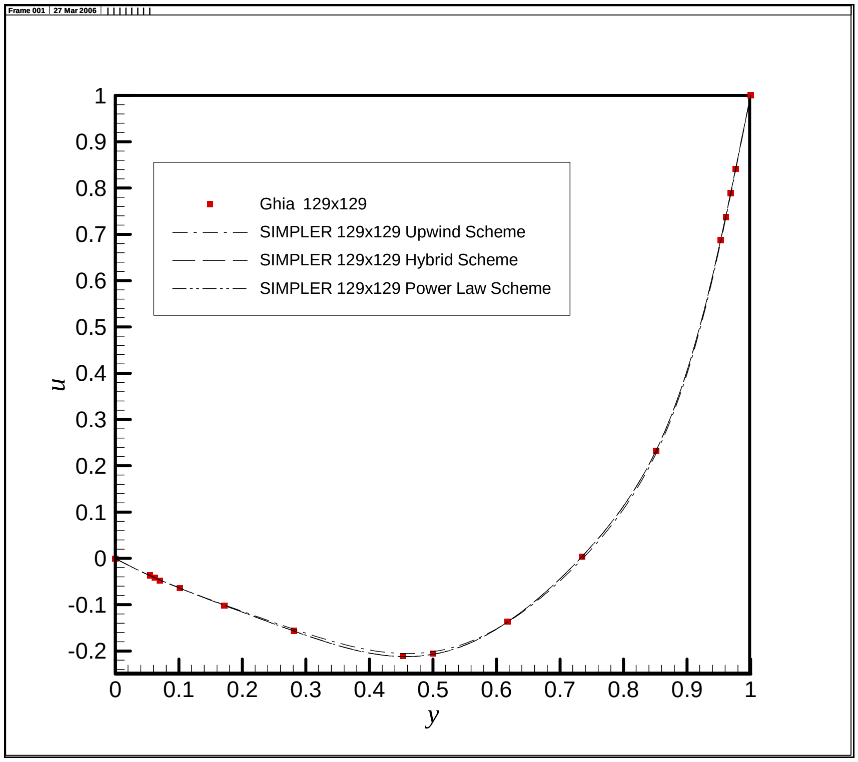

Figure 4.2 Vertical centerline *u*-velocity profiles for *Re*=100 with different schemes

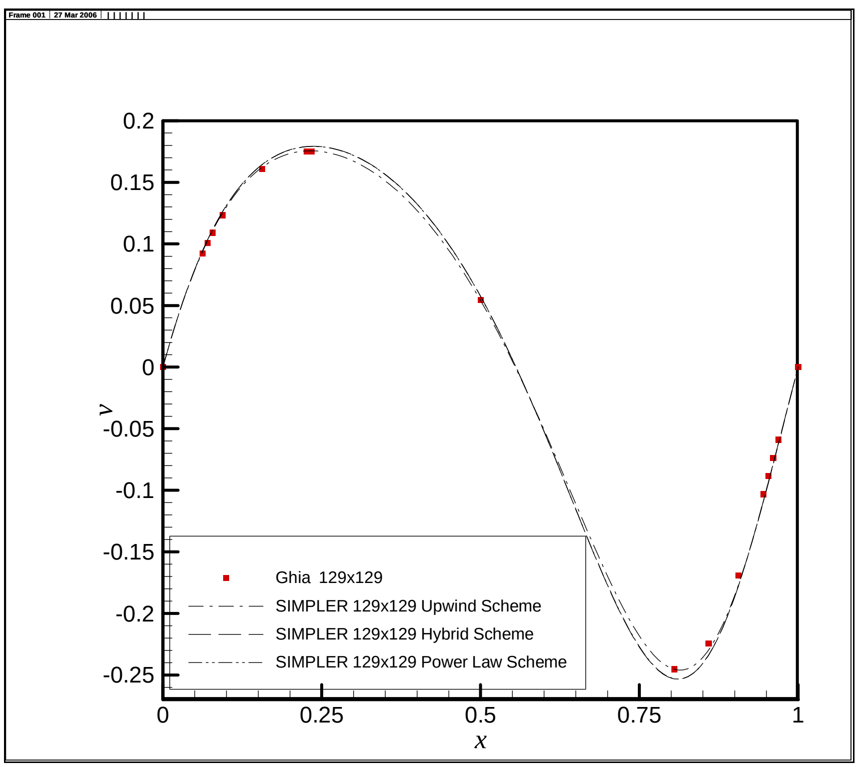

Figure 4.3 Horizontal centerline *v*-velocity profiles for *Re*=100 with different schemes

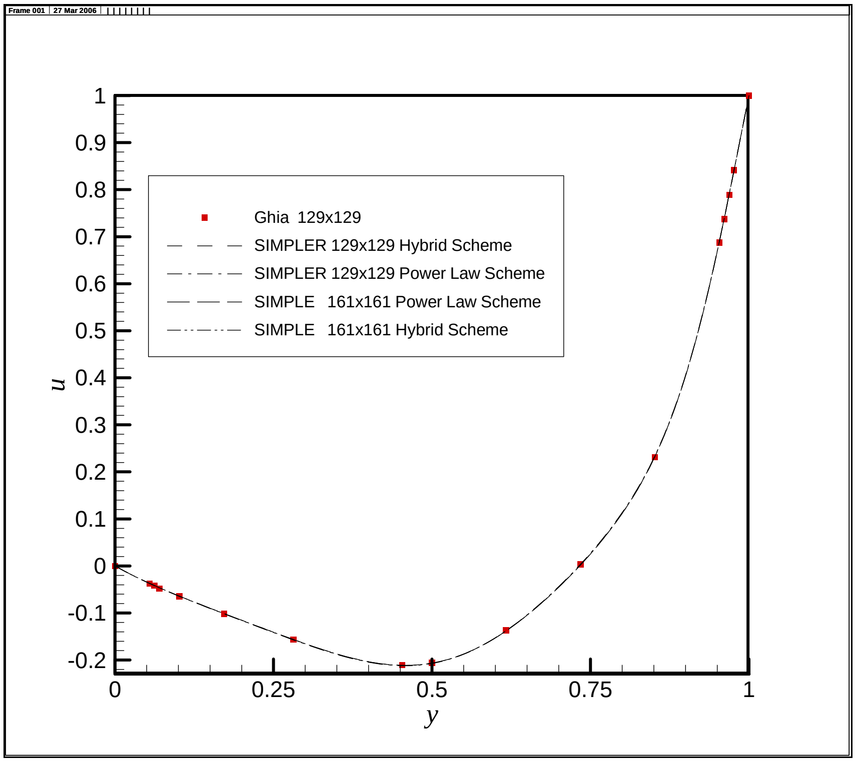

Figure 4.4 Vertical centerline *u*-velocity profiles for *Re*=100 with different algorithms

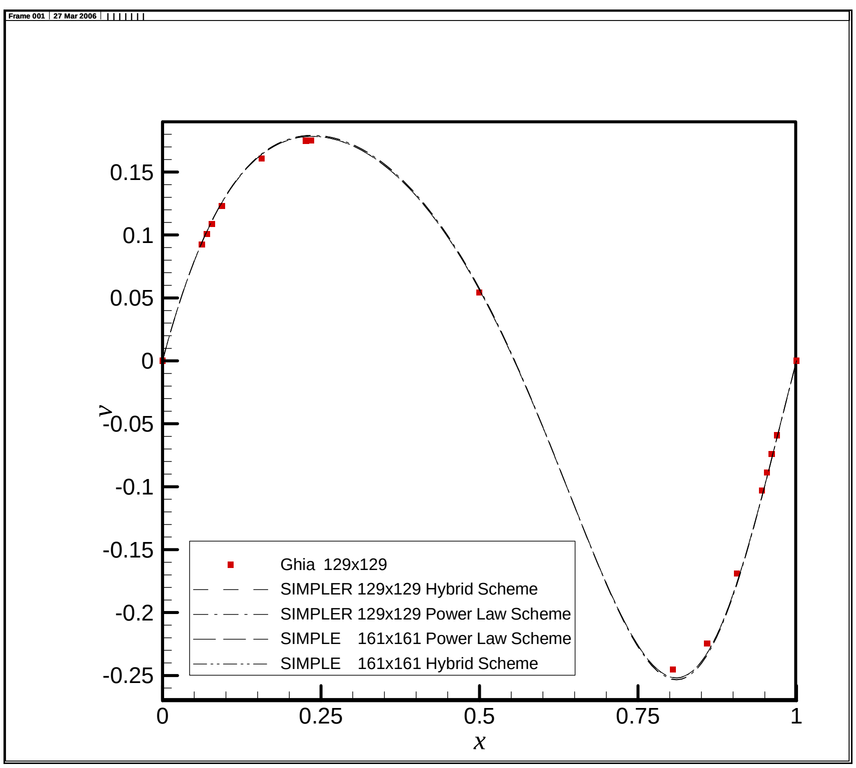

Figure 4.5 Horizontal centerline *v*-velocity profiles for *Re*=100 with different algorithms

It is seen from the Figures 4.2 and 4.3 that it is possible to obtain similar results with the first and second order differencing schemes. At such low Reynolds number flows, viscosity dominates the flow. Since at low Reynolds number flows, the influence of the flow transport in a coordinate direction is usually too small to significantly affect the transport profile in the other coordinate directions [3].

Figures 4.4 and 4.5 gives the solutions with both SIMPLE and SIMPLER method compared to the results of Ghia [8]. For the SIMPLE method, same results are obtained by using larger grid size than SIMPLER method such as 161x161. Moreover, it is obvious that using power law or hybrid schemes in both with SIMPLE and SIMPLER methods also converge to the same results. Table 4.2 shows comparison present results with published ones by presenting the centers of the primary and secondary vortices. Secondary vortices at bottom right and left are obtained for the grid size 161x161 with SIMPLE and SIMPLER method by using power law and hybrid schemes, whereas when the grid size is decreased to 129x129, only primary vortex is observed.

Table 4.1 Extrema of velocity profiles along centerlines
for the lid-driven square cavity at *Re*=100

***Re*=100**	**Grid Size**	**Extrema of velocity profiless along the centerlines**					
		u_{min}	y_{min}	v_{max}	x_{max}	v_{min}	x_{min}
Ghia, Ghia and Shin [8]	129x129	-0,2109	0,4531	0,1753	0,2344	-0,2453	0,8047
Bruneau and Jouron [20]	141x141	-0,2106	0,4531	0,1786	0,2344	-0,2521	0,8125
SIMPLE Power law	161x161	**-0,2113**	**0,4591**	**0,1784**	**0,2390**	**-0,2518**	**0,8113**
SIMPLE Hybrid	161x161	**-0,2115**	**0,4591**	**0,1784**	**0,2390**	**-0,2519**	**0,8113**
SIMPLER Hybrid	129x129	**-0,2060**	**0,4724**	**0,1650**	**0,2363**	**-0,2388**	**0,8189**
SIMPLER Hybrid	161x161	**-0,2127**	**0,4591**	**0,1794**	**0,2390**	**-0,2536**	**0,8110**

Table 4.2 Center locations of the vortices

for the lid-driven square cavity at Re=100

***Re*=100**	Grid Size	Primary vortex Location (x,y)	Secondary vortex Bottom right Location (x,y)	Secondary vortex Bottom left Location (x,y)
Ghia, Ghia and Shin [8]	129x129	(0.6172,0.7344)	(0.9454,0.0625)	(0.0313,0.0391)
Schreiber and Keller [7]	141x141	(0.6167,0.7417)	(0.9417,0.0500)	(0.0333,0.0250)
Bruneau and Jouron [20]	256x256	(0.6172,0.7344)	(0.9453,0.0625)	(0.0313,0.0391)
Vanka [28]	64x64	(0.6188,0.7375)	(0.9375,0.0563)	(0.0375,0.0313)
Gupta and Kalita [4]	41x41	(0.6125,0.7375)	(0.9375,0.0625)	(0.0375,0.0375)
Hou et. All [30]	-	(0.6196,0.7373)	(0.9451,0.0627)	(0.0392,0.0353)
SIMPLE Power law	**161x161**	**(0.6151,0.7382)**	**(0.9423,0.0616)**	**(0.0345,0.0345)**
SIMPLE Hybrid	**161x161**	**(0.6155,0.7382)**	**(0.9415,0.0623)**	**(0.0345,0.0343)**
SIMPLER Hybrid	**129x129**	**(0.6143,0.7363)**	**-**	**-**
SIMPLER Hybrid	**161x161**	**(0.6165,0.7363)**	**(0.9434,0.0625)**	**(0.0325,0.0376)**

Moreover, the extrema velocity values and their locations are presented in Table 4.1. As mentioned above, when grid size is 129x129, extrema velocity values are slightly different from the published results, whereas for a grid size of 161x161 the results for both method and schemes are in agreement with reference results in the literature.

For both SIMPLE and SIMPLER methods, first a secondary vortex in the bottom right corner appears when $Re \approx 100$. Primary vortex for grid sizes of 129x129 and 161x161 are identical to reference results in both methods by using power law and hybrid schemes.

Figures 4.6 and 4.7 show the streamlines for Re=100 obtained by SIMPLE method on a 161x161 uniformly spaced staggered grid arrangement with power law differencing scheme.

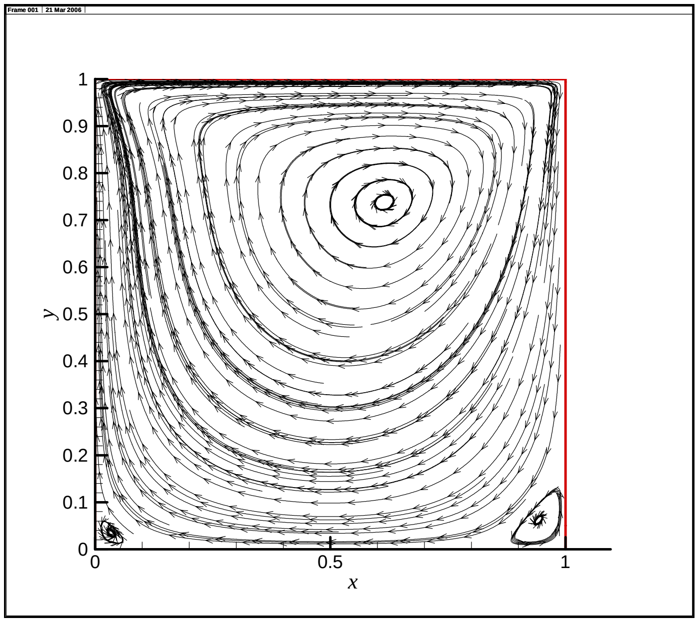

Figure 4.6 The streamlines for *Re*=100 by using the SIMPLE algorithm on a 161x161 mesh with the power law differencing scheme

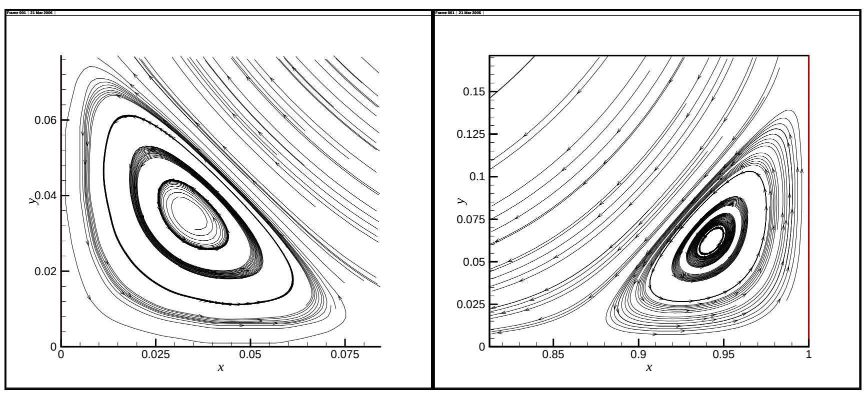

Figure 4.7 The streamlines at bottom right and left corners for *Re*=100 by using the SIMPLE algorithm on a 161x61 mesh with the power law differencing scheme

Finally for *Re*=100, the results of SIMPLER method on the clustered mesh of 129x129 is compared with the results of same method on a 129x129 uniform mesh. In Figures 4.8 and 4.9, it is seen that the results of both grid arrangements are identical to not only each other but also to the results of Ghia [8]. The advantage of using a clustered mesh is illustrated in Table 4.3. The number of successive iteration to reach the converged solution with clustered mesh arrangement is less than the number of iterations required for a uniform mesh. Moreover, if the number of iterations to get a converged solution with both SIMPLE and SIMPLER methods are compared, in the SIMPLE method, at least 20000 successive iterations are required till the residual becomes 10^{-3} whereas for SIMPLER method residual is 10^{-6} as indicated in Table 4.3.

Table 4.3 Number of iterations with SIMPLER algorithm on uniform and clustered meshes using hybrid and power law schemes for *Re*=100

***Re*=100**	Grid Size	Number of Iterations
SIMPLER Power law	**129x129**	**9710**
SIMPLER Hybrid	**129x129**	**8851**
SIMPLER Power law Clustered	**129x129**	**6436**
SIMPLER Hybrid Clustered	**129x129**	**6657**

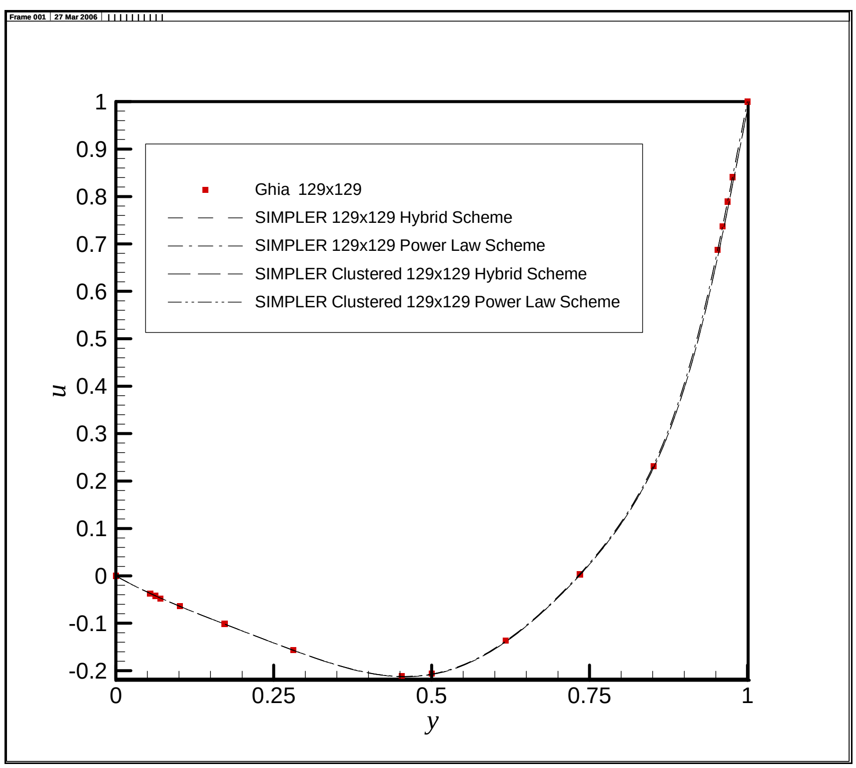

Figure 4.8 Vertical centerline *u*-velocity profiles for *Re*=100 by using clustered mesh

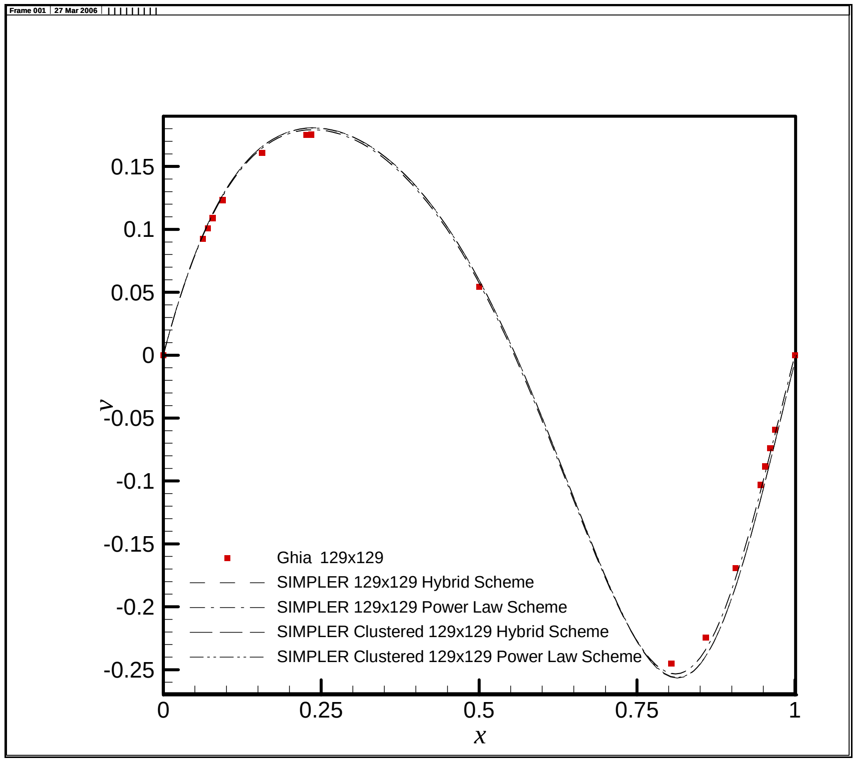

Figure 4.9 Horizontal centerline *v*-velocity profiles for *Re*=100 by using clustered mesh

In general, the results for *Re*=100 with SIMPLE and SIMPLER method by using different schemes and meshes exhibit an excellent match with the results in the literature.

4.2.3.2 Results for *Re*=400

After increasing the Reynolds number from 100 to 400, the comparison of the horizontal velocities on the vertical centerline and the vertical velocities on the horizontal centerline with different differencing schemes are presented in Figures 4.10 and 4.11 and comparison of the results with different methods are illustrated in the Figures 4.12 and 4.13.

The first order accurate upwind scheme leads to adequately acceptable convergent results as shown in Figure 4.10 and 4.11. However these results are not as close to Ghia's [8] results as the results obtained when the Reynolds number is 100.

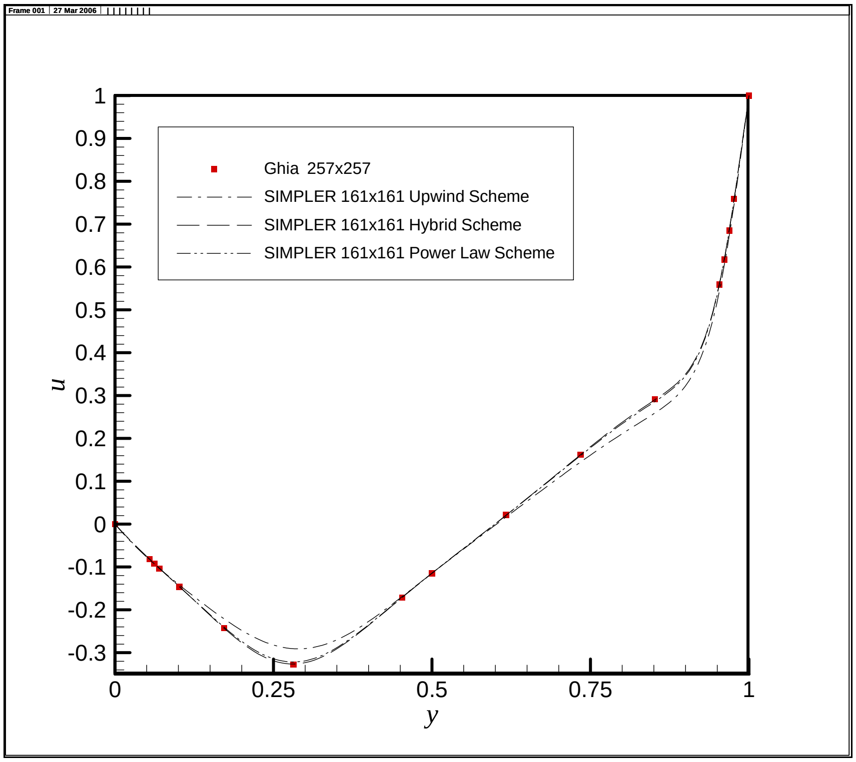

Figure 4.10 Vertical centerline *u*-velocity profiles for *Re*=400 with different schemes

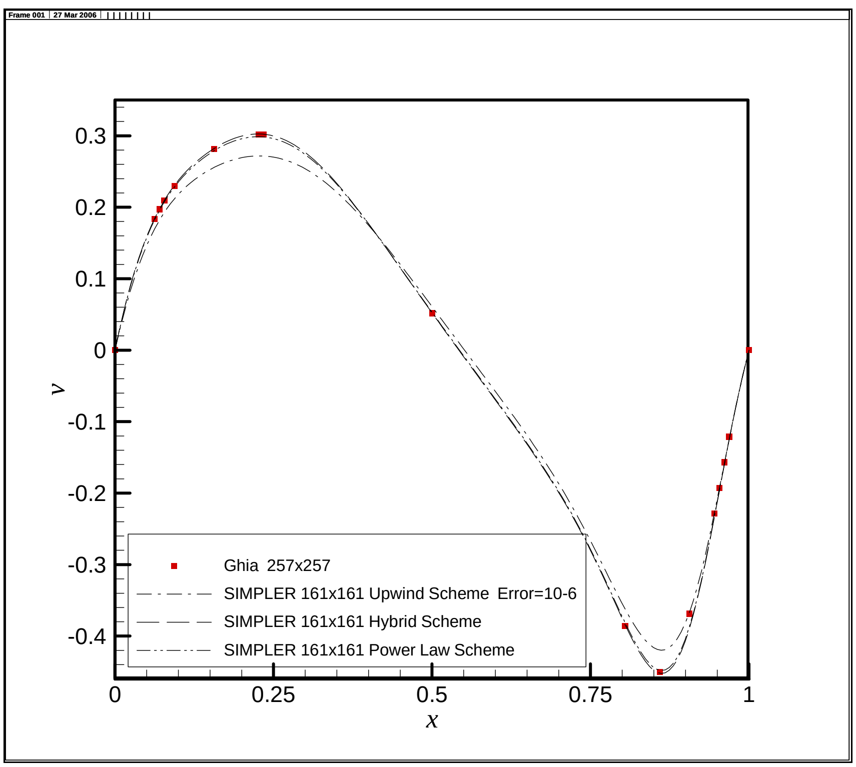

Figure 4.11 Horizontal centerline *v*-velocity profiles for *Re*=400 with different schemes

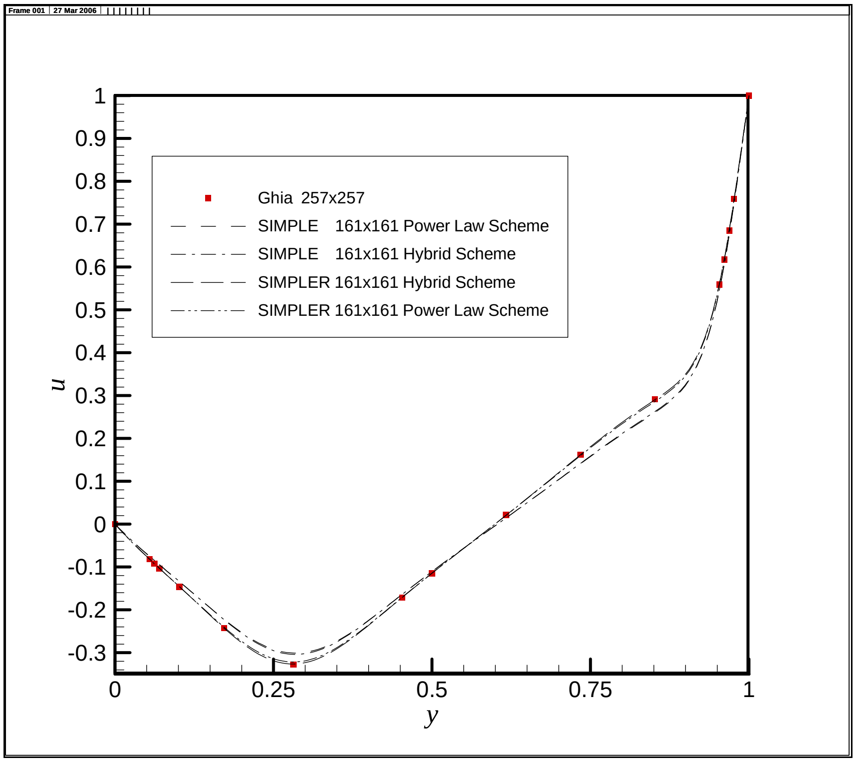

Figure 4.12 Vertical centerline *u*-velocity profiles for *Re*=400 with different algorithms

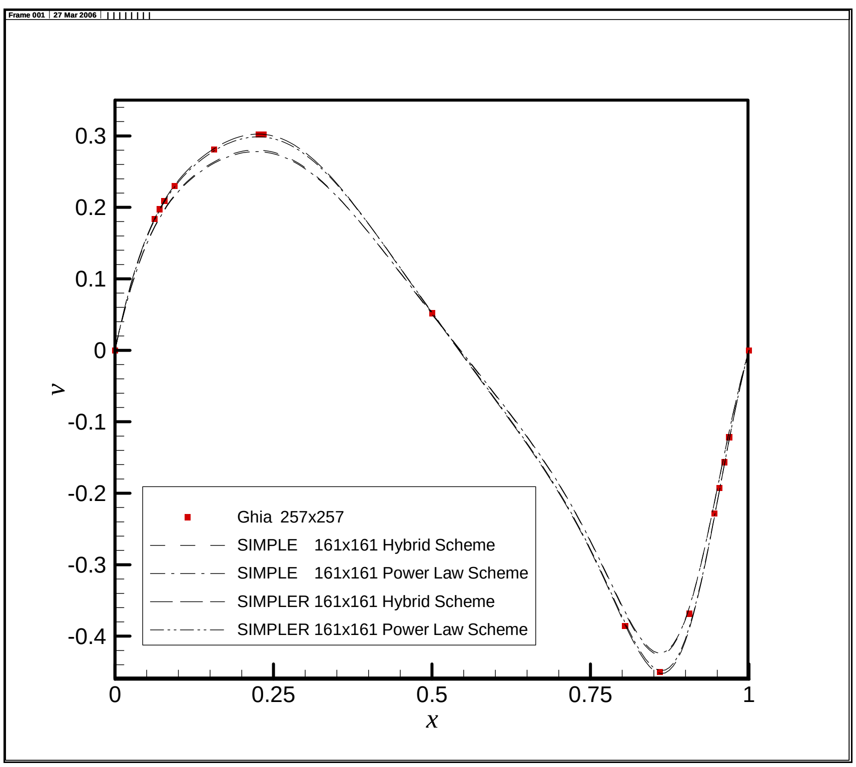

Figure 4.13 Horizontal centerline *v*-velocity profiles for *Re*=400 with different algorithms

While the results of Ghia [8] was obtained using a 257x257 grid, the same results are achieved by SIMPLER method with a 161x161 uniform grid using both power law and hybrid schemes.

If the SIMPLE and SIMPLER methods are compared, using Figures 4.12 and 4.13, it clear that the SIMPLER method is more close to the Ghia [8] results although results of the SIMPLE method is not significantly different. On the other hand, if the locations of the vortices, which are tabulated in Table 4.4, are considered, the location of the primary and secondary bottom right vortices are close to each other with both SIMPLE and SIMPLER methods using power law or hybrid schemes, whereas only SIMPLE method could indicate the secondary bottom left vortex. Also the results for the location of centers are in good agreement with the published results, as observed from Table 4.4.

Table 4.4 Location of the centers of the vortices
for the lid-driven square cavity at *Re*=400

***Re*=400**	Grid Size	Primary vortex Location (x,y)	Secondary vortex Bottom right Location (x,y)	Secondary vortex Bottom left Location (x,y)
Ghia, Ghia and Shin [8]	257x257	(0.5547,06055)	(0.8906,0.1250)	(0.0508,0.0469)
Schreiber and Keller [7]	141x141	(0.5571,06071)	(0.8857,0.1143)	(0.0500,0.0429)
Vanka [28]	64x64	(0.5563,0.6000)	(0.8875,0.1188)	(0.0500,0.0500)
Gupta and Kalita [4]	81x81	(0.5500,06125)	(0.8875,0.1250)	(0.0500,0.0500)
Hou et. All [30]		(0.5608,06078)	(0.8902,0.1255)	(0.0549,0.0510)
SIMPLE Power law	**161x161**	**(0.5590,0.6100)**	**(0.8863,0.1239)**	**(0.0487,0.0451)**
SIMPLE Hybrid	**161x161**	**(0.5582,0.6100)**	**(0.8854,0.1240)**	**(0.0489,0.0453)**
SIMPLER Power law	**161x161**	**(0.5551,0.6058)**	**(0.8867,0.1226)**	**-**
SIMPLER Hybrid	**161x161**	**(0.5543,0.6051)**	**(0.8845,0.1221)**	

***Re*=400**	Grid Size	Tertiary vortex Bottom right Location (x,y)	Tertiary vortex Bottom left Location (x,y)
Ghia, Ghia and Shin [8]	257x257	(0.9922,0.0078)	(0.0039,0.0039)

Ghia [8] found out tertiary bottom left and right vortices at a Reynolds number 400. However these vortices are not obtained by the other researchers.

From Figures 4.12 and 4.13, it is clear that SIMPLE method is not in agreement to Ghia [8] at the extrema points and the difference is illustrated in Table 4.5. Also the extrema velocity values along the centerlines, which are calculated with the SIMPLE and SIMPLER methods and are given in the mentioned references, are shown in Table 4.5.

Table 4.5 Extrema of velocity profiles along centerlines
for the lid-driven square cavity at *Re*=400

***Re*=400**	**Grid Size**	**Extrema of velocity profiles along the certerlines**					
		u_{min}	y_{min}	v_{max}	x_{max}	v_{min}	x_{min}
Ghia, Ghia and Shin [8]	257x257	-0,3273	0,2813	0,3020	0,2266	-0,4499	0,8594
Soh [10]	-	-0,312	0,288	-	-	-	-
SIMPLE Power law	161x161	**-0,3009**	**0,2830**	**0,2780**	**0,2201**	**-0,4234**	**0,8616**
SIMPLE Hybrid	161x161	**-0,3040**	**0,2830**	**0,2803**	**0,2201**	**-0,4358**	**0,8616**
SIMPLER Power law	161x161	**-0,3217**	**0,2830**	**0,2987**	**0,2264**	**-0,4482**	**0,8616**
SIMPLER Hybrid	161x161	**-0,3264**	**0,2830**	**0,3025**	**0,2264**	**-0,4522**	**0,8616**

In Figure 4.14, the streamlines obtained by SIMPLE method using power law differencing scheme on a 161x161 grid are presented. The primary vortex as well as the secondary vortices in the bottom corners of the cavity are observed. The secondary vortices dominate more space than these at a Reynolds number of 100 and these secondary vortices are shown in Figure 4.15. The streamlines of the other there calculations shown in the Figures 4.12 and 4.13 are in agreement with the streamlines shown in Figures 4.14 and 4.15. Since the location of the center of primary and secondary vortices are close to each other and it can be seen from Table 3.4 and 3.5, the size and shape of those vortices are also relevant to each other.

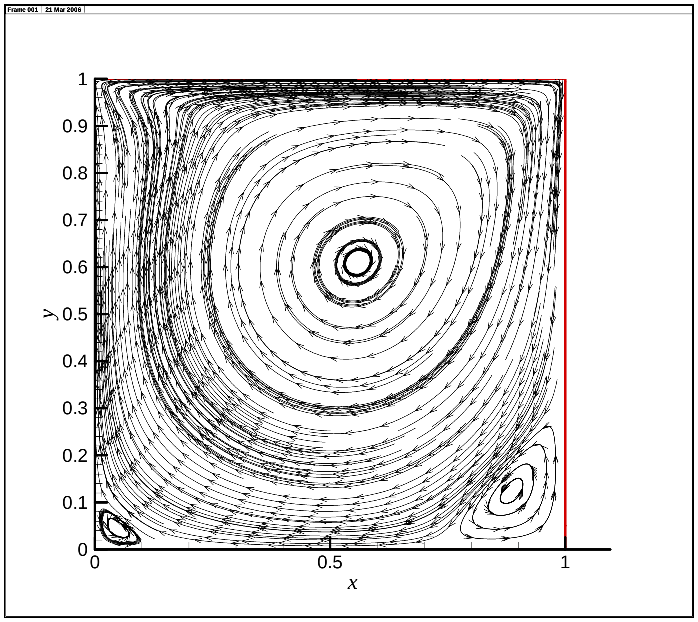

Figure 4.14 The streamlines for *Re*=400 by using the SIMPLE algorithm on a 161x161 mesh with the power law differencing scheme

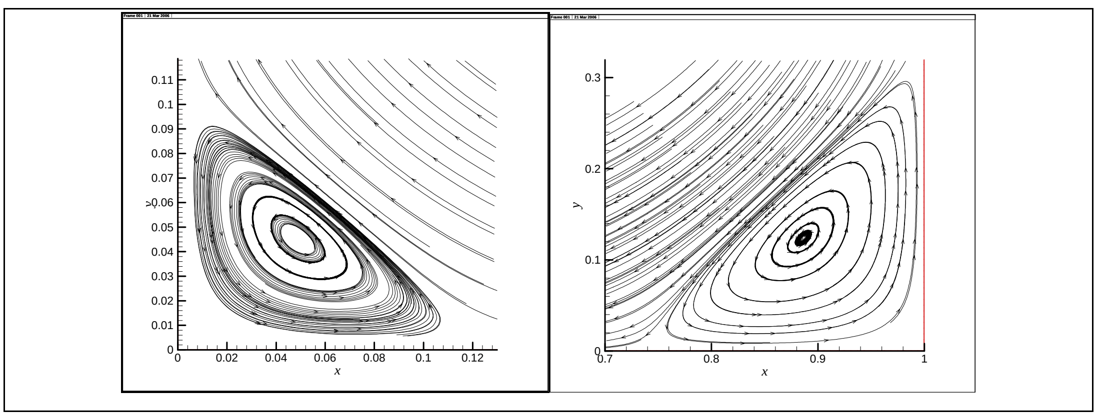

Figure 4.15 The streamlines at bottom right and left corners for *Re*=400 by using the SIMPLE algorithm on a 161x61 mesh with the power law differencing scheme

Figures 4.16 and 4.17 show results of velocity profiles along the centerlines by SIMPLER method using 129x129 and 161x161 uniform and clustered meshes with the power law differencing scheme. 161x161 uniform mesh grid size gives slightly better results than 129x129 uniform meshes. The power law solution becomes grid independent when the grid size is around 161x161.

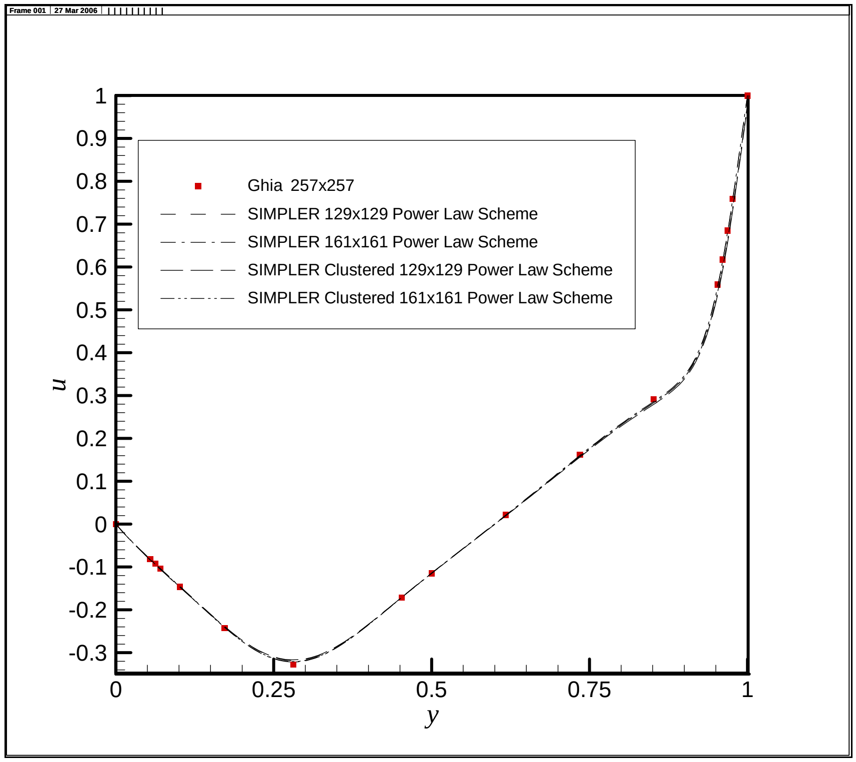

Figure 4.16 Vertical centerline *u*-velocity profiles for *Re*=400 by using clustered mesh

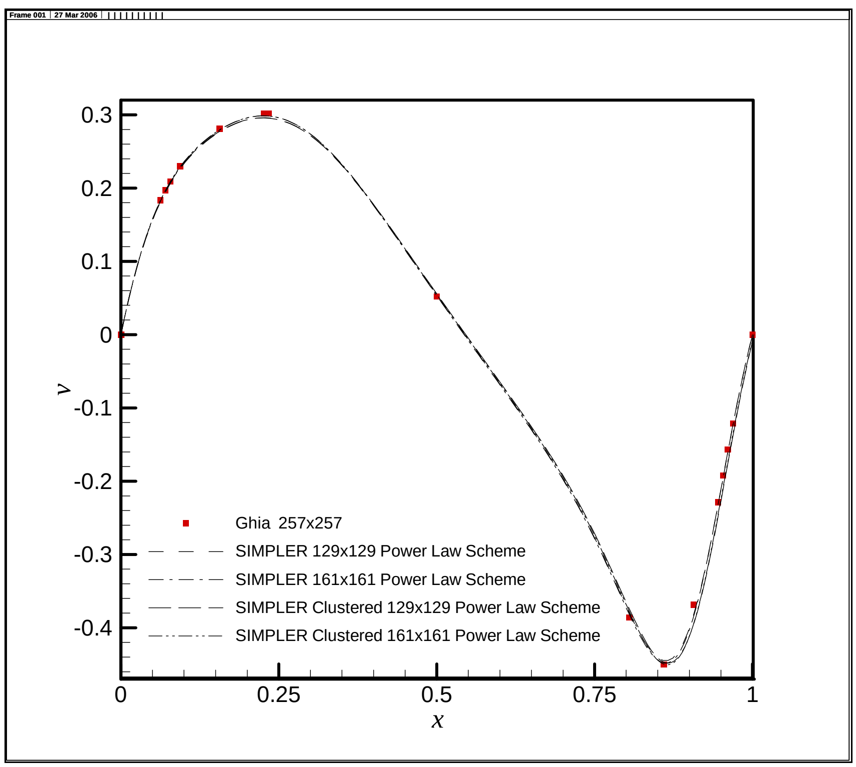

Figure 4.17 Horizontal centerline *v*-velocity profiles for *Re*=400 by using clustered mesh

If the results of clustered and uniform meshes are compared, it is observed that both of mesh types converge to the same solution with the same grid sizes. However, the number of the iterations to reach a converged solution is considerably different. To get a converged solution by using clustered mesh requires significantly less iterations than that of uniform mesh as indicated in Table 4.6. Also, the same results are obtained by using both 161x161 and 129x129 clustered meshes, whereas 161x161 clustered mesh converges by making less iteration than the 129x129 clustered mesh. For this reason, it is effective to use clustered mesh in the regions with high flow gradients, such as; boundary layers, corners where the secondary or tertiary vortices are located.

Table 4.6 Number of Iterations with SIMPLER algorithm on uniform and clustered meshes using hybrid and power law schemes for Re=400

***Re*=400**		Grid Size	Number of Iterations
SIMPLER	Power law	**129x129**	**5381**
SIMPLER	Power law	**161x161**	**6871**
SIMPLER	Hybrid	**161x161**	**6496**
SIMPLER	Power law Clustered	**129x129**	**2491**
SIMPLER	Power law Clustered	**161x161**	**1073**

4.2.3.3 Results for *Re*=1000

Re=1000 is an another test case, due to the presence of significant cross transport through-out the domain of the flow[3]. The centerline velocity profiles computed by different differencing schemes are shown in Figures 4.18 and 4.19. Both solutions with power law and hybrid schemes have perfect match with Ghia's [8] solutions whereas results for upwind scheme slightly deviates. Moreover, if the results obtained with the upwind scheme at the Reynolds number of 100, 400, 1000 are considered, it is obvious that the results of upwind scheme deviates far from the

Ghia's [8] solution as the Reynolds number increases. Since the flow in the cavity becomes more diffusive as the Reynolds number increases. Therefore, first order upwind scheme is not suitable to calculate convection term more precisely. It is obvious from Figures 4.18 and 4.19 that power law and hybrid schemes are more diffusive than the upwind scheme but hybrid scheme gives slightly better results than the power law and this can also be seen in Tables 4.7 and 4.8.

After reaching the conclusion that the hybrid scheme gives more precise results, the results of velocity profiles along the centerline calculated by SIMPLER method using hybrid scheme with different grid sizes are compared in Figures 4.20 and 4.21. Although 129x129 and 161x161 uniform grids converged to the Ghia's [8] solutions, 161x161 fine grid gives better results. The solution becomes grid independent when the grid size is 161x161. However the results, obtained by using uniform medium grid sizes such as 61x61, are not close to reference one in the literature.

The velocity profiles along the centerline with SIMPLE and SIMPLER method by using hybrid scheme with two different grid sizes are compared in the Figures 4.22 and 4.23. The results of the velocity profiles with SIMPLE Method are not close to Ghia's [8] solution when the grid size is 161x161, but as mentioned above SIMPLER method on grid size 161x161 is in excellent agreement with the Ghia's [8] results. As the grid size increases from 161x161 to 257x257, SIMPLE method gives better accuracy. The number of iterations required to obtain a converged solution in the SIMPLE method is larger than the one required for SIMPLER method. This is not only time consuming but also creates more computational load.

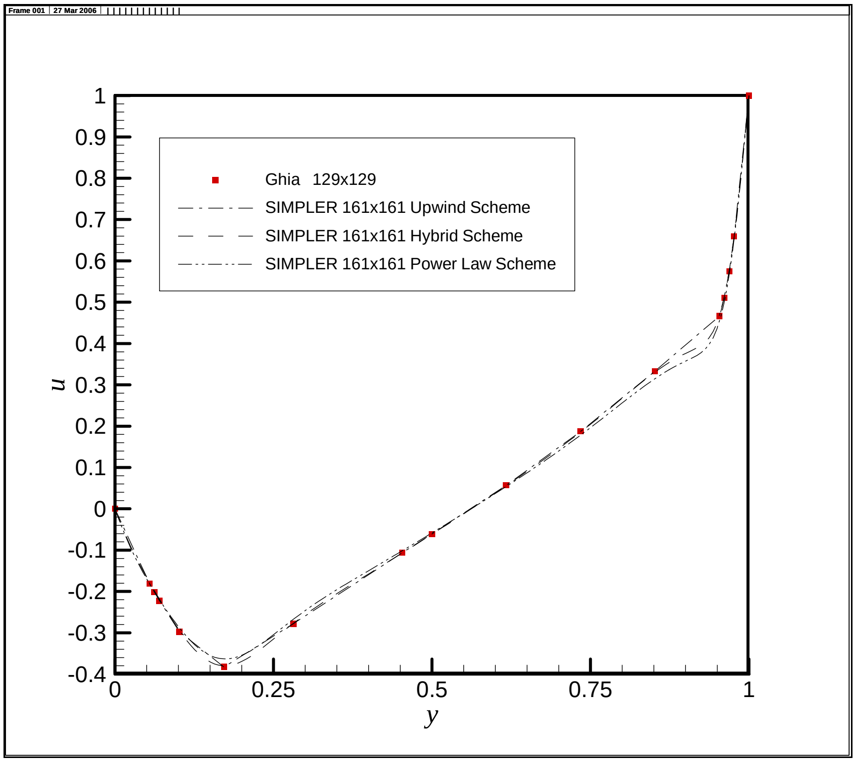

Figure 4.18 Vertical centerline *u*-velocity profiles for *Re*=1000 with different schemes

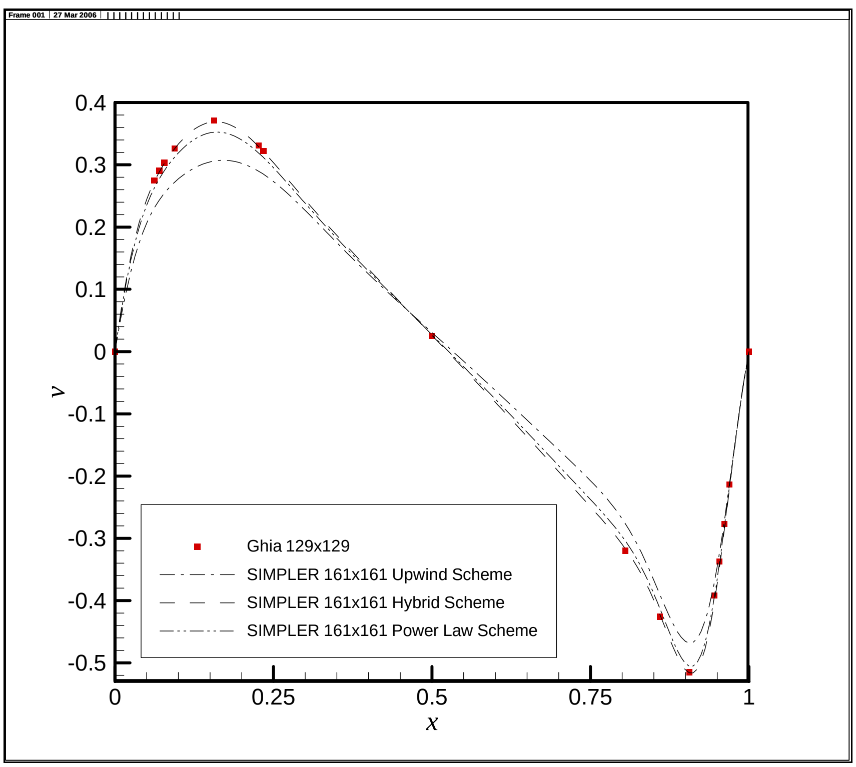

Figure 4.19 Horizontal centerline *v*-velocity profiles for *Re*=1000 with different schemes

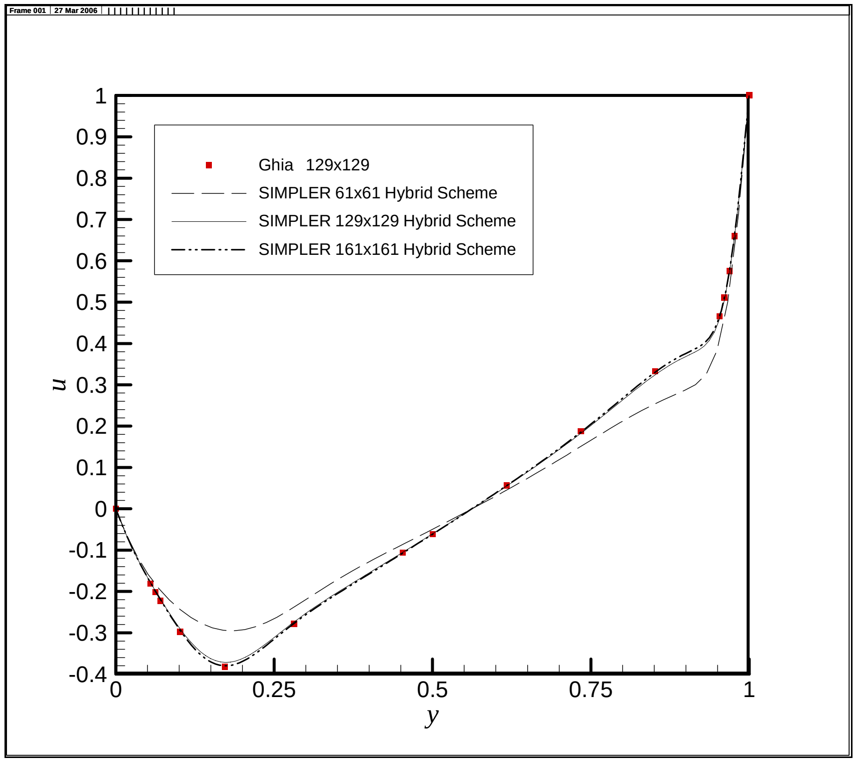

Figure 4.20 Vertical centerline *u*-velocity profiles for *Re*=1000 with different grid sizes

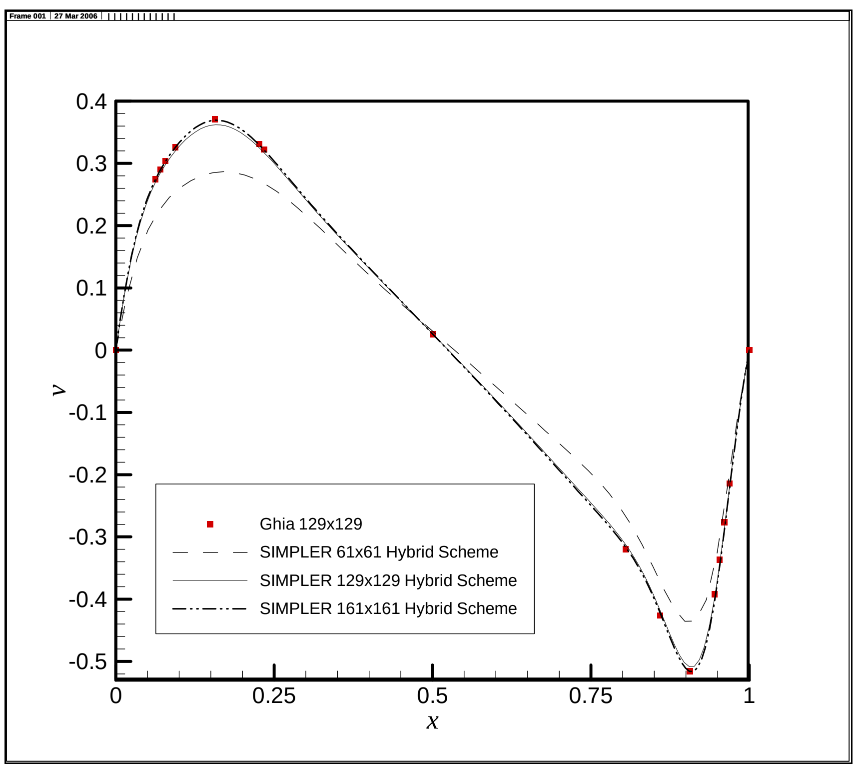

Figure 4.21 Horizontal centerline *v*-velocity profiles for *Re*=1000 with grid sizes

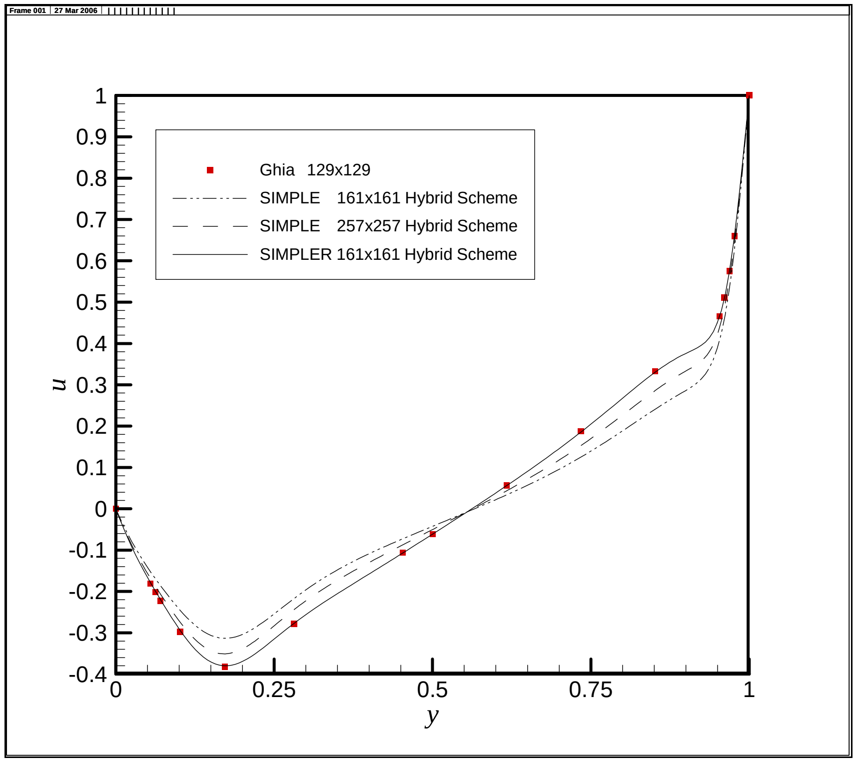

Figure 4.22 Vertical centerline *u*-velocity profiles for *Re*=1000 with different algorithms

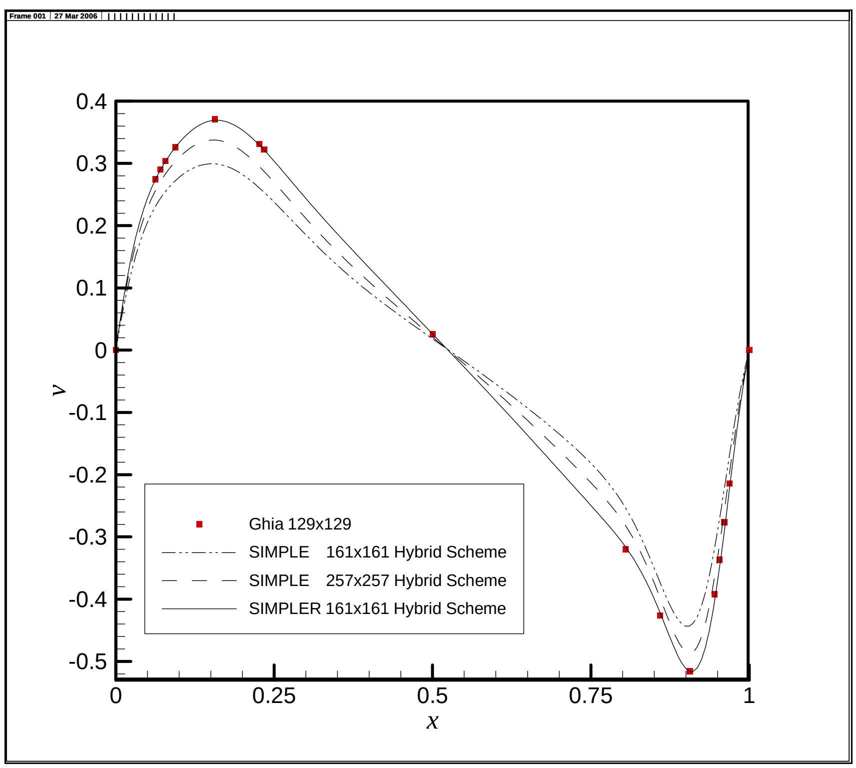

Figure 4.23 Horizontal centerline *v*-velocity profiles for *Re*=1000 with different algorithms

The extrema points of the velocity profiles, shown in Figures 4.18 through 4.23, are tabulated in the Table 4.7. The extrema values for different methods, different schemes and different grid sizes can be compared with the results of Ghia [8], Bruneau and Jouron [20], Vanka [24] and Soh [10].

It is obvious from Table 4.7 that the result of SIMPLER method by using hybrid scheme on 161x161 grid size gives the best result.

Table 4.7 Extrema of velocity profiles along centerlines
for the lid-driven square cavity at *Re*=1000

***Re*=1000**	**Grid Size**	**Extrema of velocity profiles along the certerlines**					
		u_{min}	y_{min}	v_{max}	x_{max}	v_{min}	x_{min}
Ghia, Ghia and Shin [8]	257x257	-0,3829	0,1719	0,3709	0,1563	-0,5155	0,9063
Bruneau and Jouron [20]	-	-0,3764	0,1602	0,3665	0,1523	-0,5208	0,9102
Vanka [28]	-	-0,3798	0,168	0.3669	0,1563	0,5186	0,9102
Soh [10]	-	-0,372	0,185	-	-	-	-
SIMPLE Hybrid	161x161	**-0,3133**	**0,1698**	**0,2996**	**0,1509**	**-0,4535**	**0,8994**
SIMPLE Hybrid	257x257	**-0,3504**	**0,1765**	**0,3375**	**0,1569**	**-0,4858**	**0,9020**
SIMPLER Power law	161x161	**-0,3631**	**0,1761**	**0,3526**	**0,1635**	**-0,5053**	**0,9057**
SIMPLER Hybrid	129x129	**-0,3716**	**0,1732**	**0,3621**	**0,1575**	**-0,5086**	**0,9055**
SIMPLER Hybrid	161x161	**-0,3798**	**0,1761**	**0,3693**	**0,1572**	**-0,5161**	**0,9120**

Table 4.8 indicates the location of primary and secondary vortices. Although the velocity profiles calculated by SIMPLE method does not perfectly match with Ghia's [8] results, the location of centers of primary and secondary bottom right vortices obtained by SIMPLE method is in agreement with Ghia's [8] results and other references. The SIMPLE method is not effective in observing the location of secondary bottom right vortex. The center of the secondary bottom right vortex, which is obtained by the SIMPLE method, is more close to bottom right corner than the SIMPLER method. Therefore, the strength of the secondary bottom right vortex observed with SIMPLE method is smaller than the SIMPLER method. On

the other hand, the location centers of the vortices, which are obtained by the SIMPLER, are identical to the results in the literature whether differencing scheme is power law or hybrid. If the results in the literature are considered, only Ghia [8] observed a tertiary vortex at the bottom right, whereas only Bruneau and Jouron [20] could obtain secondary top left and tertiary bottom left vortex by using 256x256 mesh. The spaces in the cavity occupied by the vortices evaluated by SIMPLER method are same as the ones in the literature.

Table 4.8 Location of the centers of the vortices for the lid-driven square cavity at *Re*=1000

***Re*=1000**	Grid Size	Primary vortex Location (x,y)	Secondary vortex Bottom right Location (x,y)	Secondary vortex Bottom left Location (x,y)
Ghia, Ghia and Shin [8]	129x129	(0.5313,0.5625)	(0.8594,0.1094)	(0.0859,0.0781)
Schreiber and Keller [7]	141x141	(0.5286,0.5643)	(0.8643,0.1071)	(0.0857,0.0714)
Bruneau and Jouron [20]	256x256	(0.5313,0.5586)	(0.8711,0.1094)	(0.0859,0.0820)
Vanka [28]	256x256	(0.5313,0.5664)	(0.8672,0.1133)	(0.0820,0.0781)
Vanka [28]	64x64	(0.5438,0.5625)	(0.8625,0.1063)	(0.0750,0.0831)
Gupta and Kalita [4]	81x81	(0.5250,0.5625)	(0.8625,0.1125)	(0.0875,0.0750)
Hou et. All [30]		(0.5333,0.5647)	(0.8667,0.1137)	(0.0902,0.0784)
SIMPLE Power law	**161x161**	**(0.5358,0.5703)**	**(0.8686,0.1150)**	**(0.0786,0.0704)**
SIMPLE Hybrid	**161x161**	**(0.5347,0.5711)**	**(0.8677,0.1157)**	**(0.0780,0.0700)**
SIMPLE Hybrid	**257x257**	**(0.5326,0.5677)**	**(0.8661,0.1135)**	**(0.0808,0.0742)**
SIMPLER Power law	**161x161**	**(0.5333,0.5631)**	**(0.8661,0.1119)**	**(0.0818,0.0783)**
SIMPLER Hybrid	**129x129**	**(0.5321,0.5660)**	**(0.8655,0.1131)**	**(0.0827,0.0768)**
SIMPLER Hybrid	**161x161**	**(0.5313,0.5683)**	**(0.8641,0.1124)**	**(0.0841,0.0775)**
***Re*=1000**	Grid Size	Secondary vortex Top Left Location (x,y)	Tertiary vortex Bottom right Location (x,y)	Tertiary vortex Bottom left Location (x,y)
Ghia, Ghia and Shin [8]	129x129	-	(0.9922,0.0078)	-
Bruneau and Jouron [20]	256x256	(0.0039,1.0000)	-	(0.0039,0.0039)

In conclusion, the most accurate result with the SIMPLER algorithm is obtained for 161x161 uniform grid by using the hybrid differencing scheme. With SIMPLE method, the most accurate solution is obtained when the uniform grid size is 257x257 by using the hybrid differencing scheme. The streamlines obtained for these two results are illustrated in Figures 4.24 and 4.26. Also the Figures 4.25 and 4.27 show the right and left bottom corners more closely to compare how much space is occupied by the secondary vortices in the left and right bottom of the cavity.

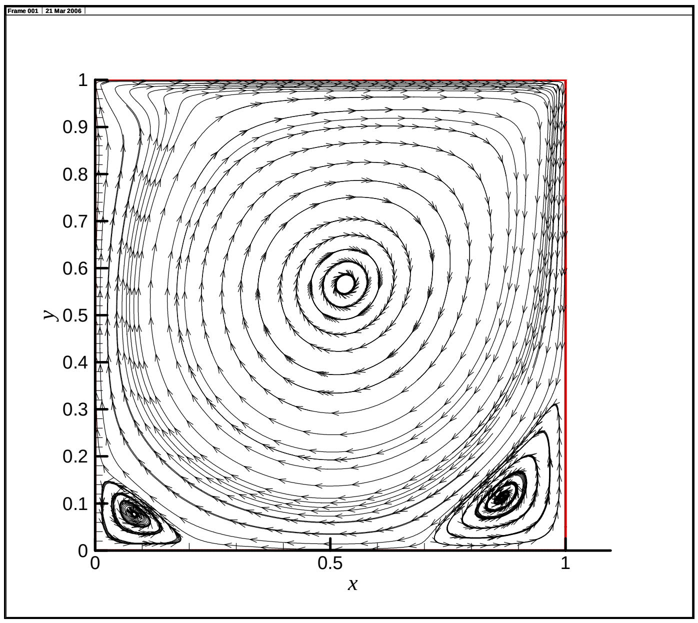

Figure 4.24 The streamlines for *Re*=1000 on a 161x161 mesh by using the SIMPLER algorithm with the hybrid differencing scheme

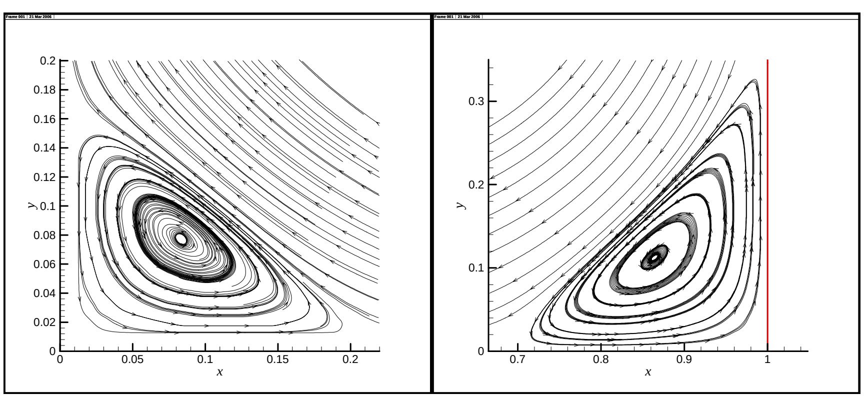

Figure 4.25 The streamlines at bottom right and left corners for *Re*=1000 on a 161x161 mesh by using the SIMPLER algorithm with the hybrid differencing scheme

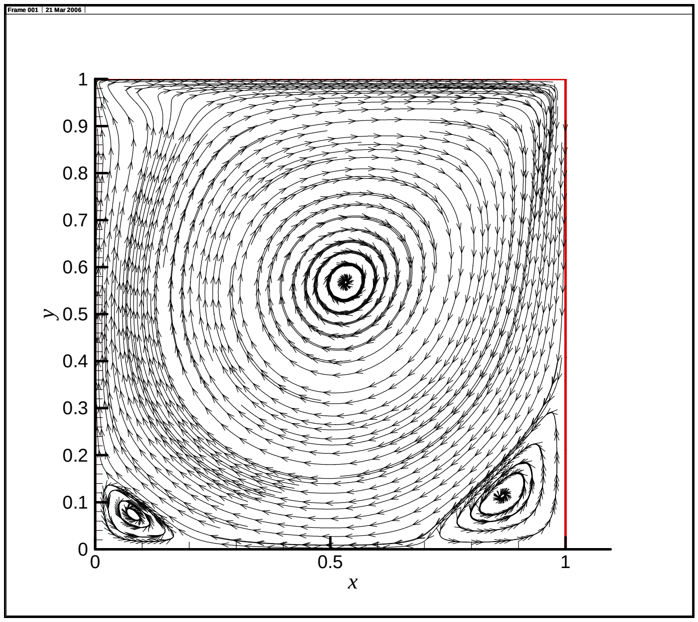

Figure 4.26 The streamlines for *Re*=1000 on a 257x257 mesh by using the SIMPLE algorithm with the hybrid differencing scheme

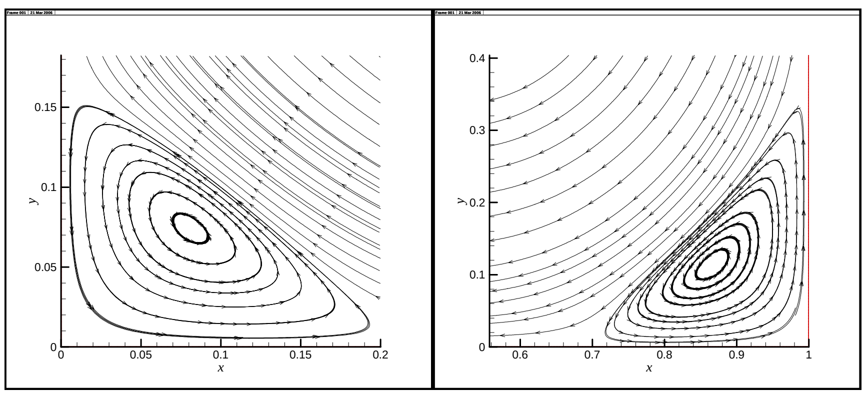

Figure 4.27 The streamlines at bottom right and left corners for *Re*=1000 on a 257x257 mesh by using SIMPLE algorithm with the hybrid differencing scheme

When the space occupied by the left and right bottom vortices are checked from Figures 4.25 and 4.26, it is obvious that the space occupied in the solution by the SIMPLE method on 257x257 grid with hybrid scheme is larger than the one for the SIMPLER method. So the strength of the bottom left and right vortices of the SIMPLE method using the hybrid scheme with 257x257 grid size is higher.

Velocity profiles along centerlines with SIMPLER method using power law scheme both with clustered and uniform mesh are shown in Figures 4.28 and 4.29. It can be observed from Figures 4.28.and 4.29; the results both with clustered and uniform mesh by the SIMPLER algorithm using the power law scheme on a 161x161 grid are identical to each other. The result obtained by the SIMPLER algorithm on a 129x129 clustered mesh with the same scheme is also close to the other two results. However when the number of iterations is considered, it is seen from Table 4.9 that using clustered mesh does not reduce computational effort at Re=1000. Results on clustered mesh at *Re*=100 and 400 take less number of iterations than using uniform mesh and it is less time consuming. However when the Reynolds number increased to 1000, using clustered mesh can not change the number of iterations required to reach the converged solution, as can be observed from Table 4.9. When the Reynolds number is 100 or 400, the strength of the bottom left and right vortices are smaller and the space occupied by these vortices are less than the corresponding ones at Re=1000. For this reason; there is no need to use clustered mesh near the boundaries or near the corners to obtain the vortices at the bottom right and left corners.

Table 4.9 Number of iterations with SIMPLER algorithm on uniform and clustered meshes using hybrid and power law schemes for *Re*=1000

***Re*=1000**	Grid Size	# of Iterations
SIMPLER Hybrid	**129x129**	**304**
SIMPLER Hybrid	**161x161**	**418**
SIMPLER Power law	**161x161**	**400**
SIMPLER Power law Clustered	**129x129**	**316**
SIMPLER Power law Clustered	**161x161**	**506**

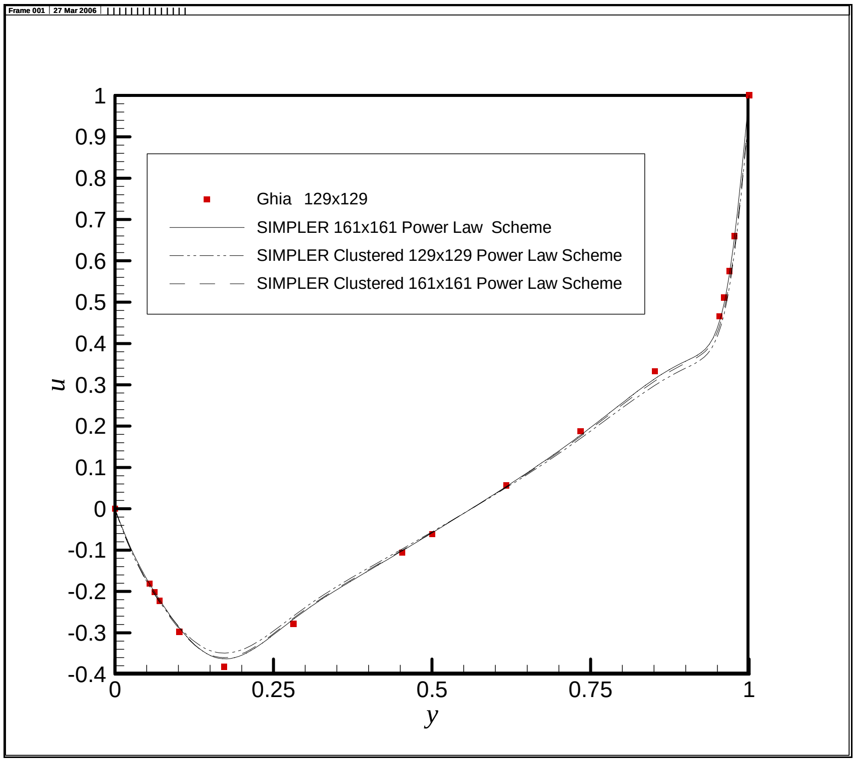

Figure 4.28 Vertical centerline *u*-velocity profiles for *Re*=1000 by using clustered mesh

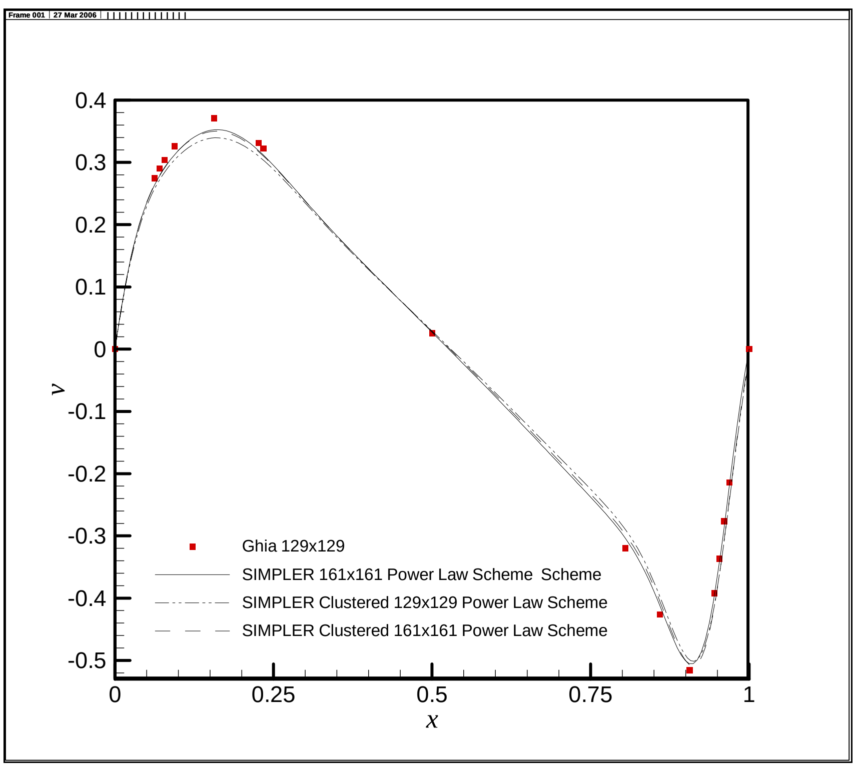

Figure 4.29 Horizontal centerline *v*-velocity profiles for *Re*=1000 by using clustered mesh

The strength of these vortices at Re=1000 is high enough to observe it by using a uniform mesh. Calculations are carried out on both 129x129 and 161x161 meshes and both with clustered and uniform mesh by SIMPLER method. For both mesh sizes, the number of iterations required on uniform meshes is slightly less than the number of iterations required on clustered mesh.

4.2.3.5 Convergence Data and CPU Times

The converged solutions are obtained on a PC with double Xeon 2.4 hyper threading processor and 1GB RAM. The converged solution to a residual value of 10^{-5} with SIMPLER method by using hybrid differencing scheme for *Re*=100 is obtained in about 18 minutes, for *Re*=400 in about 28 minutes and for *Re*=1000 in about 37 minutes of computation time. In Table 4.9, the convergence data and CPU times for different Reynolds number on different grid arrangements with different grid sizes by using Hybrid differencing scheme are presented.

A five order drop in magnitude of velocity residuals is sufficient to achieve converged solution [3]. As expected, the convergence to a lower residual value requires larger number of iterations.

It is obvious from the Table 4.9 that the converged solution for larger Reynolds numbers is achieved by larger number of iterations.

When clustered meshes are used to converge to a residual larger than 10^{-5} on same grid size with same algorithm, not only the convergence rates, but also number of iterations, are noticeably increased. However when the order of residual is decreased to 10^{-6} or 10^{-7}, using clustered meshes reduce the computational effort and take less number of iterations as presented in Tables 4.3 and 4.6.

For a given Reynolds and grid size, the SIMPLE algorithm requires more CPU time than the SIMPLER algorithm to converge to the same residual. Although the each iteration step of SIMPLER algorithm has more computational load than the SIMPLE algorithm, each iteration step SIMPLER algorithm converges more accurate result than the SIMPLE algorithm’s each iteration step. Therefore, SIMPLER algorithm converges to accurate result than SIMPLE algorithm. The fact that SIMPLE algorithm requires extra effort to iterate on the velocity correction step than the SIMPLER algorithm.

Although the SIMPLE algorithm makes at least 200000 iterations in about 300 minutes for Re=100, at least 200000 iterations in about 400 minutes for Re=400 and at least 200000 iterations in about 700 minutes for Re=1000, it can not reach to the residual value of 10^{-3}.

Table 4.9 Convergence data and CPU Times for the lid-driven cavity problem up to Re=1000

Algorithm and Scheme Types	Reynolds Number	Grid Size	Residual	CPU Time (min) ≈	Iteration
SIMPLE Hybrid	100	161x161	1,E-03	302	≈200000
SIMPLER Hybrid	100	129x129	1,E-03	18	29
SIMPLE Hybrid Clustered	100	161x161	1,E-03	271	≈200000
SIMPLER Hybrid Clustered	100	129x129	1,E-03	19	37
SIMPLER Hybrid	100	129x129	1,E-05	43	346
SIMPLER Hybrid Clustered	100	129x129	1,E-05	44	1440
SIMPLE Hybrid	400	161x161	1,E-03	422	≈200000
SIMPLER Hybrid	400	161x161	1,E-03	28	40
SIMPLE Hybrid Clustered	400	161x161	1,E-03	355	200000
SIMPLER Hybrid Clustered	400	161x161	1,E-03	71	35
SIMPLER Hybrid	400	161x161	1,E-05	134	281
SIMPLER Hybrid Clustered	400	161x161	1,E-05	209	322
SIMPLE Hybrid	1000	257x257	1,E-03	755	≈200000
SIMPLER Hybrid	1000	129x129	1,E-03	34	53
SIMPLER Hybrid	1000	129x129	1,E-05	54	234
SIMPLER Hybrid Clustered	1000	129x129	1,E-05	59	246
SIMPLER Hybrid	1000	161x161	1,E-03	37	53
SIMPLE Hybrid Clustered	1000	257x257	1,E-03	617	≈200000
SIMPLER Hybrid Clustered	1000	161x161	1,E-03	81	57
SIMPLER Hybrid	1000	161x161	1,E-05	83	234
SIMPLER Hybrid Clustered	1000	161x161	1,E-05	186	327

4.2.3.5 Results for *Re*=5000

A rather difficult test case is obtained as the Reynolds number is increased to 5000. The velocity profiles along the vertical and horizontal centerlines of the square cavity, which are obtained by using SIMPLE algorithm, are shown in Figures 4.30 and 4.31. Moreover the results of the velocity profiles with the SIMPLER algorithm are illustrated in Figures 4.32 and 4.33. These results, which are shown in Figures from 4.30 to 4.33, are obtained by using both SIMPLE and SIMPLER algorithms on three different grid sizes by using hybrid and power law differencing schemes. The results by using hybrid and power law differencing schemes are nearly identical to each other when the same grid size is used on either SIMPLE or SIMPLER algorithm. However for all calculations, the hybrid scheme gives slightly better results.

Results of velocity profiles with the SIMPLE algorithm on a 161x161 uniform grid deviates from Ghia's [8] results. As the grid size is increased to 257x257, the accuracy of the SIMPLE method becomes more acceptable but they are still significantly different from Ghia's [8] results. Also, results on a 299x299 uniform grid are slightly better than the results on a 257x257 mesh.

The change between the results for 299x299 and 257x257 uniform meshes is not so significant. The solution with SIMPLE algorithm becomes grid independent when the grid size is nearly 300x300.

Unlike the SIMPLE algorithm, the results of the velocity profiles with the SIMPLER algorithm on a 161x161 uniform grid using both power law and hybrid schemes are close to the results on 257x257 and 291x291 uniform meshes. The closest result to Ghia's [8] solution is obtained by the SIMPLER algorithm by using hybrid scheme when the grid size is 257x257.

When the SIMPLE and SIMPLER algorithms on a uniform grid size of 257x257 are compared, it is obvious that the SIMPLER method is more close to the Ghia [8] results as observed from Figures 3.34 and 3.35. In addition to this, the results of SIMPLE algorithm are significantly different from Ghia's [8] solution.

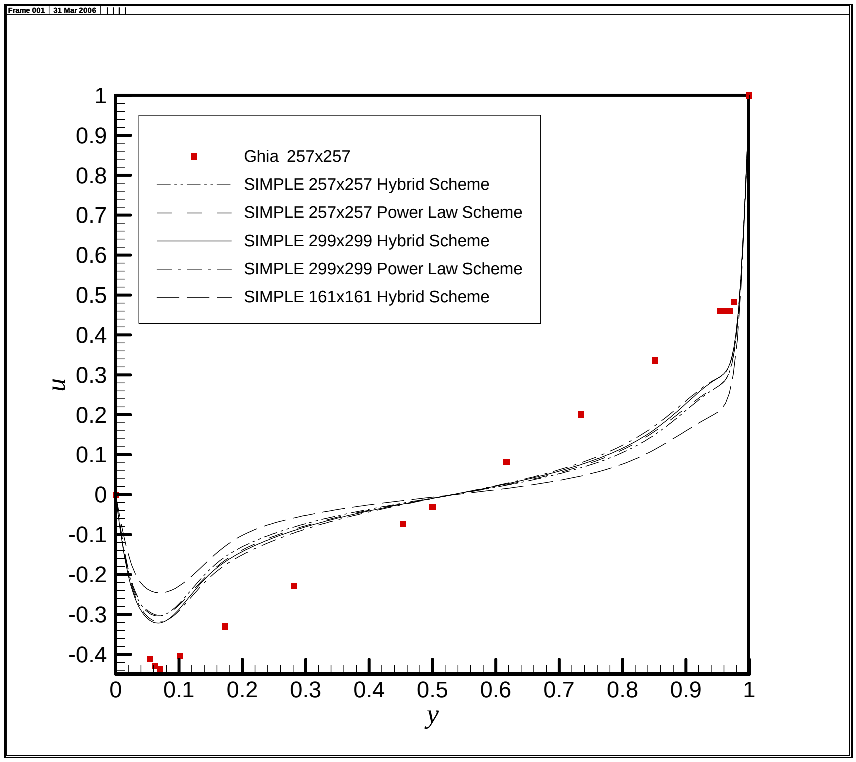

Figure 4.30 Vertical centerline *u*-velocity profiles for *Re*=5000 using the SIMPLE algorithm

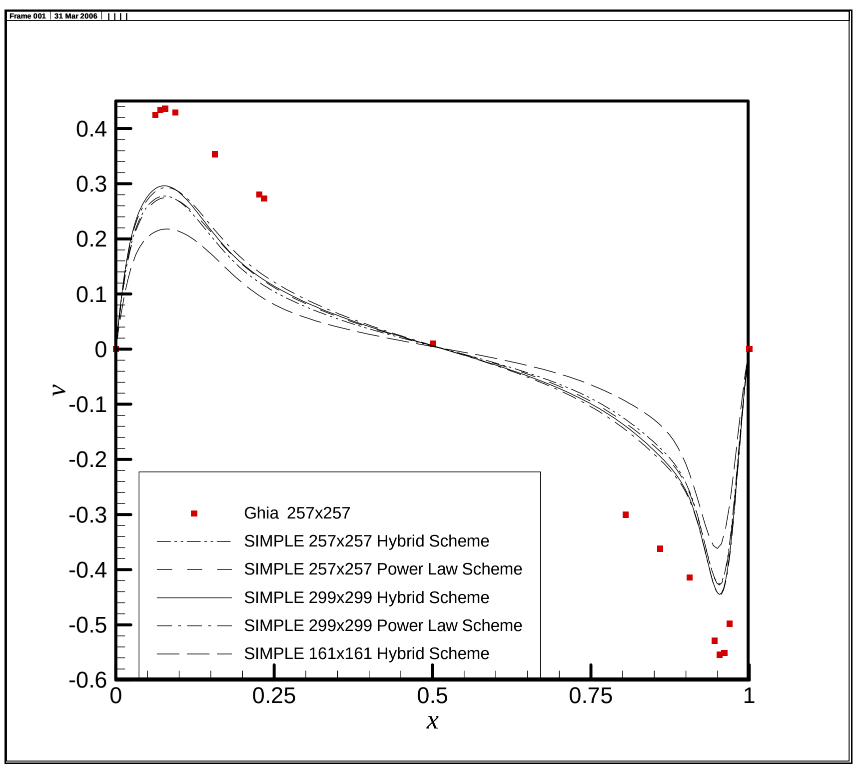

Figure 4.31 Horizontal centerline *v*-velocity profiles for *Re*=5000 using the SIMPLE algorithm

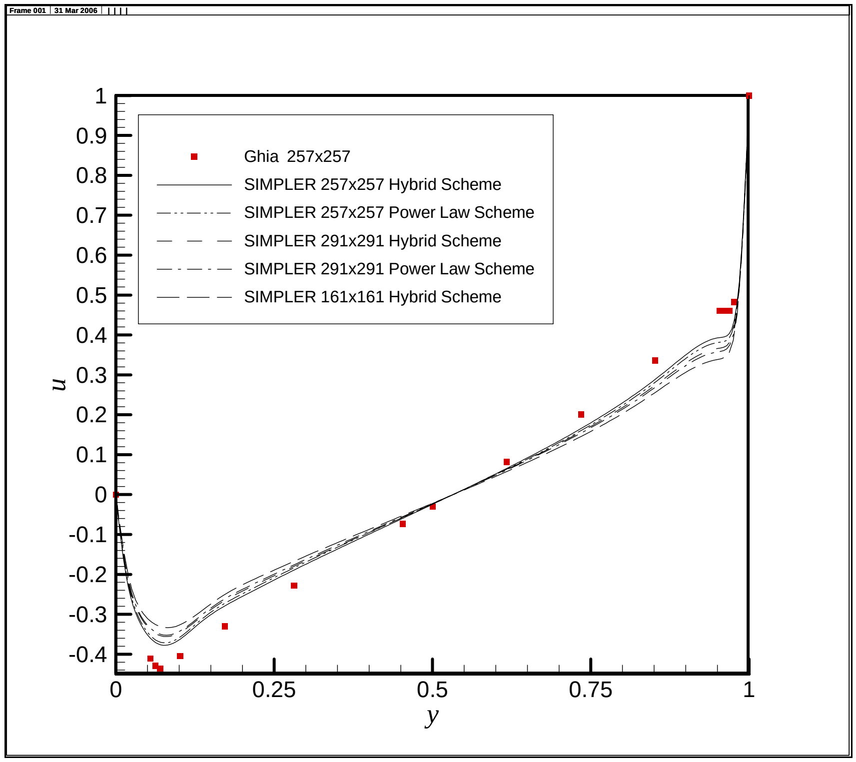

Figure 4.32 Vertical centerline *u*-velocity profiles for *Re*=5000 by using the SIMPLER algorithm

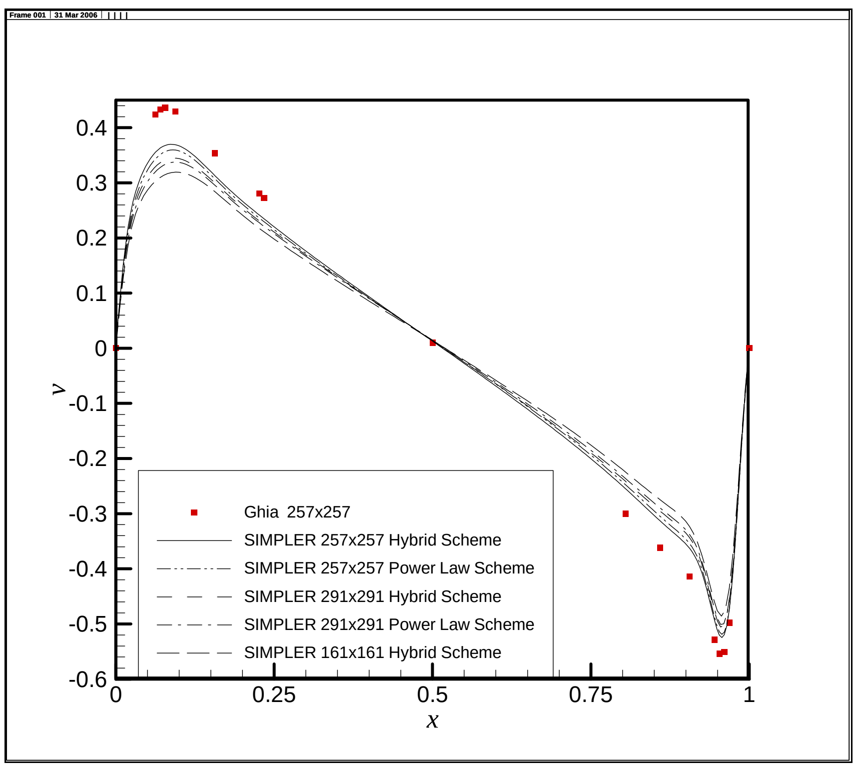

Figure 4.33 Horizontal centerline *v*-velocity profiles for *Re*=5000 by using the SIMPLER algorithm

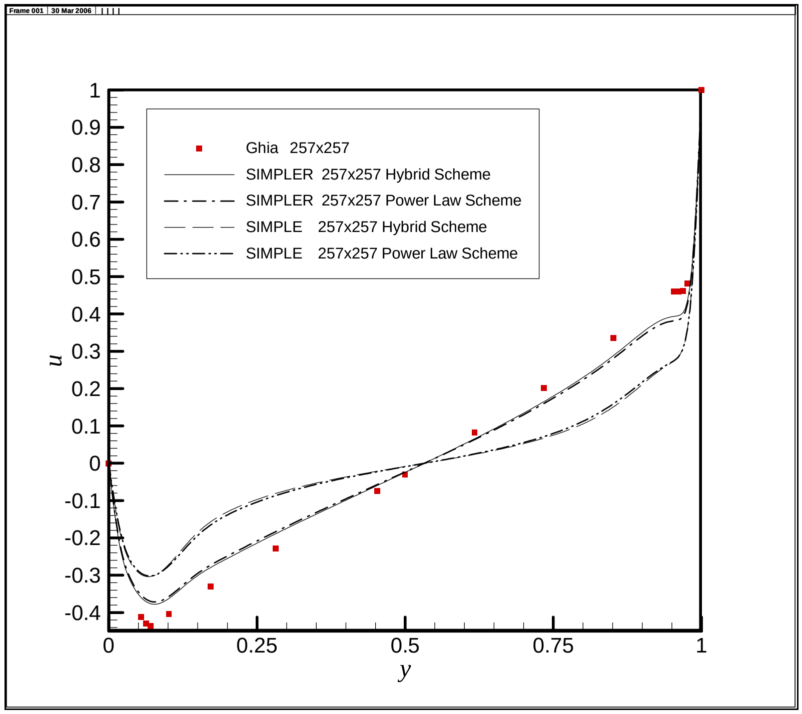

Figure 4.34 Vertical centerline *u*-velocity profiles for *Re*=5000 both by using the SIMPLE and SIMPLER algorithms on a 257x257 grid size

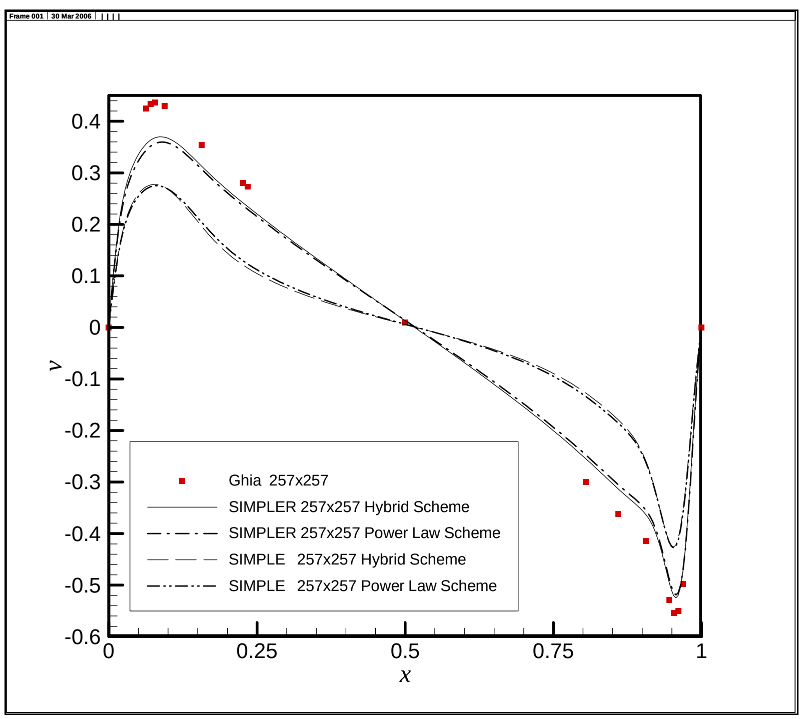

Figure 4.35 Horizontal centerline *v*-velocity profiles for *Re*=5000 both by using the SIMPLE and SIMPLER algorithms on a 257x257 grid size

Table 4.11 Extrema of velocity profiles along centerlines

for the lid-driven square cavity at *Re*=5000

***Re*=5000**	**Grid Size**	**Extrema of velocity profiles along the certerlines**					
		u_{min}	y_{min}	v_{max}	x_{max}	v_{min}	x_{min}
Ghia, Ghia and Shin [8]	257x257	-0,4364	0,0703	0,4365	0,0781	-0,5541	0,9531
Bruneau and Jouron [20]	-	-0,4359	0,0664	0,4259	0,0762	-0,5675	0,9590
Soh [10]	161x161	-0,4150	0,0810	-	-	-	-
SIMPLE Power Law	**257x257**	**-0,3020**	**0,0706**	**0,2750**	**0,0824**	**-0,4277**	**0,9529**
SIMPLE Power Law	**299x299**	**-0,3190**	**0,0707**	**0,2931**	**0,0808**	**-0,4460**	**0,9529**
SIMPLE Hybrid	**257x257**	**-0,3217**	**0,0667**	**0,2772**	**0,0824**	**-0,4262**	**0,9529**
SIMPLE Hybrid	**299x299**	**-0,3020**	**0,0673**	**0,2964**	**0,0774**	**-0,4448**	**0,9529**
SIMPLER Power Law	**201x201**	**-0,3521**	**0,0804**	**0,3370**	**0,0955**	**-0,5004**	**0,9548**
SIMPLER Power Law	**257x257**	**-0,3717**	**0,0784**	**0,3597**	**0,0902**	**-0,5190**	**0,9569**
SIMPLER Power Law	**291x291**	**-0,3524**	**0,0804**	**0,3376**	**0,0955**	**-0,5008**	**0,9548**
SIMPLER Hybrid	**201x201**	**-0,3555**	**0,0804**	**0,3440**	**0,0905**	**-0,5048**	**0,9548**
SIMPLER Hybrid	**257x257**	**-0,3778**	**0,0784**	**0,3697**	**0,0902**	**-0,5247**	**0,9569**
SIMPLER Hybrid	**291x291**	**-0,3560**	**0,0804**	**0,3449**	**0,0905**	**-0,5054**	**0,9548**

A good convergence to the steady laminar solution with the SIMPLE method is observed for *Re*=100 and 400 on a uniform 161x161 grid and for *Re*=1000 on a 257x257 uniform grid. However, when the Reynolds number is increased to 5000, the solutions with the SIMPLE algorithm are in a rather poor agreement with Ghia's [8] result. Not only the difference between the SIMPLE and SIMPLER algorithms is shown in Figures 4.30, 4.31, 4.34 and 4.35, but also the difference at the extrema points of the velocity profiles passing through the geometric center of the square cavity is shown in Table 4.11. It is clear that local maxima and minima values of the velocity profiles with the SIMPLE method deviate from Ghia's [8] results.

When solutions of the SIMPLER algorithm for *Re*=100 on a uniform 129x129 grid, for *Re*=400 and 1000 on a uniform 161x161 grid, and for *Re*=5000 on a uniform 257x257 grid is examined, it can be mentioned that these steady laminar converged results exhibit perfect match with Ghia's [8] results. Although the grid size of 257x257 is very fine for a Reynolds number of 5000, a stable converged solution is obtained by SIMPLER method.

The location of the centers of the primary and secondary bottom right and left vortices are presented in Table 4.12. These results are obtained with the SIMPLE and SIMPLER algorithms using hybrid and power law schemes on different grid sizes. The data available in the literature is also presented in this table. The solutions with SIMPLER algorithm exhibit a good match with the results in the literature, whereas the results of SIMPLE algorithm are not close to the results in the literature.

Up to a Reynolds number of 5000, only primary, secondary bottom right and secondary bottom left vortices are observed. However, at a Reynolds number of 5000, tertiary vortex at bottom right and secondary vortex at top left are firstly visible. The locations of centers of these vortices, which are indicated in Table 4.12(b), are identical to the results in the literature. When Tables 4.12a and Table 4.12b are compared, the location centers of the primary, secondary bottom right and secondary bottom left vortices are quite good agreement with the results in the literature than the location of centers of the secondary top left and tertiary bottom right and left vortices.

Although a tertiary vortex at bottom left is obtained by Ghia [8], Bruneau and Jouron [20], Gupta and Kalita [4] and Barragy and Carey [31], this vortex can not be observed by SIMPLE and SIMPLER algortihms in our calculation, and by Hou et. All [30].

Table 4.12 Center locations of the vortices for the lid-driven square cavity at Re=5000

(a) Primary, Secondary bottom right and left vortices

***Re*=5000**	Grid Size	Primary vortex Location (x,y)	Secondary vortex Bottom right Location (x,y)	Secondary vortex Bottom left Location (x,y)
Ghia, Ghia and Shin [8]	257x257	(0.5117,0.5352)	(0.8086,0.0742)	(0.0703,0.1367)
Schreiber and Keller [7] *	161x161	(0.5188,0.5375)	(0.8188,0.0750)	(0.0857,0.0714)
Bruneau and Jouron [20]	256x256	(0.5156,0.5313)	(0.8301,0.0703)	(0.0664,0.1484)
Vanka [28]	64x64	(0.5125,0.5313)	(0.8500,0.0813)	(0.0625,0.1563)
Gupta and Kalita [4]	161x161	(0.5125,0.5375)	(0.8000,0.0750)	(0.0750,0.1313)
Hou et. All [30]	-	(0.5176,0.5373)	(0.8078,0.0745)	(0.0784,0.1313)
Barragy and Carey [31]	-	(0.5113,0.5283)	(0.8041,0.0725)	(0.0725,0.1370)
SIMPLE Power Law	**257x257**	**(0.5227,0.5352)**	**(0.8416,0.0740)**	**(0.0768,0.1358)**
SIMPLE Power Law	**299x299**	**(0.5217,0.5338)**	**(0.8387,0.0736)**	**(0.0743,0.1359)**
SIMPLE Hybrid	**257x257**	**(0.5218,0.5348)**	**(0.8322,0.0730)**	**(0.0779,0.1334)**
SIMPLE Hybrid	**299x299**	**(0.5207,0.5332)**	**(0.8297,0.0732)**	**(0.0773,0.1329)**
SIMPLER Power Law	**201x201**	**(0.5221,0.5340)**	**(0.8398,0.0726)**	**(0.0713,0.1471)**
SIMPLER Power Law	**257x257**	**(0.5202,0.5341)**	**(0.8261,0.0702)**	**(0.712,0.1462)**
SIMPLER Power Law	**291x291**	**(0.5221,0.5342)**	**(0.8396,0.0726)**	**(0.0714,0.1471)**
SIMPLER Hybrid	**201x201**	**(0.5207,0.5346)**	**(0.8238,0.0694)**	**(0.0696,0.1521)**
SIMPLER Hybrid	**257x257**	**(0.5191,0.5335)**	**(0.8105,0.0653)**	**(0.0690,0.1521)**
SIMPLER Hybrid	**291x291**	**(0.5206,0.5346)**	**(0.8236,0.0694)**	**(0.0696,0.1521)**

* The results are obtained at Re=4000

Table 4.12 Center locations of the vortices for the lid-driven square cavity at *Re*=5000

(b) Secondary top left, Tertiary bottom right and left vortices

Re=5000	Grid Size	Secondary vortex Top Left Location (x,y)	Tertiary vortex Bottom right Location (x,y)	Tertiary vortex Bottom left Location (x,y)
Ghia, Ghia and Shin [8]	257x257	(0.0625,0.9102)	(0.9805,0.0195)	(0.0117,0.0078)
Bruneau and Jouron [20]	256x256	(0.0625,0.9102)	(0.9668,0.0293)	(0.0117,0.0098)
Gupta and Kalita [4]	161x161	(0.0688,0.9125)	(0.9750,0.0188)	(0.0063,0.0063)
Hou et. All [30]	-	(0.0667,0.9059)	-	-
Barragy and Carey [31]	-	(0.0635,0.9092)	(0.9786,0.0188)	(0.0079,0.0079)
SIMPLE Power Law	**257x257**	**(0.0437,0.9000)**	**(0.9834,0.0136)**	**-**
SIMPLE Power Law	**299x299**	**(0.0463,0.9029)**	**(0.9805,0.0120)**	**-**
SIMPLE Hybrid	**257x257**	**(0.0438,0.9004)**	**(0.9846,0.0137)**	**-**
SIMPLE Hybrid	**299x299**	**(0.0473,0.9034)**	**(0.9835,0.0123)**	**-**
SIMPLER Power Law	**201x201**	**(0.0565,0.9087)**	**(0.9723,0.0238)**	**-**
SIMPLER Power Law	**257x257**	**(0.0592,0.9122)**	**(0.9657,0.0289)**	**-**
SIMPLER Power Law	**291x291**	**(0.0567,0.9087)**	**(0.9723,0.0239)**	**-**
SIMPLER Hybrid	**201x201**	**(0.0578,0.9106)**	**(0.9636,0.0333)**	**-**
SIMPLER Hybrid	**257x257**	**(0.0601,0.9125)**	**(0.9636,0.0333)**	**-**
SIMPLER Hybrid	**291x291**	**(0.0579,0.9106)**	**(0.9623,0.0327)**	**-**

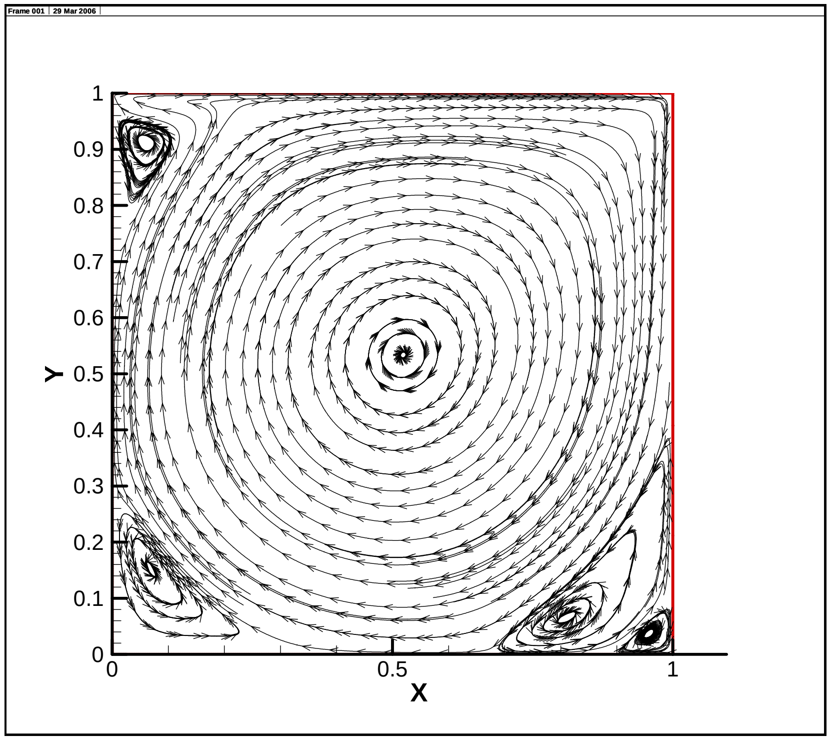

Figure 4.36 The streamlines for Re=5000 on a 257x257 mesh by using the SIMPLER algorithm with the hybrid differencing scheme

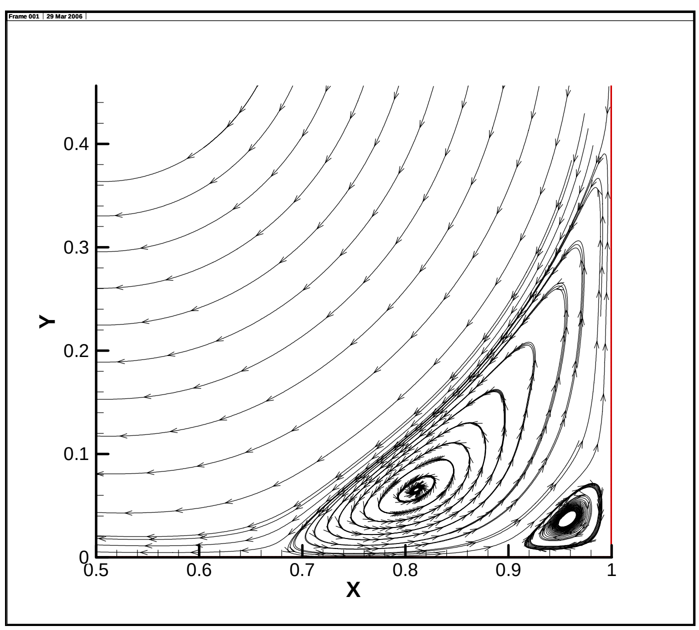

Figure 4.37 The streamlines for Re=5000 on a 257x257 mesh by using the SIMPLER algorithm with the hybrid differencing scheme

(a) at bottom right corner

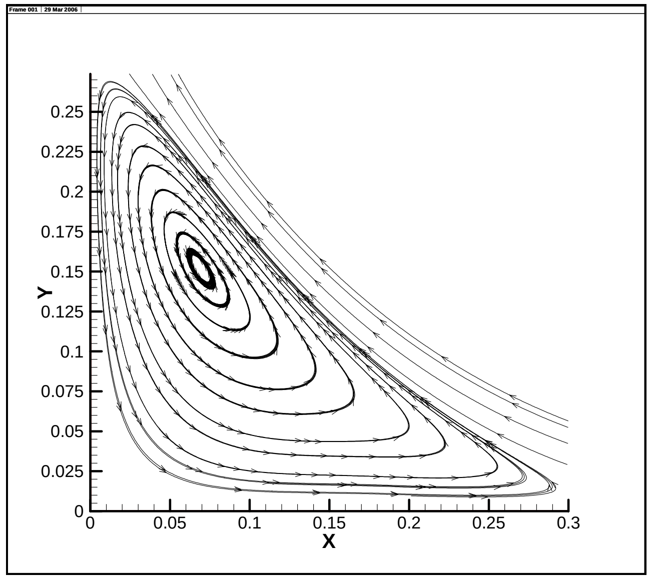

Figure 4.37 The streamlines for *Re*=5000 on 257x257 mesh by using the SIMPLER algorithm with the hybrid differencing scheme

(b) at bottom left corner

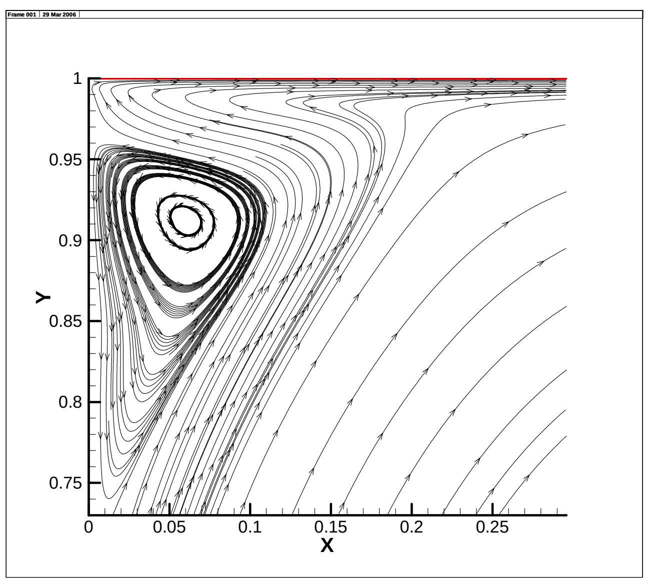

Figure 4.37 The streamlines for *Re*=5000 on 257x257 mesh by using the SIMPLER algorithm with the hybrid differencing scheme

(c) at top left corner

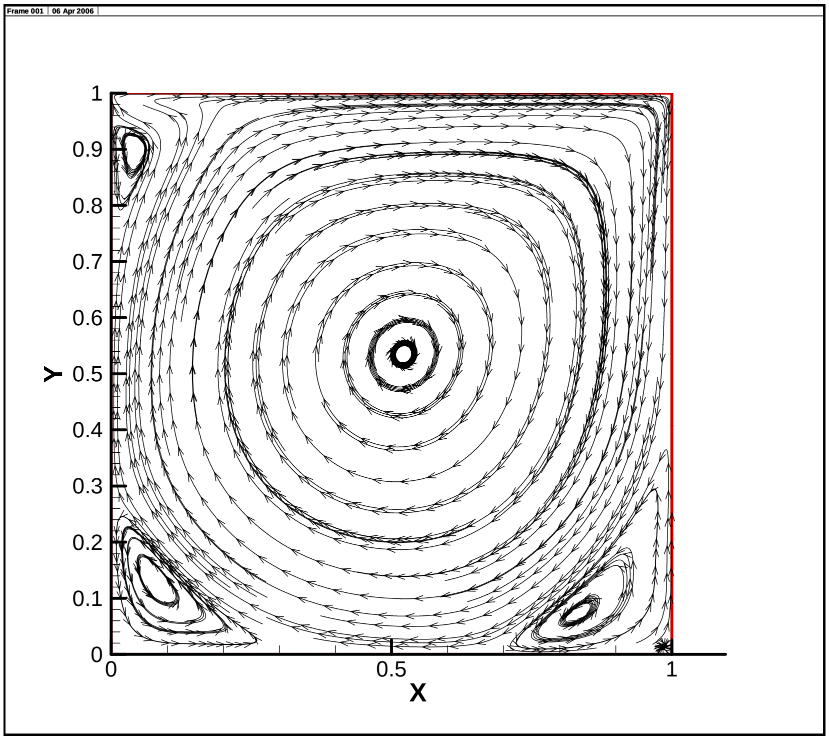

Figure 4.38 The streamlines for *Re*=5000 on a 257x257 mesh by using the SIMPLE algorithm with the hybrid differencing scheme

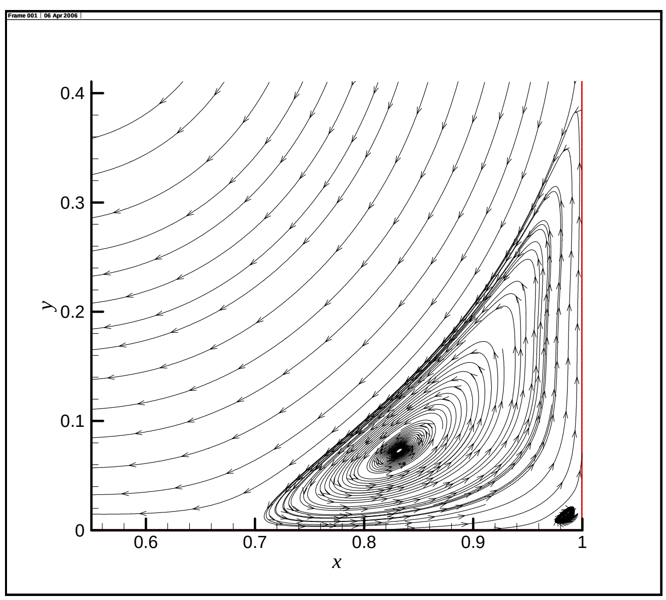

Figure 4.39 The streamlines for *Re*=5000 on 257x257 mesh by using the SIMPLE algorithm with the hybrid differencing scheme

(a) at bottom right corner

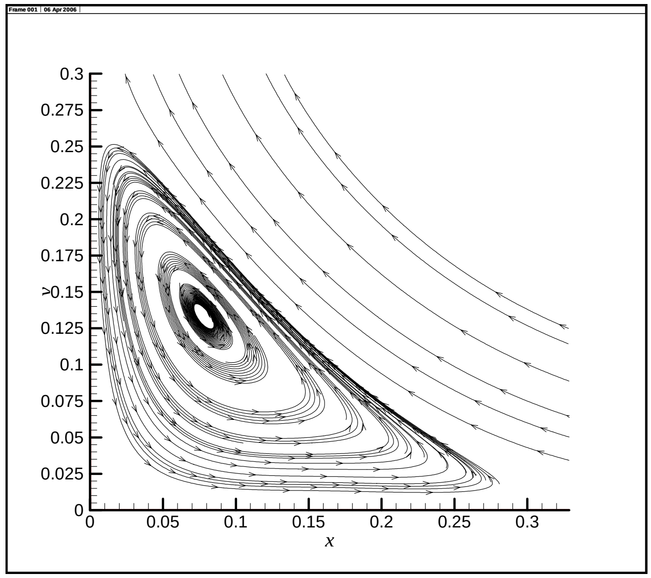

Figure 4.39 The streamlines for *Re*=5000 on 257x257 mesh by using the SIMPLE algorithm with the hybrid differencing scheme

(b) at bottom left corner

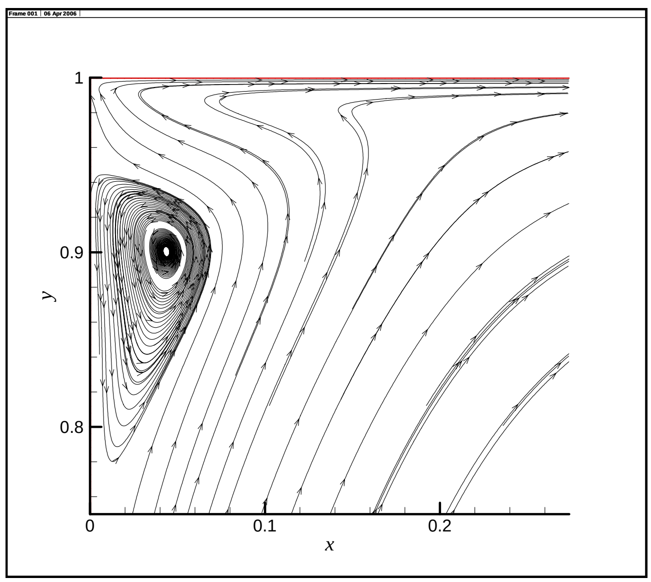

Figure 4.39 The streamlines for *Re*=5000 on 257x257 mesh by using the SIMPLE algorithm with the hybrid differencing scheme

(c) at top left corner

The solution with the SIMPLER algorithm using the hybrid scheme on a uniform 257x257 grid size is the most closest solution to the results available in the literature for *Re*=5000. The streamlines of this solution is illustrated in Figure 4.36 and the vortex at top left, vortex at bottom left and two vortices at bottom right are shown in Figures 4.37a, 4.37b and 4.37c, respectively. Figures 4.38, 4.39a, 4.39b and 4.39c shows the streamline plots obtained by the SIMPLE method using the hybrid scheme on a uniform 257x257 grid size. When the results for SIMPLE and SIMPLER algorithms by using same scheme on same gird size are compared in Figures 4.36 and 4.38, it can be observed that the strength of vortices calculated by the SIMPLER algorithm is higher and the space occupied by secondary and tertiary vortices are larger. Also tertiary bottom right vortex with the SIMPLER algorithm is quite visible. However, the same vortex obtained by the SIMPLE algorithm is just brought into view.

In addition to these, the calculations are carried on different clustered meshes both with SIMPLE and SIMPLER algorithm by using power law and hybrid schemes. These results, are compared with the results obtained by uniform meshes of the same sizes, are shown in Figures 4.40 and 4.41 according to their velocity profiles along the centerlines of the cavity. Moreover number of iterations with respect to velocity residuals, which are required to obtain converged solutions on uniform and clustered meshes by using the same methods, schemes and grid sizes, are presented and compared in Table 4.12.

Although the grid is clustered near the boundaries that leads to clustered mesh generation at bottom left corner, tertiary vortex at bottom left is also not visible.

The other vortices are visible and locations of their centers are the same as the results on uniform meshes for the methods and schemes.

In addition to this, it is clear from Table 4.12 that for the SIMPLER algorithm, to reach the same residual for a 257x257clustered mesh takes quite less iterations than for a 257x257 uniform mesh. Also, the velocity residuals, which are obtained by 257x257 clustered meshes using power law and hybrid schemes after 20000 iterations, are slightly less than the velocity residuals obtained by 257x257 uniform meshes in the case of SIMPLE method. Unlike for the Reynolds numbers of 100 and 400, replacing a uniform mesh with a clustered mesh does not make significant change in number of iterations and computational time.

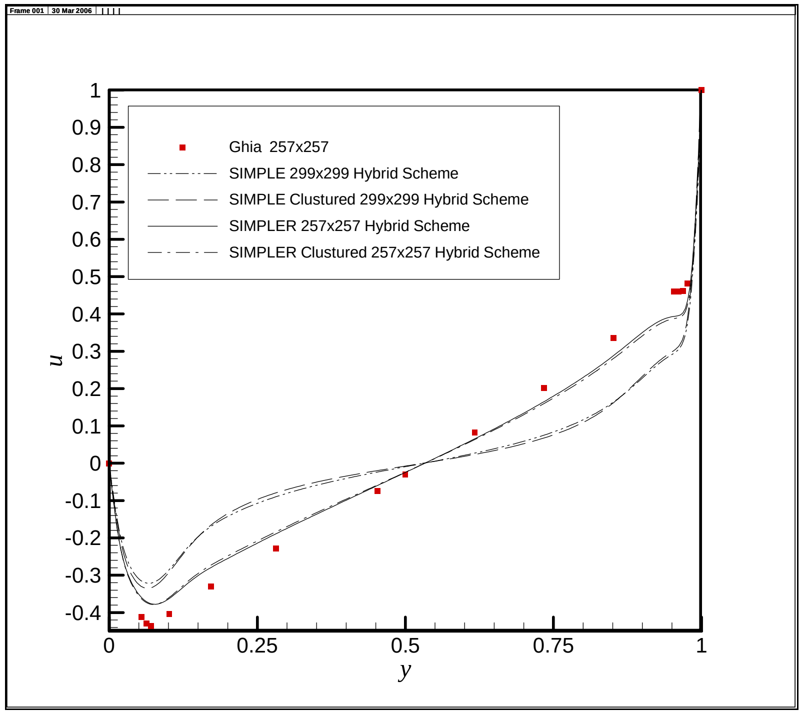

Figure 4.40 Vertical centerline *u*-velocity profiles for *Re*=5000 with the SIMPLE and SIMPLER algorithm by using clustered and uniform meshes

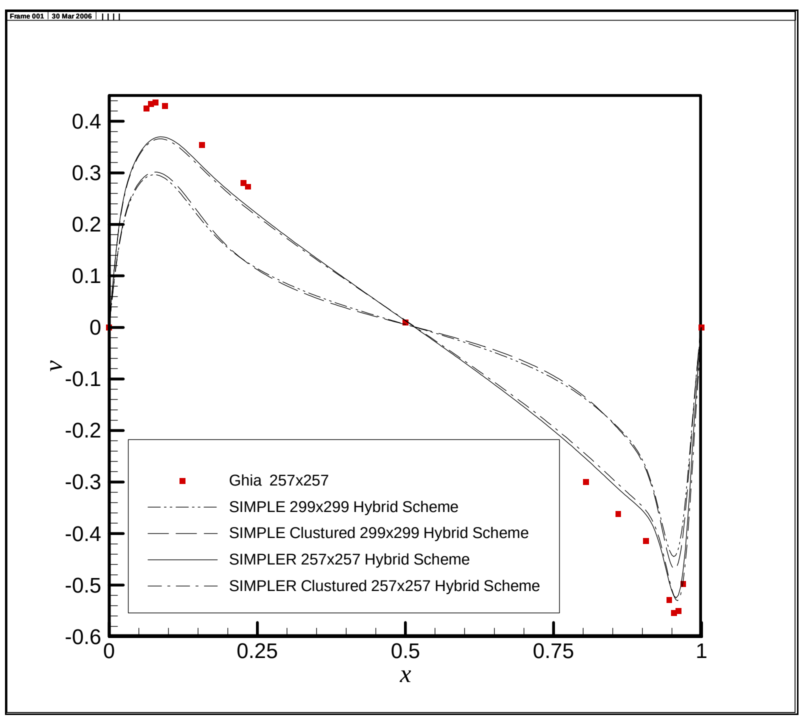

Figure 4.41 Horizontal centerline *v*-velocity profiles for *Re*=5000 with the SIMPLE and SIMPLER algorithm by using clustered and uniform meshes

Table 4.12 Number of Iterations with SIMPLER algorithm on uniform and clustered meshes using hybrid and power law schemes for *Re*=5000

***Re*=5000**	Grid Size	Number of Iterations	Error *u* and *v* less than
SIMPLER Hybrid	**257x257**	**470**	**1x10-5**
SIMPLER Hybrid Clustered	**257x257**	**438**	**1x10-5**
SIMPLER Power Law	**257x257**	**494**	**1x10-5**
SIMPLER Power Law Clustered	**257x257**	**426**	**1x10-5**
SIMPLE Hybrid	**299x299**	**20000**	**0,694x10-2**
SIMPLE Hybrid Clustered	**299x299**	**20000**	**0,665x10-2**
SIMPLE Power Law	**299x299**	**20000**	**0,643x10-2**
SIMPLE Power Law Clustered	**299x299**	**20000**	**0,623x10-2**

4.2.3.6 Results for *Re*=10000

When the Reynolds number is increased to 10000, the flow inside a lid-driven square cavity becomes a more difficult test case to investigate. Since more complex flow interactions, which can be highly unsteady, are guessed. In addition to this, numerical uncertainties and inconsistencies start to take place on which many researchers have been agreed. It is explained by Huser [18] that the Reynolds number is directly proportional to the driving shear force in the lid-driven cavity influencing the dynamics of recirculating flows. As the Reynolds number increases, high gradients in the shear stress distribution near the solid boundaries increase the effects of viscosity which lead to increase the local curvature of the mean velocity profile [18]. Small eddies are developed at the two lower corners and also at the upper left corner. This development makes the laminar mean velocity of the primary vortex unstable and interaction of these eddying motions with the mean shear causes turbulence [3]. Reynolds number 10000 is limiting Reynolds number at which turbulence starts. The translation to turbulence is the result of the development of these small eddies. However, in early researches, Bye [32] found out that the transition Reynolds number is between 400 and 600. Also Kumagai [33] estimates the transition at lower Reynolds number than Bye's [32].

Ghia [8] obtained a converged steady-state solution at a Reynolds number of 10000 by using the QUICK scheme on a 82x82 grid. Most recent study by Huser [18] is also able to get steady-state results for *Re*=10000. Hayase [15] mentioned that the flow inside the lid-driven cavity also converges to a steady-state solution at *Re*=10000. Although Wirogo's [3] result with a 322x322 multigrid solution using the power law scheme is not good agreement with Ghia's [8] fine grid solution, steady-state converged solution with Flux Corrected method using QUICK scheme is obtained on 82x82 grid at *Re*=10000.

The centerline velocity profiles with SIMPLE and SIMPLER algorithm on fine grids are shown in Figures 4.42 and 4.43. Although hybrid scheme is used in all calculations presented in these figures, power law scheme results are identical to the results which are obtained by using hybrid scheme. It is clear that the both power law and hybrid scheme solutions are so far from the Ghia's [8] solutions, since both schemes are too diffusive to calculate high convection recirculating flow properly at high Reynolds number 10000. Therefore stability of the numerical scheme becomes more important at these high Reynolds numbers.

Solution of SIMPLER method on a uniform 257x257 grid and solutions of SIMPLE method both with uniform and clustered 299x299 meshes are incorrect when they are compared with the Ghia's [8] results but converged solutions. Since the formation of corner vortices causes transition, the flow becomes highly unsteady and it can not be properly evaluated by using steady-state numerical calculations.

Ghia's [8] results at *Re*=5000 and 1000 are given in Figures 4.42 and 4.43. Both results are close to each other that the change in centerline velocity profiles is not so significant above a Reynolds number of 5000.

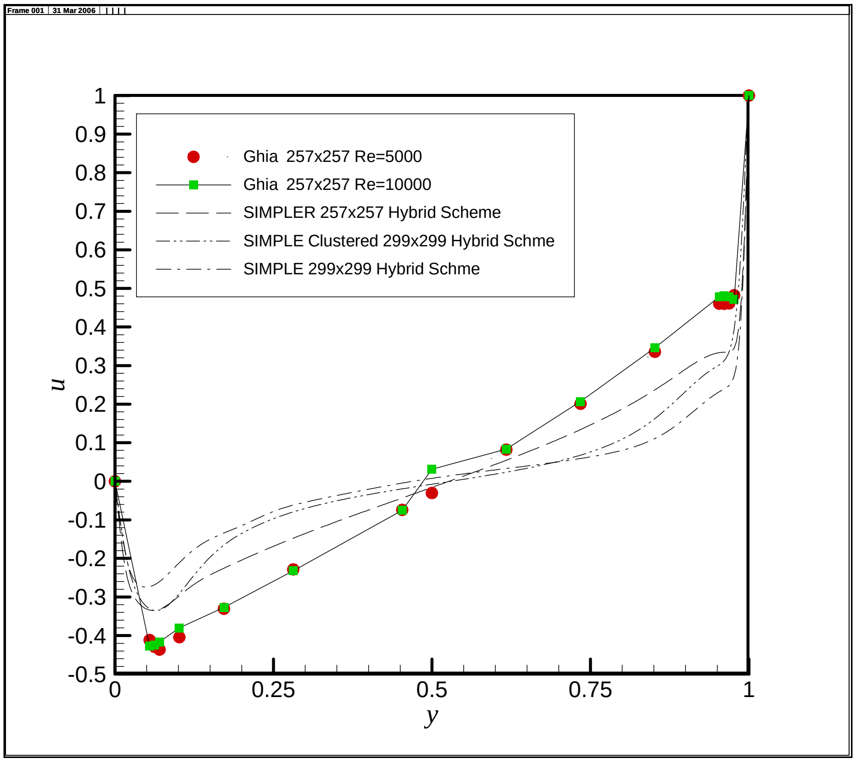

Figure 4.42 Vertical centerline *u*-velocity profiles for *Re*=10000

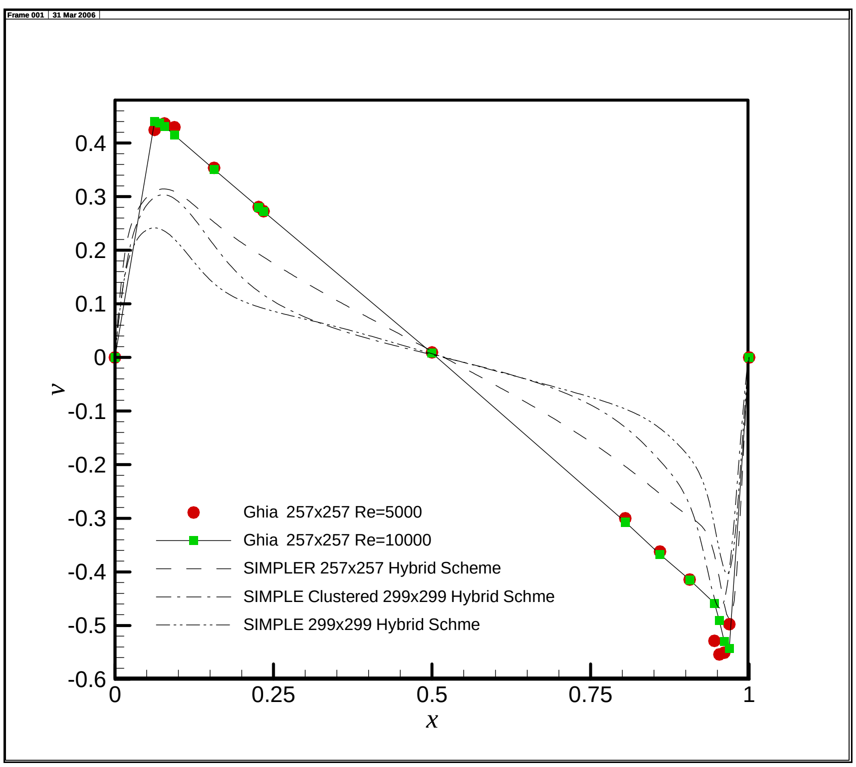

Figure 4.43 Horizontal centerline *v*-velocity profiles for *Re*=10000

Although with respect to centerline velocity profiles converged results of SIMPLER method are far from the results in the literature, results are closer when the centerline locations of the vortices are considered. The center locations of primary and secondary bottom right and left vortices are shown in Table 4.14a. While center locations of secondary vortices at top left and tertiary vortices at bottom right and left are presented in Table 4.14b.

While the tertiary vortex at bottom left is not visible at Re=5000, it can be obtained when the Reynolds number increased to 10000. In addition to this, tertiary vortex at bottom left becomes quite visible.

The streamlines obtained by SIMPLER method using hybrid scheme on a 257x257 uniform gird are presented in Figure 4.44. The top left, bottom right and left corners are illustrated in Figure 4.45a, 4.45b and 4.45c to visualize how much space is dominated by secondary and tertiary vortices at these corners more precisely. Since it is mentioned previously that the results of power law and hybrid scheme are nearly identical, obtained streamlines and the strength of the vortices with both schemes are close to each other.

Table 4.14 Center locations of the vortices
for the lid-driven square cavity at *Re*=10000
(a) Primary, Secondary bottom right and left vortices

***Re*=10000**	Grid Size	Primary vortex Location (x,y)	Secondary vortex Bottom right Location (x,y)	Secondary vortex Bottom left Location (x,y)
Ghia, Ghia and Shin [8]	257x257	(0.5117,0.5333)	(0.7656,0.0586)	(0.0586,0.1641)
Schreiber and Keller [7]	180x180	(0.5140,0.5307)	(0.7656,0.0615)	-
Bruneau and Jouron [20]	256x256	(0.5156,0.5234)	(0.8945,0.0820)	(0.0781,0.1133)
Gupta and Kalita [4]	161x161	(0.5125,0.5313)	(0.7813,0.0625)	(0.0623,0.1564)
Barragy and Carey [31]	-	(0.5113,0.5302)	(0.7747,0.0588)	(0.0588,0.1623)
SIMPLER Hybrid	**257x257**	**(0.5194,0.5297)**	**(0.8360,0.0738)**	**(0.0561,0.1771)**
SIMPLER Power Law	**257x257**	**(0.5207,0.5286)**	**(0.8680,0.0788)**	**(0.0622,0.1625)**

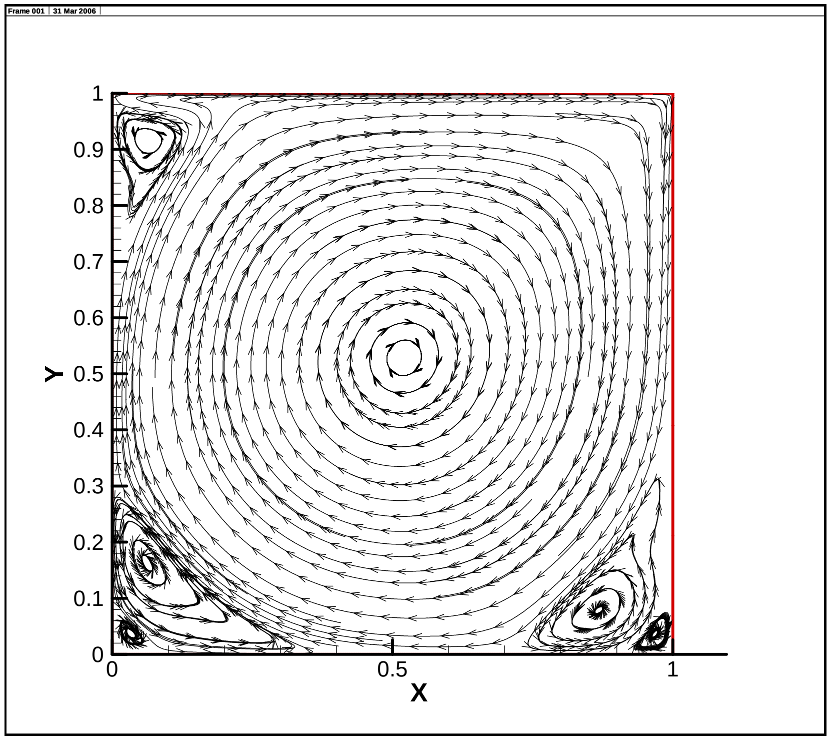

Figure 4.44 The streamlines for *Re*=10000 on a 257x257 mesh by using the SIMPLER algorithm with the hybrid differencing scheme

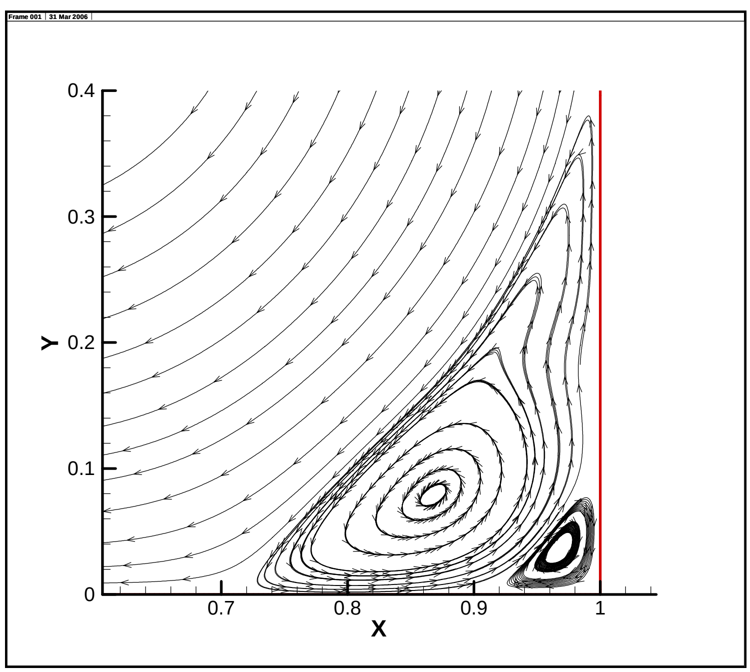

Figure 4.45 The streamlines for *Re*=10000 on a 257x257 mesh by using the SIMPLER algorithm with the hybrid differencing scheme

(a) at bottom right corner

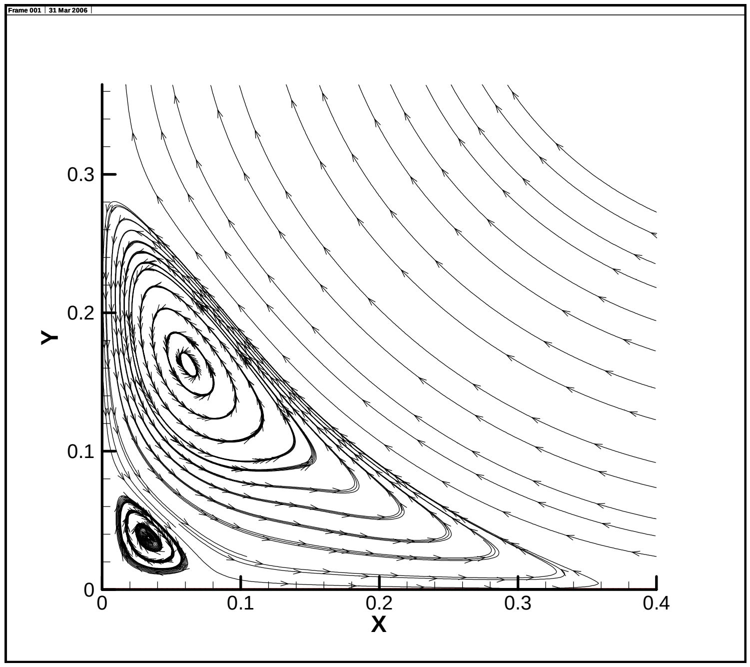

Figure 4.45 The streamlines for *Re*=10000 on a 257x257 mesh by using SIMPLER algorithm with the hybrid differencing scheme

(b) at bottom left corner

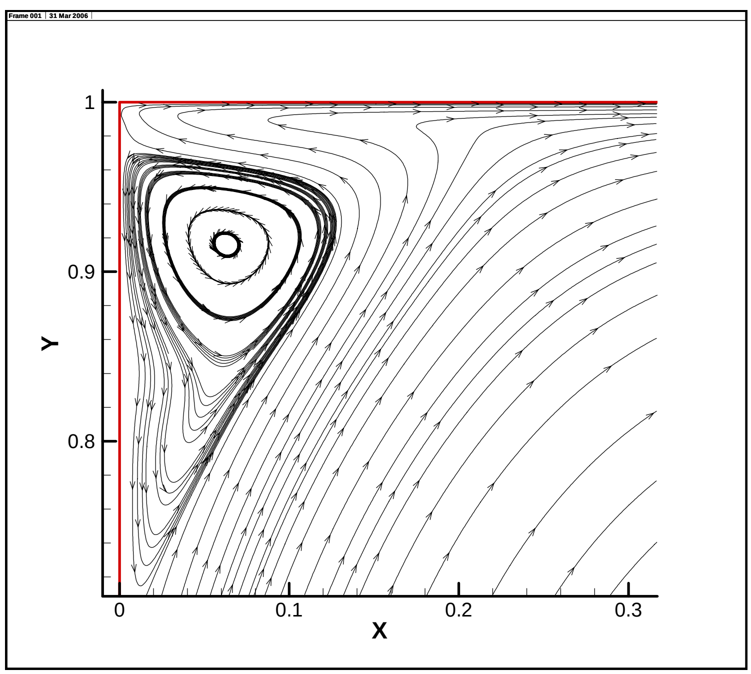

Figure 4.45 The streamlines for *Re*=10000 on a 257x257 mesh SIMPLER algorithm with the hybrid differencing scheme

(c) at top left corner

Table 4.14 Center locations of the vortices for the lid-driven square cavity at Re=10000

(b) Secondary top left, Tertiary bottom right and left vortices

Re=10000	Grid Size	Secondary vortex Top Left Location (x,y)	Tertiary vortex Bottom right Location (x,y)	Tertiary vortex Bottom left Location (x,y)
Ghia, Ghia and Shin [8]	257x257	(0.0703,0.9141)	(0.9336,0.0625)	(0.0156,0.0195)
Bruneau and Jouron [20]	256x256	(0.0664,0.9141)	-	-
Gupta and Kalita [4]	161x161	(0.0688,0.9188)	(0.9563,0.0375)	(0.0125,0.0187)
Barragy and Carey [31]	-	(0.0702,0.9108)	(0.9351,0.0675)	(0.0173,0.0201)
SIMPLER Hybrid	**257x257**	**(0.0632,0.9174)**	**(0.9491,0.0753)**	**(0.0392,0.0447)**
SIMPLER Power Law	**257x257**	**(0.0628,0.9161)**	**(0.9679,0.0365)**	**(0.0334,0.0374)**

4.3 Flows over a Backward-Facing Step

The flow over a two-dimensional backward-facing step is second classical well studied test case problem for evaluating the numerical methods for the simulation of viscous incompressible recirculating flows.

4.3.1 Definition of the Problem Characteristics

A fully developed flow through the channel having a sudden expansion leads the laminar separation. The channel is long enough in order to have a fully developed outflow. The sudden expansion results in one or more regions of recirculations depending on the Reynolds number of the inflow. Figure 4.46 shows the geometry of the flow over a backward-facing step.

The expansion ratio is defined by:

$$\eta = \frac{H}{H-h} \tag{4.5}$$

where h is the step height, H is the channel height and x_L is length of the channel.

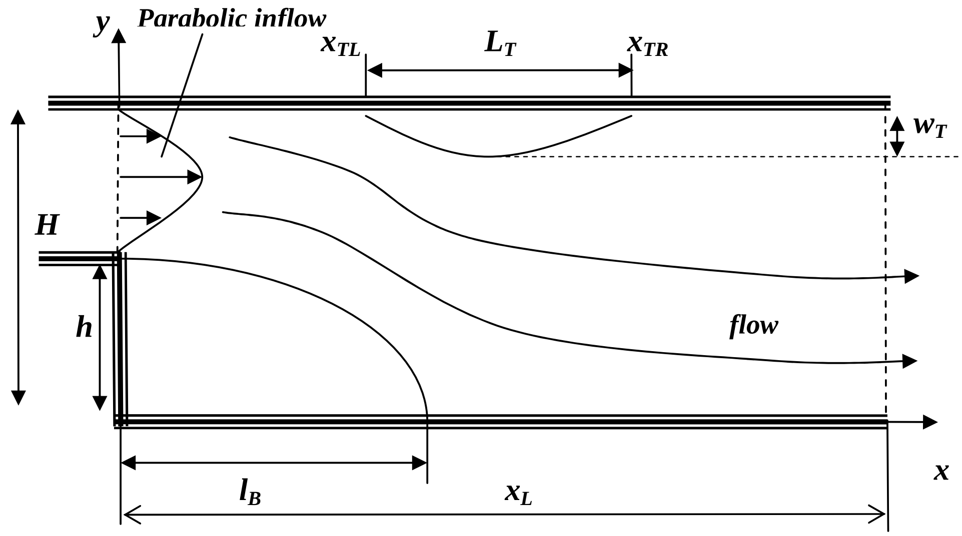

Figure 4.46 Geometry of the flow over a backward-facing step in a channel

The possible recirculating regions are shown in Figure 4.48 whose sizes and locations are indicated by the variable *x*'s.

The Reynolds number is this test case is evaluated by:

$$Re = \frac{U_{avg} H}{\nu} \tag{4.6}$$

where U_{avg} is the average inlet velocity.

At the inlet boundary, a parabolic *u*-velocity profile is prescribed and *v*-velocity is taken as is zero.

$$u = \frac{6U_{avg}(H-y)(y-H)}{(H-h)^2} \qquad x = 0, h \le y \le H \tag{4.7}$$

The wall boundary conditions are treated as the lid-driven cavity problem by imposing no-slip boundary conditions on the walls of the channel. If the grid points are not present on the boundaries, the velocities on the boundaries are calculated by simple interpolation and the boundary conditions for velocity become:

$$u(nx, j) = u(nx-1, j) \quad u(i,1) + u(i,2) = 0$$

$$u(i, ny) + u(i, ny-1) = 0 \tag{4.8}$$

$$v(1,j)+v(2,j)=0 \qquad v(i,1)=v(i,ny)=0$$
$$v(nx,j)+v(nx-1,j)=0 \tag{4.9}$$

The length x_L of the channel is taken large enough to make fully developed outflow such as $x_L \geq 30h$ and U_{avg} can be taken as $U_{avg} = \frac{2}{3}U_{\max}$.

4.3.2 Historical Background of the Backward-Facing Step

Over the last two or three decades; many researchers have proposed and developed investigations on the backward-facing step geometry. Armaly et al. [23] reported experimental and theoretical investigations of backward-facing step flow. Figure 4.47 shows the results obtained by laser-doppler measurements of the velocity distribution. Armaly et al. [23] summarized the locations of the three recirculation regions for Reynolds numbers in the range of 70≤*Re*≤8000, covering the laminar, transitional and turbulent flows.

Armaly [23] reported that the flow is laminar when *Re*<1200, transitional when 1200<*Re*<6600 and turbulent when *Re*>6600 and separated flow regions also exist approximately at Reynolds numbers higher than 400. The beginning of the recirculation region at the upper wall is upstream from the reattachment point of the primary recirculating flow region and its end is downstream from it [23]. In the study of Armaly [23] the computational and analytical approaches are identical to each other up to about *Re*=500 and *Re*=600 and expansion ratio is taken as 1.94. On the other hand, expansion ratio is taken as 2.0 in the most of the researches as well as in present study. Raithby, Strong and Hackman [24] reported numerical results with both cartesian and curvilinear meshes by using finite volume method. On the other hand, Gartling [25] used finite element method to investigate with mesh refinement. The SIMPLE method flow over a backward-facing step is studied by Barton [26] using five difference schemes. He compared the accuracy of the differencing schemes and tabulated the lower and upper reattachment lengths for different Reynolds numbers. In addition to this, Barton [27] studied the entrance effect of the laminar flow by changing the length of the inlet channel and expansion ratio in another paper. Barton [27] concluded that the low expansion numbers always experience a greater entrance effect after some distance upstream and downstream of sudden expansion. However, high expansion ratio has high entrance effect near the sudden expansion region. Moreover also using long inlet channel for low Reynolds numbers decrease the experimental errors significantly [27]. The accurate results are obtained with the SIMPLER algorithm and compared with SIMPLEV method which is an improved version of SIMPLE according to their convergence rates by Anjorin and Barton [16].

In this present study results are compared with the results mentioned in the above researches to show the accuracy of the method.

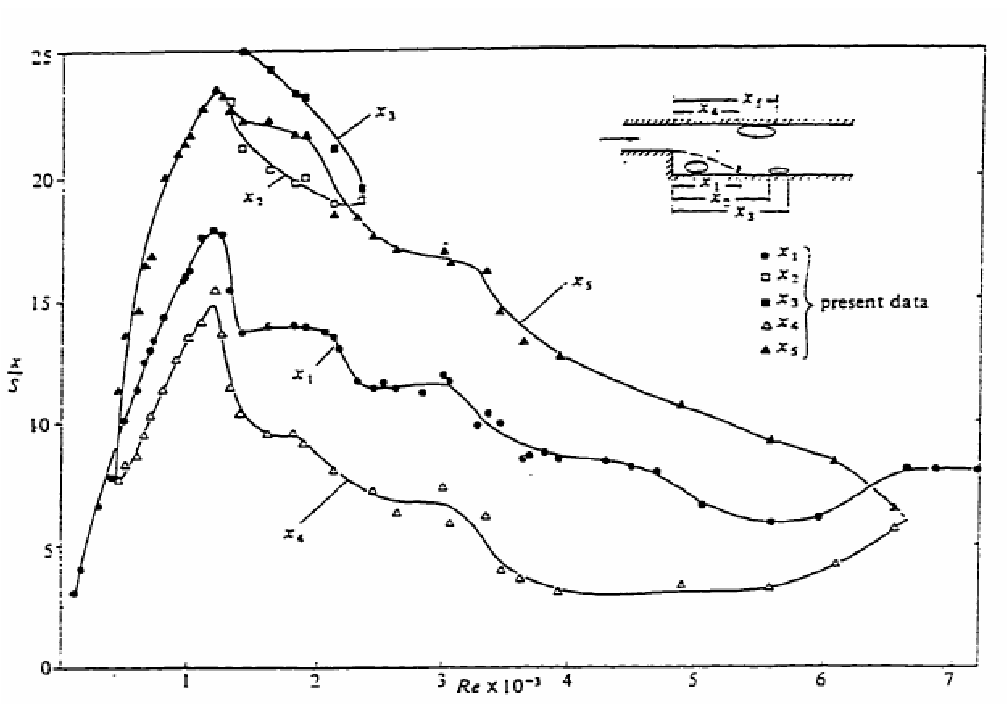

Figure 4.47 The experimental results show the locations of the detachment and reattachment of the flow at the center of the test section for different Reynolds numbers

4.3.3 Numerical Results for Flow over Backward-Facing Step

In following sections, the results obtained in this present study are compared with the results of mentioned researchers in previous section to evaluate the accuracy of the code. While making comparison of the reattachment lengths of the recirculation regions, various *x*'s, are used to illustrate these lengths as shown in the Figure 4.48.

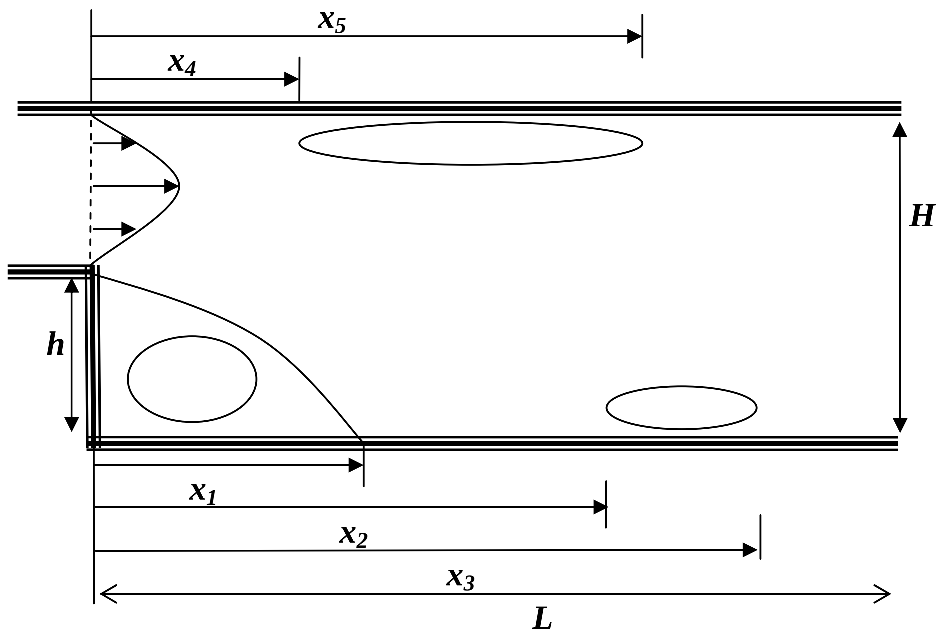

Figure 4.48 Two-Dimensional Backward-Facing Step

The accuracy and stability of the SIMPLER algorithm are investigated and compared for Reynolds numbers of 300, 400, 600 and 800. These Reynolds number are selected to restrict the flow to the laminar range until the start of turbulence.

4.3.3.1 Results for *Re*=300

First, a low Reynolds number of 300, is considered. Results with the SIMPLER algorithm and results of Barton [26] using the SIMPLE methodology are presented and compared in Table 4.15. Results of Barton [26] and present study are obtained by using different schemes on various grid sizes. It is clear from Table 4.15 that the lower reattachment length is dependent on the grid arrangement.

The hybrid scheme converges for all grid types. However, results of the hybrid scheme are not in good arrangement with higher order schemes when coarse grids are used. Very fine grids should be used to get accurate results with the hybrid scheme as well as the power law scheme. Barton [26] stated that the hybrid scheme is dominated by numerical diffusion so that in calculating larger lower reattachment length are obtained for coarser grids. However, results obtained by SIMPLER algorithm using hybrid scheme are shorter than the results of Barton [26].

Moreover, central differencing scheme diverged for coarse grids in the results of Barton [26]. However this scheme converged and gave better results when Barton [26] used finer grids, such as a 120x50 grid. Converged solution is obtained with the SIMPLER algorithm by using central differencing scheme only when the grid size is 402x62 and the length of channel is 45*h*. However, this is the worst result that is obtianed.

Results with upwind differencing scheme converge for all grid sizes. However, all reattachment lengths are under-predicted when they are compared with the results obtained by using the power law and hybrid schemes.

The reattachment length, calculated by SIMPLER method with upwind, power law and hybrid differencing schemes, are smaller than the corresponding results of Barton [26]. On the other hand, when the length of the channel increased from 45*h* to 60*h* without altering the grid sizes and scheme types, it is obvious that the lower reattachment lengths increase with increasing of the channel length. Moreover, when the number of grid points are increased from 62 to 91 in the y-directions while keeping the channel length constant, lower reattachment lengths also increase but slightly. It can be concluded that the reattachment length decreases in size with grid refinement for low Reynolds numbers.

The upper eddy is not visible for Re=300. Moreover, Figures 4.49 and 4.50 show the streamline plots for Re=300 with SIMPLER method using hybrid scheme on a 62x402 mesh when x_L=45h.

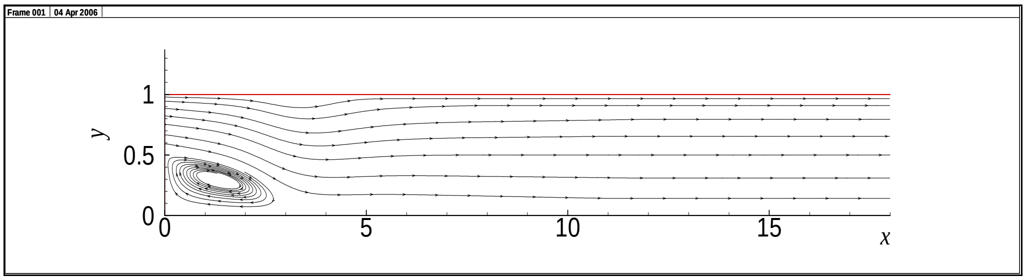

Figure 4.49 Streamlines between x=0 and x=18 for Re=300 with SIMPLER algorithm using hybrid scheme on a 402x62 mesh when x_L=45h

Table 4.15 Lower reattachment length x_l for Re=300

***Re*=300**	**Grid Size**	Upwind	Power law	Hybrid	Central	QUICK
Barton [26]	15x8	-	-	4,00	No Convergence	3,87
Barton [26]	30x16	-	-	3,73	No Convergence	3,68
Barton [26]	40x20	-	-	3,63	No Convergence	3,65
Barton [26]	80x40	-	-	3,49	No Convergence	3,58
Barton [26]	120x50	-	-	3,50	3,56	3,58
Barton [26]	160x80	-	-	3,51	3,53	3,57
Barton [26]	200x100	-	-	3,53	3,57	3,58
Barton [26]	250x128	-	-	3,54	No Convergence	-
SIMPLER(x_L=45)	**402x62**	**3.00**	**3.14**	**3.17**	**2.99**	
SIMPLER(x_L=45)	**332x77**	**3.07**	**3.19**	**3.21**	No Convergence	
SIMPLER(x_L=45)	**281x91**	**3.14**	**-**	**3.29**	No Convergence	
SIMPLER(x_L=60)	**402x62**	**3.04**	**3.22**	**3.22**	No Convergence	
SIMPLER(x_L=60)	**332x77**	**3.17**	**3.30**	**3.23**	No Convergence	
SIMPLER(x_L=60)	**281x91**					

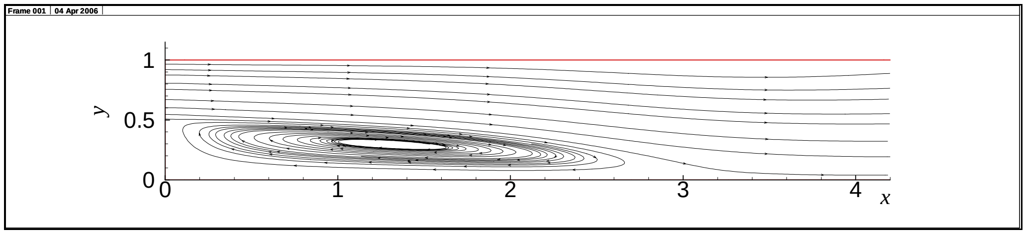

Figure 4.50 Streamlines between x=0 and x=4 for Re=300 with SIMPLER algorithm using hybrid scheme on a 402x62 mesh when x_L=45h

4.3.3.2 Results for *Re*=400

Another test case is for a Reynolds number of 400. The secondary eddy or upper recirculation region is weak but visible on the upper side of the flow. Wirogo [3] observed that the exponentional based schemes predict the separation length accurately for low Reynolds numbers (Re≤400), but detonates quickly at higher Reynolds numbers. Table 4.15 presents not only the published results, but also results obtained by SIMPLER algorithm using different schemes on different grid sizes.

When Reynolds number is 400 or above, unfortunately a converged solution can not be obtained by using central differencing scheme on a 402x62 grid, on a 332x72 gird or on a 281x91 grid when 45h or 60h is used as the length of the channel.

Moreover, it is obvious from Table 4.15 that lower reattachment lengths and upper detachment lengths obtained by SIMPLER algorithm using upwind, hybrid and power law differencing schemes are smaller than the ones presented in the literature. On the other hand, unlike results obtained by using the upwind scheme, the upper reattachment lengths obtained by using power law and hybrid schemes agrees with the results in the literature. It can be concluded that upwind schemes underestimates the lower reattachment length when compared with upper detachment length and upper reattachment length than the power law and hybrid schemes.

Furthermore, when the length of channel is increased from 45h to 60h with the same grid sizes, all schemes tends to give more acceptable separation lengths.

Results on a 332x77 grid are better than the results on a 402x62 grid for all schemes. Increasing the number of grid points in the *y*-direction increases accuracy of SIMPLER algorithm and makes it possible to decrease the number of grids in the streamwise *x*-direction from 402 to 332. Using 77 grid points in the *y*-direction is sufficient to predict lower and upper recirculation regions.

Figures 4.51 and 4.52 contain the streamline for *Re*=400 with SIMPLER method using hybrid scheme on a 62x402 mesh when x_L=60*h*.

Table 4.16 Separation lengths and locations for *Re*=400

***Re*=400**	**Grid Size**	x_1	x_4	x_5	$x_5 - x_4$
Marinova, Christov and Marinov [29]	256x64	4,3223	3,9732	5,2018	1,2286
Thompson and Ferziger [19]	512x128	4.3500	-	-	-
Wirogo [3] with FCM	102x22	4,4850	4,5607	4,8752	0,3146
Wirogo [3] with FCM	102x42	4,4741	4,4764	5,3053	0,8289
Wirogo [3] with FCM	102x82	4,4697	4,5301	5,3562	0,8261
Wirogo [3] with Power law	102x22	3,9263	3,4299	4,4740	1,0441
SIMPLER Hybrid (x_L=45)	**402x62**	**3.3868**	**2.6092**	**5.5089**	**2.8997**
SIMPLER Power Law (x_L=45)	**402x62**	**3.3650**	**2.6143**	**5.4031**	**2.7939**
SIMPLER Upwind (x_L=45)	**402x62**	**3.4642**	**2.7923**	**4.5262**	**1.7339**
SIMPLER Hybrid (x_L=60)	**402x62**	**3.6022**	**3.0280**	**5.2005**	**2.1725**
SIMPLER Power Law (x_L=60)	**402x62**	**3.7267**	**3.1093**	**5.4120**	**2.3027**
SIMPLER Upwind (x_L=60)	**402x62**				
SIMPLER Hybrid (x_L=45)	**332x77**	**3.3653**	**2.6264**	**5.1248**	**2.4984**
SIMPLER Power Law (x_L=45)	**332x77**	**3.5127**	**2.8642**	**5.2106**	**2.3464**
SIMPLER Upwind (x_L=45)	**332x77**	**3.5028**	**2.9300**	**4.7350**	**1.8050**
SIMPLER Hybrid (x_L=60)	**332x77**				
SIMPLER Power Law (x_L=60)	**332x77**				
SIMPLER Upwind (x_L=60)	**332x77**	**3.7881**	**-**	**-**	**-**

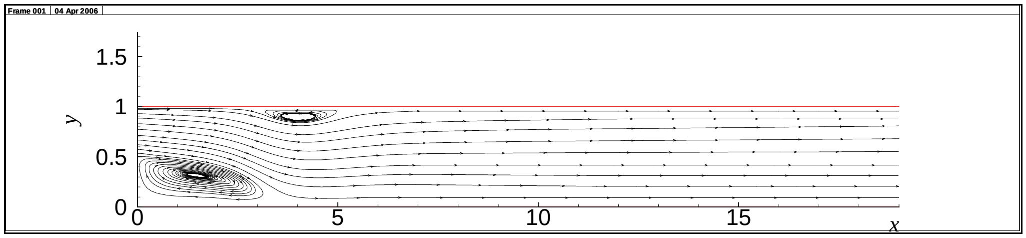

Figure 4.51 Streamlines between x=0 and x=18 for Re=400 with SIMPLER algorithm using hybrid scheme on a 402x62 mesh when x_L=60h

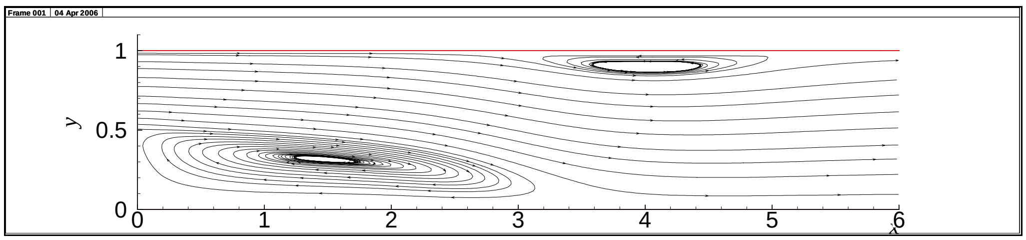

Figure 4.52 Streamlines between x=0 and x=6 for Re=400 with SIMPLER algorithm using hybrid scheme on a 402x62 mesh when x_L=60h

4.3.3.3 Results for *Re*=600

Another test case is for a Reynolds number of 600. The reattachment and separation lengths, which are estimated by SIMPLER algorithm, are presented in Table 4.17 and compared with the results in the literature. As the Reynolds number is increased to 600, estimation of upper recirculation region becomes more sensitive since it interacts with the lower reattachment length. Therefore calculation of correct x_4 is the most difficult issue.

It is obvious from Table 4.17 that all schemes yield the worst result for the lower reattachment lengths compared with the low Reynolds number case results, as shown in Tables 4.15 and 4.16.

Moreover, convergence can not be obtained with central differencing when 281x91 and 332x77 grids are used. On the other hand, when coarser grids are used, the results of Barton [26] with the central differencing scheme diverged.

Barton [26] and Wirogo [3] mentioned that hybrid scheme fails to give reliable results for even the finest grids at higher Reynolds numbers. Also this fact is confirmed in present study by using upwind, hybrid and power schemes. The results of upwind, hybrid and power law schemes are nearly match with the results in literature. However the results of upwind, hybrid and power law schemes underpredict separation lengths and locations when compared to the results in the literature that are obtained.

Unlike the test case for *Re*=400, it is observed that placing 62 grid points in the *y*-direction is not sufficient to obtain converged solutions by using hybrid and power law schemes. Therefore, at least 77 points in the *y*-direction are needed to obtain converged results. Results of separation lengths are more accurate and increased with grid refinement.

Figures 4.53 and 4.54 shows the streamline plots for *Re*=600 with SIMPLER algorithm using hybrid scheme on a 281x91 mesh when x_L=45h. The upper recirculating region is more visible at *Re*=600.

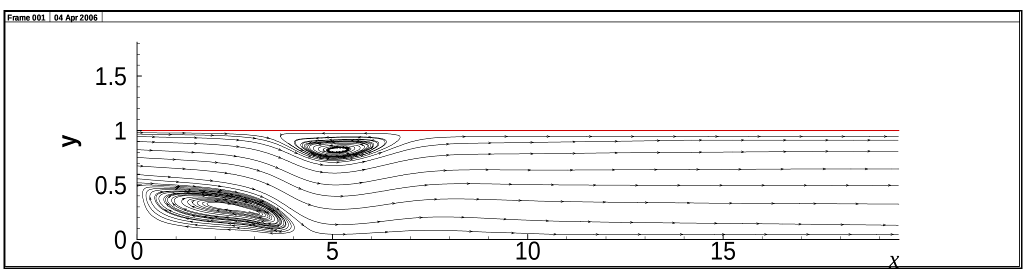

Figure 4.53 Streamlines between x=0 and x=19 for *Re*=600 with SIMPLER algorithm using hybrid scheme on a 281x91 mesh when x_L=45h

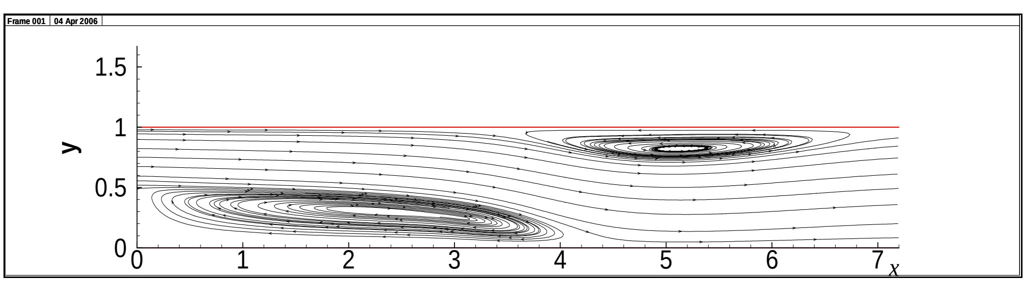

Figure 4.54 Streamlines between x=0 and x=7 for *Re*=600 with SIMPLER algorithm using hybrid scheme on a 281x91 mesh when x_L=45h

Table 4.17 Separation lengths and locations for *Re*=600

***Re*=600**	**Grid Size**	x_1	x_4	x_5	$x_5 - x_4$
Marinova, Christov and Marinov [29]	64x256	5,3703	4,3304	8,1119	3,7815
Wirogo [3] with FCM	102x22	5,7923	4,7644	8,1417	3,3773
Wirogo [3] with FCM	102x42	5,7932	4,9018	8,6215	3,7197
Wirogo [3] with FCM	102x82	5,7953	4,9761	8,7265	3,7504
Wirogo [3] with Power law	102x22	4,0659	3,1097	6,2099	3,1002
Barton [26] with Hybrid	15x8	7,1400	-	-	-
Barton [26] with Hybrid	120x50	4,7900	3,7500	7,2950	3,5450
Barton [26] with Hybrid	200x100	5,0500	4,0150	7,6950	3,6800
Barton [26] with Central	15x8	-	-	-	-
Barton [26] with Central	120x50	-	-	-	-
Barton [26] with Central	200x100	5,3600	4,3600	8,0750	3,7150
Barton [26] with QUICK	15x8	4,2300	2,0950	5,6050	3,5100
Barton [26] with QUICK	120x50	5,3300	4,2950	8,0850	3,7900
Barton [26] with QUICK	200x100	5,3350	4,3150	8,1050	3,7900
SIMPLER Hybrid (x_L=45)	**281x91**	**4.3759**	**3.5266**	**7.1775**	**3.6509**
SIMPLER Power Law (x_L=45)	**281x91**	**4.1636**	**3.5057**	**6.7281**	**3.2224**
SIMPLER Upwind (x_L=45)	**281x91**				
SIMPLER Hybrid (x_L=60)	**332x77**				
SIMPLER Power Law (x_L=60)	**332x77**				
SIMPLER Upwind (x_L=60)	**332x77**	**3.4306**	**2.8658**	**5.0768**	**2.2110**
SIMPLER Hybrid (x_L=60)	**281x91**	**3.3936**	**3.3709**	**6.3898**	**3.0189**
SIMPLER Power Law (x_L=60)	**281x91**				
SIMPLER Upwind (x_L=60)	**281x91**	**4.1900**	**3.5379**	**6.0530**	**2.5151**
SIMPLER Upwind (x_L=60)	**402x62**	**4.3509**	**2.4239**	**7.0000**	**4.5761**

4.3.3.4 Results for ***Re*=800**

Final test case is for a Reynolds number of 800. The SIMPLE methodology can only successfully produces steady-state solutions up to *Re*=800 as mentioned by Barton [27] and by other researchers. Although flow becomes unsteady and unstable at *Re*=800, many researchers attempt to obtain stable results for the steady viscous incompressible two-dimensional flow over a backward-facing step at this Reynolds number. Gartling [25] obtained accurate results with steady numerical calculations.

It is observed from steady runs that after a one or two drops in magnitude, the residuals start to fluctuate during steady calculations at this Reynolds number and these oscillations leads to development of several vortices in the channel. For this reason, it is observed that the physical problem is no longer steady. Therefore the inlet Reynolds number can not be increased above *Re*=800 in present study and obtaining converged solution using steady computations by applying SIMPLER algorithm is challenged.

Results of reattachment and separation positions, which are presented in the literature, are shown in Table 4.18 and compared with the results of the present study.

At Re=800, main channel length becomes seriously important and it should be long enough to achieve accurate results.

Even though the grids are finer, for high Reynolds number runs, obtained separation lengths have fairly large difference with results presented in the literature. Separation lengths are underpredicted by using hybrid and power law schemes. Moreover, results are diverged when upwind and central difference schemes are used in the present study.

Table 4.18 Separation lengths and locations for *Re*=800

Re=800	Grid Size	x_1	x_4	x_5	$x_5 - x_4$
Marinova, Christov and Marinov [29]	-	6,0909	4,8214	10,4719	5,6505
Wirogo [3] with FCM	102x22	6,6638	5,2651	10,5099	5,2448
Wirogo [3] with FCM	102x42	6,8324	5,5781	11,5049	5,9268
Wirogo [3] with FCM	102x82	6,8746	5,7095	11,7568	6,0473
Wirogo [3] with Power law	102x22	3,6787	2,6534	6,1692	3,5158
Gartling [25] with mesh A	6x120	5,81	4,79	10,48	5,69
Gartling [25] with mesh B	10x200	6,07	4,83	10,47	5,64
Gartling [25] with mesh C,D,E	*	6,09-6,10	4,85	10,48	5,63
Barton [27] with no entrance	-	6,015	4,82	10,48	5,66
Barton [27] with inlet channel	-	5,755	4,57	10,33	5,76
Anjorin and Barton [16] with SIMPLE	60x60	6,4860	1,6592	7,1850	5,53
Anjorin and Barton [16] with SIMPLEV	60x60	6,4915	2,4796	7,1850	4,71
Barton [26] with Hybrid - uniform	200x100	5,410	4,225	9,455	5,230
Barton [26] with Hybrid - refined	200x100	5,495	4,275	9,775	5,500
Barton [26] with QUICK	**-**	6,100	4,820	11,005	6,185
SIMPLE					
SIMPLE					
SIMPLE Hybrid					
SIMPLER Hybrid (x_L=45)	**332x77**	**2.1824**	**0.7637**	**5.4888**	**4.7251**
*mesh C=400x20, mesh D=600x30, mesh E=800x40.					

CHAPTER 5

CONCLUSIONS

5.1 Summary

In the previous chapter, first the problem of two-dimensional lid-driven square cavity, which is widely used to validate the code for the steady –state forms of the incompressible laminar Navier-Stokes equations, is considered. The flow over a backward-facing step is studied as the second benchmark case. The presented results of the two test cases in previous chapter are summarized in the following section.

5.1.1 Flow Characteristics of the Test Problem 1

Lid driven cavity, which is the first test case problem, is solved for Reynolds number ranging from 100 to 10000. First, the graphs of horizontal and vertical velocity along the centerlines are illustrated. Then the vortex center locations are presented and compared with reference results quantitatively. The strength of primary, secondary and tertiary vortices are shown by representing streamlines in the Figures. Finally solutions on clustered meshes are compared with the results on uniform grids and number of iterations is tabulated.

Results obtained by using power law and hybrid schemes give better results than the upwind differencing scheme for both SIMPLE and SIMPLER algorithms, which can be seen from the results at Reynolds numbers of 100,400 and 1000 since the power law and hybrid differencing schemes possess second order accuracy, whereas upwind differencing scheme have first order accuracy

When the centerline velocity profiles are examined, results obtained by the SIMPLER algorithm using a 129x129 grid for *Re*=100, a 161x161 grid for *Re*=400 and 100, 257x257 grid for *Re*=5000 are perfectly match with Ghia's [8] results. However SIMPLER solution for the centerline velocity profiles at *Re*=10000 deviates from Ghia's [8] solution. In the case of SIMPLE algorithm, solutions using a 161x161 grid for *Re*=100 and 257x257 grid for *Re*=400 and 1000 are in good agreement with Ghia's [8] solution. However, for larger values of the Reynolds numbers ranging from 5000 to 10000, results of SIMPLE algorithm gives incorrect but converged solutions.

It is concluded that our steady-state solutions with both methods deviates considerable from the reference solutions for the centerline velocity profiles at *Re*=10000. This Reynolds number is the limiting Reynolds number at which translation from laminar to turbulence occurs because of the formation of the vortices at the corners of the square cavity. Although unsteady calculations of Wirogo [3] can lead to satisfactory converged results, steady-state numerical calculations will result in very slow convergence and the magnitude of residual drops only a few orders [3]. The simulation of the transient behavior of flow using steady calculations causes oscillations in residuals. Since the problem becomes unsteady, the unsteady solutions are able to handle the transient nature of the flow. For $Re \geq 5000$ the loss stability for the steady solution is observed.

For Reynolds number 1000, the flow is not actually unsteady, whereas flow is transient at the initial formation period of the primary vortex. Then after the development of primary vortex steady-state solution can be achieved for *Re*=1000.

The unsteady flow inside the lid-driven cavity starts for large Reynolds numbers of 5000 and 1000. For large Reynolds numbers, the grid Peclet number in the main flow direction is generally much larger than unity. Moreover exponential based schemes (i.e. Power Law, hybrid) are more convective and neglects diffusion for transient problems. For this reason, the Power Law and Hybrid schemes are not usually used for unsteady flow calculation [3].

The nature of the vortices formed in the cavity depends on the Reynolds number. The location of the centers of the primary, secondary and tertiary vortices in a square cavity are tabulated in the previous chapter for *Re*=100, 400, 1000, 5000 and 10000. Most of the strength is concentrated on the primary vortex in the middle of the cavity. It is shown in Figure 5.1 that as the Reynolds number increases from 100 to 5000, the primary vortex moves downstream and toward the geometric center of the cavity considerably. However, with further increases in the Reynolds number from 5000 to 10000, the center location of the primary vortex becomes virtually invariant. The center of location of the primary vortex calculated by SIMPLER and SIMPLE algorithms exhibit perfect match with the reference results at *Re*=100, 400 and 1000. However, only the location of the center of the primary vortex calculated by SIMPLER algorithm at *Re*=5000 is in good agreement with reference data. On the other hand, at a Reynolds number of 10000, both methods deviate considerably from the reference results.

The formation, position and strength of small counter rotating vortices having a smaller strength at the top left, bottom right and left corner of the cavity also depend on the Reynolds number. Burgess [5] noted that unlike primary vortex which occurs by the development of inviscid core of the flow, the secondary and tertiary vortices are viscosity-dominated. The vortices in the bottom right and left corners appear for *Re*≈100, whereas the vortex at the bottom right is less intensive than the vortex at the bottom left. The locations of center of the secondary vortex in the bottom right corner at *Re*=100, 400, 1000, 5000 and 10000 are shown in Figure 5.2. The center of locations of the secondary vortex at bottom left corner is presented in Figure 5.3. The strengths of secondary vortices at the bottom right and left increase by increasing Reynolds number. As Reynolds number is increased, the center of the secondary vortex at bottom right corner moves towards left. In contrast, center of the secondary vortex at bottom left goes up with an increase in the Reynolds number.

If the secondary vortex at top left corner and tertiary vortices are considered, they are not visible for Reynolds numbers of 100, 400 and 1000. When the Reynolds number increased to 5000, except the tertiary vortex at bottom left, the secondary vortex at top left corner and the tertiary vortex at bottom right become quite visible and gain a significant size for $Re \geq 7500$. Tertiary vortex at the bottom right is observed at $Re=10000$.

The data provided for location of the center of the secondary and tertiary vortices are provided for $100 \leq Re \leq 10000$. The results in the literature are compared with the results of presented study. It is clear from the Tables presenting the location of the center of the secondary and tertiary vortices that the results of SIMPLER algorithm are in good arrangement with reference results up to a Reynolds number 10000. However, the results of SIMPLE method start to deviate from reference results when $Re \geq 5000$.

Clustering mesh near the solid boundaries does not alter the converged results but decreases the number of numerical iterations since the secondary vortices at left and right bottom corners are small in size at Reynolds numbers of 100 and 400. However, when Reynolds number is increased to 1000, clustered meshes does not affect the number of iterations. Therefore, instead of using uniform meshes, using clustered meshes for Reynolds numbers up to 1000 is effective in decreasing the computational load. Moreover, to obtain converged solutions for larger Reynolds number requires larger number of iterations as expected.

The computational time for each iteration in the SIMPLER algorithm is larger than the SIMPLE algorithm, since it is expected that one step of the SIMPLER algorithm requires more calculations than the one step of SIMPLE algorithm.

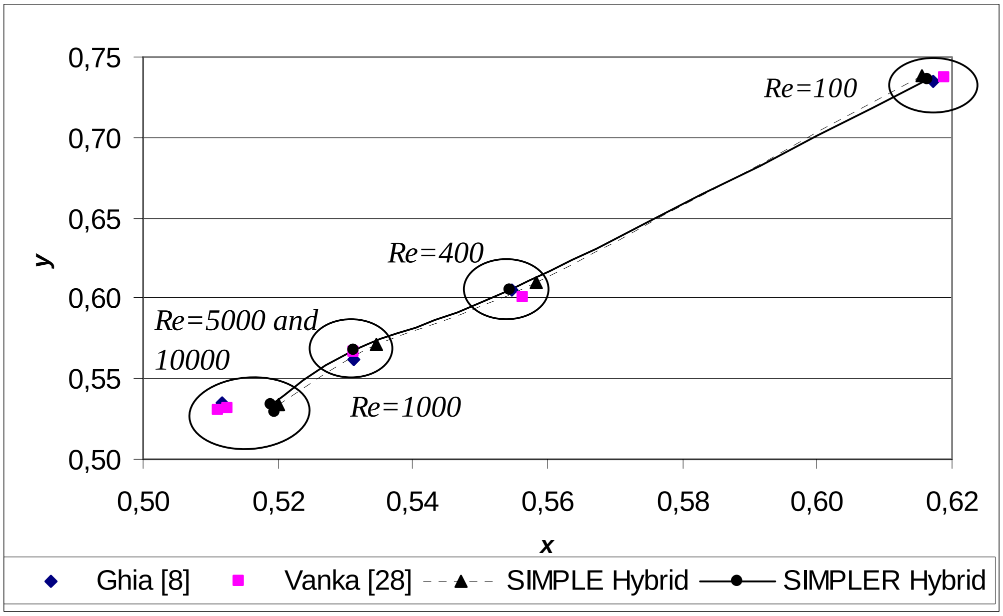

Figure 5.1 Variation of locations of the Primary Vortex Center with Reynolds number

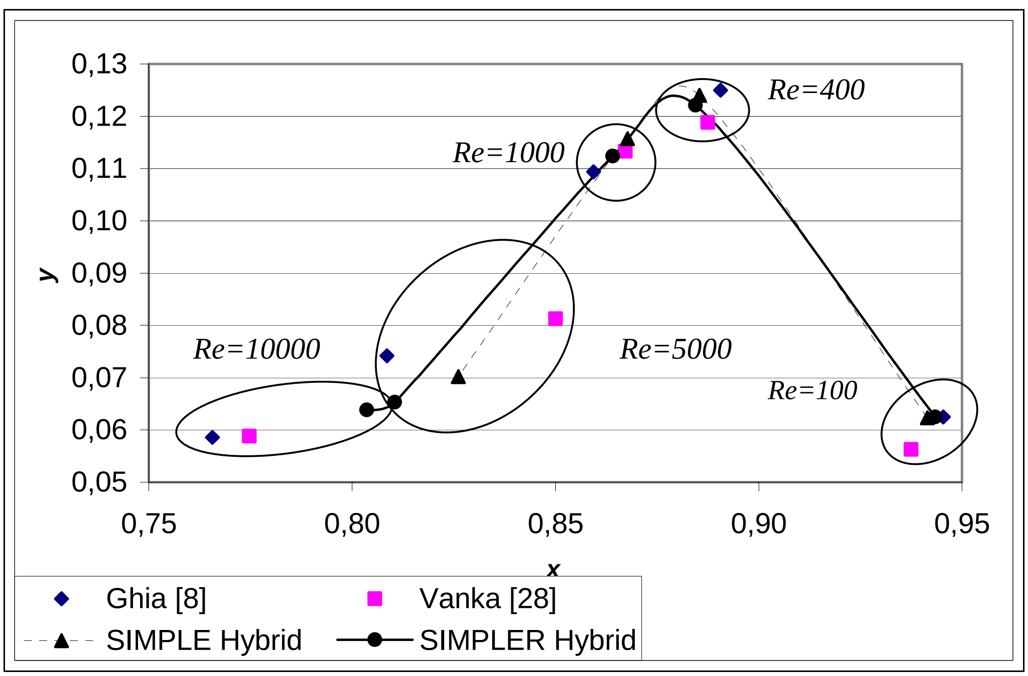

Figure 5.2 Variation of locations of the Bottom-Right Secondary Vortex Center with Reynolds number

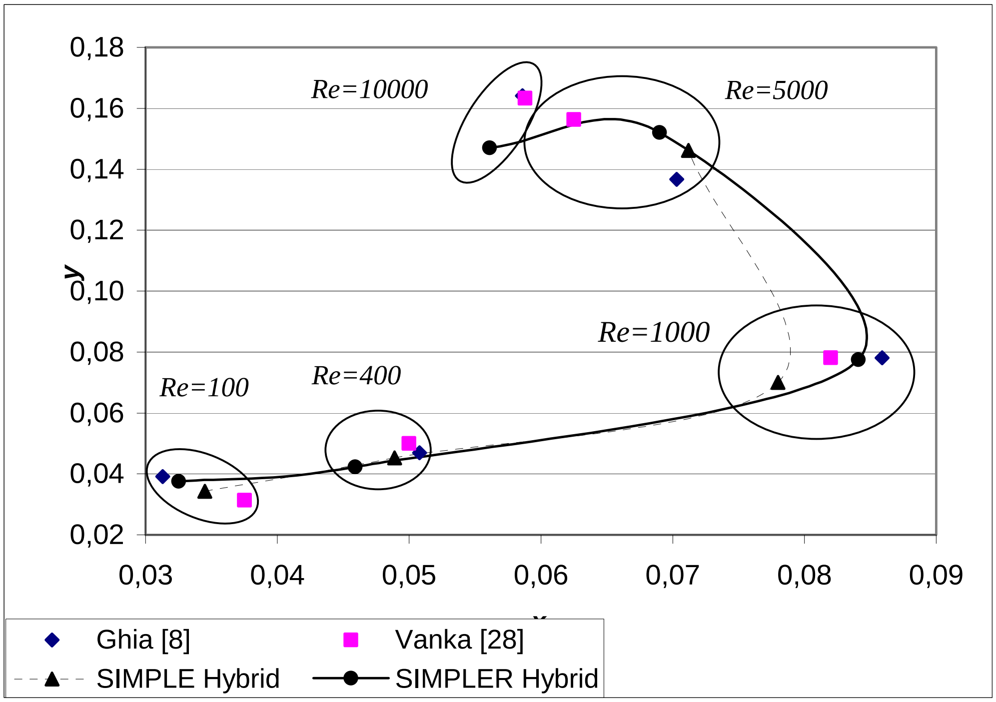

Figure 5.3 Variation of locations of the Bottom-Left Secondary Vortex Center with Reynolds number

5.1.2 Flow Characteristics of the Test Problem 2

The second test problem, used in the previous chapter, is the flow over a backward facing step. The study focused on the numerical solution of the steady laminar flow over a backward-facing step.

The lower reattachment, upper detachment and upper reattachment lengths are tabulated for Reynolds numbers of 300, 400, 600 and 800 and compared with the results in the literature. In the figures not only streamlines of converged solutions are plotted, but also upper and lower eddies are illustrated.

Results of SIMPLER algorithm by using central differencing scheme only converge at Reynolds number 300 for finer grids. Upwind scheme converges for $Re \leq 600$ but fails to give accurate results. Separation lengths obtained by using upwind schemes is worse than the results obtained by using the hybrid and power law differencing schemes. Hybrid and power law differencing schemes are closer to the results in the literature for low Reynolds numbers. However, as the Reynolds number is increased, results of these schemes fail to give accurate results. Results of the all schemes underpredict the reattachment and separation lengths.

More accurate results are obtained not only when the length of the channel is increased from 45*h* to 60*h* but also, the number of grid points in the *y*-direction is increased until a grid-independent solution is obtained.

Figure 5.4 presents the variation of lower reattachment length with Reynolds number. Although the results of Barton [26] with QUICK scheme and Marinova, Christov and Marinov [29] are in good arrangement, Wirogo [3] over-predicted the lower reattachment length. In the present study and the result of Barton [26] with Hybrid scheme under-predict the lower reattachment length. Lower reattachment length increases with the increasing Reynolds number. Furthermore, when the Reynolds number is increased, the presented results for lower reattachment lengths in Figure 5.4 deviates from each other.

In addition to this, the variation of the upper detachment length and reattachment length of upper eddy with the Reynolds number is illustrated in Figures 5.5 and 5.6, respectively. Like the results of lower reattachment length, results of Barton [26] with QUICK scheme and Marinova, Christov and Marinov [29] for the variation of the upper detachment and reattachment lengths are perfectly matched with each other. On the other hand, results of Barton [26] and the present study, both using hybrid scheme, underestimate the upper detachment and upper reattachment lengths. However Wirogo [3] over-predicts these lengths by using FCM method on a 102x42 grid. The slope of the variation of upper reattachment lengths in the presented results is almost constant.

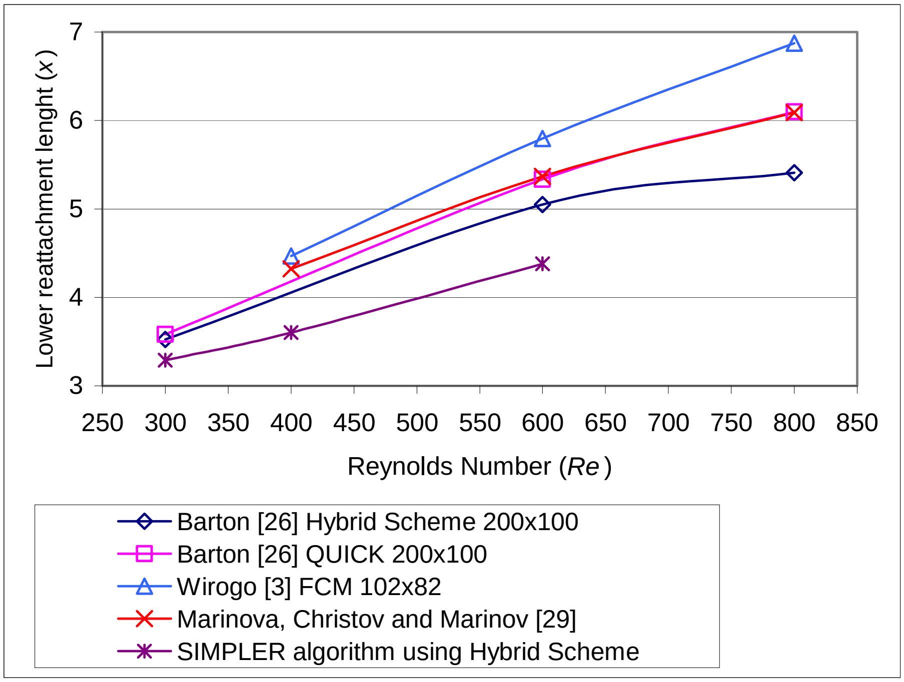

Figure 5.4 Variation in lower reattachment lengths with Reynolds number

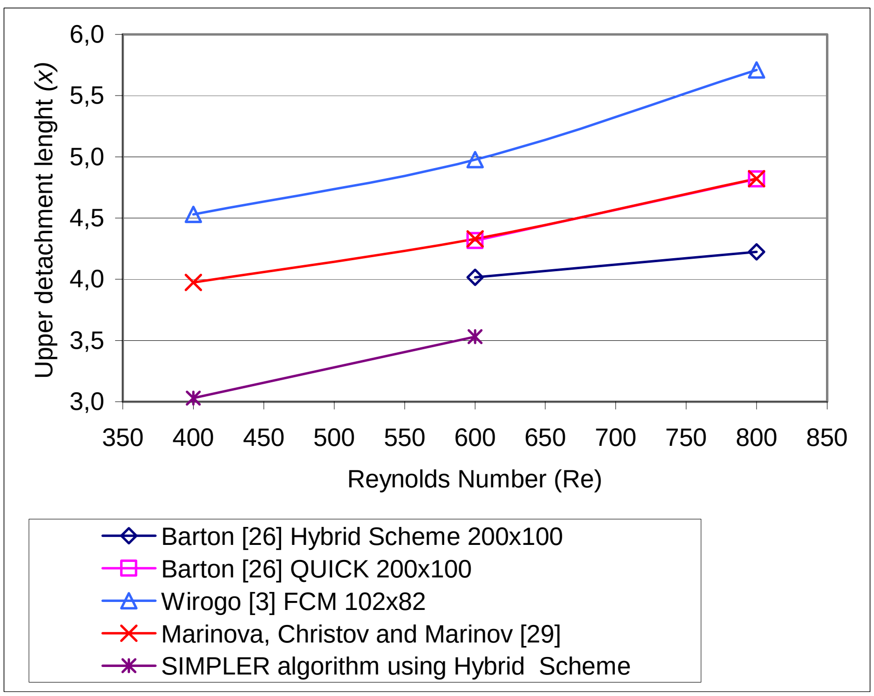

Figure 5.5 Variation in upper detachment lengths with Reynolds number

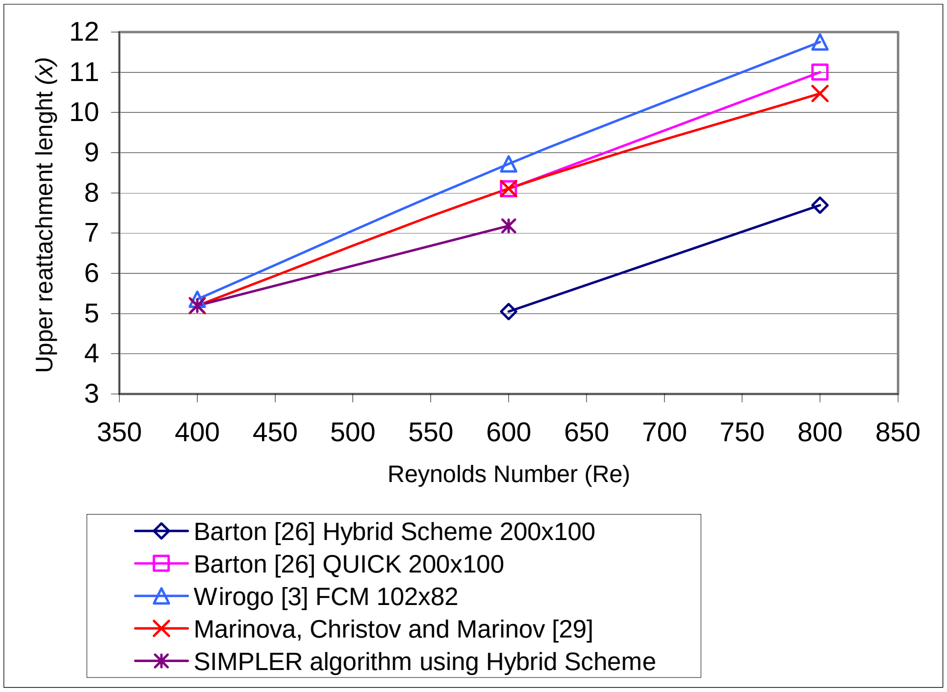

Figure 5.6 Variation in upper reattachment lengths with Reynolds number

The upper eddy is visible when $Re \geq 400$ and slows down the growth of the lower reattachment length when $Re \geq 600$. The slope of the variation of the lower reattachment length with the Reynolds number is smaller when $Re \geq 600$.

For the backward-facing flows, the reattachment length increases until the start of transition. The transition and unsteady flow can be defined by the observation of more than one eddy behind the step. This is the result of decreasing diffusive length scale with increasing Reynolds number [18]. On the other hand, diffusion is more at low Reynolds number that small eddies are rapidly dissipated by the action of viscosity [18].

5.2 Conclusion

In this thesis, a FORTRAN code is prepared and used for solving steady incompressible laminar Navier-Stokes equations. The SIMPLE and SIMPLER algorithms, which are based on the primitive variable approach, are used in this study. The two-dimensional flow in a lid-driven cavity and the two-dimensional backward-facing step are chosen to validate the accuracy of the algorithms. For low Reynolds numbers, flow is laminar in both test cases. However, these problems can be highly transient and unsteady for high Reynolds numbers.

SIMPLER algorithm is more accurate than SIMPLE algorithm for estimating not only steady flows but also unsteady flows especially in the recirculating regions of lid-driven cavity problem. SIMPLE algorithm is not effective when the translation is perceived.

Hybrid and power law differencing schemes give better results than the upwind and central differencing schemes in general. The SIMPLE and SIMPLER algorithms by using upwind scheme tend to fail when Re≥5000 in the lid-driven cavity problem. The SIMPLER algorithm by using the central-differencing scheme diverges in backward-facing step problem when Re≥400. The SIMPLER method by using hybrid and power law differencing schemes are sufficient to obtain accurate results for lid-driven cavity problem for Reynolds numbers ranging from 100 to 10000. Although the SIMPLER method by using hybrid and power law differencing schemes also give acceptable results for low Reynolds numbers in the backward-facing step problem when finer grids are used, these schemes fail to give accurate results even for the finest grids. Therefore, higher order differencing schemes, such as QUICK scheme, should be used in SIMPLER method for high Reynolds numbers in the backward-facing step problem. Using highly accurate schemes may increase the computational time but can increase the accuracy of the results at high Reynolds numbers. It is state in many researches that higher order schemes are more efficient in the solution of transient flow problems.

It is observed that the finer grids are used to obtain accurate results in the backward-facing problem. On the other hand, grid independent solutions are obtained for lid-driven cavity according to Reynolds number and algorithm. The SIMPLER algorithm is grid independent on smaller size meshes than the SIMPLE algorithm. For example, the solution with SIMPLER algorithm becomes grid independent at Re=1000 when the grid size is nearly 161x161. However, with SIMPLE method, solution becomes grid independent on a 257x257 grid at the same Reynolds number. Also grid clustering reduces the computational effort up to a Reynolds number of 1000 in the lid-driven cavity problem.

In addition to this, unlike the lid-driven cavity problem in which grids are clustered in all coordinate directions since recirculation occurs at the corners, refining grid size in y-direction is sufficient for the backward-facing problem since u-velocity profiles is most sensitive to Δy variations. Furthermore, applying local grid stretching to the inlet region of the backward-facing problem reduces the computational cost and save CPU time. Although the rate of convergence depends on the nature of the test problem, physical properties of the flow and differencing schemes, all differencing schemes seem to converge reference results as the mesh is refined.

One or two order of decrease of the residuals in the SIMPLE algorithm is faster than the SIMPLER algorithm for low Reynolds number since the methodology of correction of velocities in both algorithms are different. However, efficiency of the SIMPLE algorithm reduces not only for high Reynolds numbers but also when dropping the residuals order more than two is desired.

For high Reynolds numbers and for larger grid systems, the efficiency of the SIMPLER and SIMPLE algorithms reduces considerably. Also the choice of under-relaxation factors alters the number of iterations to achieve a converged solution for both algorithms.

5.3 Recommendations for the Results

Finally, the recommendations can be discussed to improve the present study.

Higher order schemes can be applied to not only to the SIMPLE algorithm but also to its variants.

Outlet boundary conditions can be treated more accurately in order to increase the efficiency of the solution in the backward-facing step.

Local grid clustering can used in backward-facing step problem to reduce computational load while increasing the efficiency of algorithms.

Calculations in the present study are obtained for Reynolds numbers up to translation from the laminar to turbulent flow. Therefore, turbulence model can added to predict the turbulent flow. Also steady solutions are captured in this study. By altering the equations to unsteady forms, unsteady flow solver can be used to solve this two benchmark test problems.

Finally, performance of the SIMPLE algorithms and its variants on lid-driven cavity flow problem and on backward-facing step problem by using an unstructured grid can be considered to evaluate the ability of algorithms.

REFERENCES

[1] Malalasekera W., and Versteeg H. K., “An Introduction to Computational Fluid Dynamics The Finite Volume Method”, Pearson Education Limited, Harlow, England, 1995.

[2] Patankar S. V., “Numerical Heat Transfer and Fluid Flow”, Hemisphere Publishing Corporation, New York, 1980.

[3] Wirogo S., “Flux Corrected Method An Accurate Approach to Fluid Flow Modeling”, Ph.D. Thesis, Department of Aerospace Engineering, Iowa State University, 1997.

[4] Gupta M.M. and Kalita C.J., “A New Paradigm for Solving Navier-Stokes Equations: Streamfunciton-Velocity Formulation”, Journal of Computational Physics, 207, 52-68, January 2005.

[5] Burggraf R.O., “Analytical and Numerical Studies of the Structure of Steady Seperated Flows ”, Journal of Fluid Mechanics, 24, Part 1, 113-151, 1966.

[6] Bozeman D.J., “Numerical Study of Viscous Flow in Cavity”, Journal of Computational Physics, 12, 348-363, 1979.

[7] Schreiber R. and Keller H.B., “Driven Cavity Flows by Efficient Numerical Techniques”, Journal of Computational Physics, 49, 310-333, 1983.

[8] Ghia U., Ghia K.N. and Shin C.T., “High Re Solutions for Incompressible Flow Using the Navier-Stokes Equations and a Multigrid Method”, Journal of Computational Physics, 48, 387-411, 1982.

[9] Chorin A.J.,“A Numerical Method for Solving Incompressible Viscous Flow Problems”, Journal of Computational Physics, 2, 12-26, 1967.

[10] Soh W.Y.,“Time-Marching Solution of Incompressible Navier-Stokes Equations for Internal Flow”, Journal of Computational Physics, 70, 232-252, 1987.

[11] Harlow F.H. and Welch J.E., “Numerical Calculation of Time-Dependent Viscous Incompressible Flow with Free Surface”, Physics of Fluid, 18, 2182-2184, 1965.

[12] Chorin A.J., Mathematical Computation, 22, 727, 1968.

[13] Leonard B.P. and Mokhtari S., “Beyond first-order Upwinding: The Ultra Sharp Alternative for Non-oscillatory Steady-State simulation of Convection”, International Journal for Numerical Methods in Engineering, 90, 729, 1990.

[14] Leonard B.P., “A Stable and Accurate Convective Modeling Procedure Based On Quadratic Upstream Interpolation”, Computer Methods in Applied Mechanics and Engineering, 19, 59-98, 1979.

[15] Hayase T., Humphrey J.A.C. and Greif R., “A Consistently formulated QUICK Scheme for Fast and Stable Convergence Using Finite Volume Iterative Calculation Procedures”, Journal of Computational Physics, 98, 108-118, 1992.

[16] Anjorin A.O.V. and Barton I.E., ”Removal of Temporal and Under-Relaxation Terms from the Pressure-Correction Equation of the SIMPLE Algorithm”, International Journal of Fluid Dynamics, 5, 59-75, 2001.

[17] Lund University of Technology home page url: "http://www.vok.lth.se/", last access date: March 2006.

[18] Huser A. and Biringen S., "Calculation of the Two-dimensional Shear-Driven cavity Flows at High Reynolds number", International Journal of Numerical Methods in Fluids, 14, 1087-1109, 1992.

[19] Thompson C.M and Ferziger J.H., "An Adaptive Multigrid Technique for the Incompressible Navier-Stokes Equations", Journal of Computational Physics, 82, 94-121, 1989.

[20] Bruneau C.H. and Jouron C., "An Efficient Scheme for Solving Steady Incompressible Navier-Stokes Equations", Journal of Computational Physics, 89, 389-413, 1990.

[21] Gjestal T. and Lossius M.E.H., "Comparison of Pressure Correction Smoothers for Multigrid solutions of Imcompressible Flow", Christian Michelsen Researh AS, June 17, 1990.

[22] Kim J. and Moin P., "Application of A Fractional-Step Method to Incompressible Navier-Stokes Equations", Journal of Computational Physics, 59, 308-323, 1985.

[23] Armaly Gjestal T. and Lossius M.E.H., "Comparison of Pressure Correction Smoothers for Multigrid solutions of Imcompressible Flow", Christian Michelsen Researh AS, June 17, 1990.

[24] Hackman l.P., Raithby G.D. and Strong A.B.,"Numerical Predictions of Flows Over Backward-Facing Steps", International Journal for Numerical Methods in Fluids, 4, 711-724, 1984.

[25] Gartling D.K.,“A Test Problem for Outflow Boundary Conditions – Flow Over A Backward-Facing Step”, International Journal for Numerical Methods in Fluids, 11, 953-967, 1990.

[26] Barton I.E., ”A Numerical Study of Flow Over A Confined Backward-Facing Step”, International Journal for Numerical Methods in Fluids, 21, 653-665, 1995.

[27] Barton I.E., ”The Entrance Effect of Laminar Flow Over A Confined Backward-Facing Step Geometry”, International Journal for Numerical Methods in Fluids, 25, 633-644, 1997.

[28] Vanka S.P., “Block-Implicit Multigrid Solution of Navier-Stokes Equations In Primitive Variavles”, Journal of Computational Physics, 65, 138-158, 1986.

[29] Marinova R.S., Christov C.I. and Marinov T.T., “A Fully Solver for Incompressible Navier-Stokes Equations Using Operator Splitting ”.

[30] Hou S., Zou Q., Chen G., Doolen G. and Cogley A., “Simulation of Cavity Flows by The Lattice Boltzmann Method”, Journal of Computational Physics, 118, 329-347, 1995.

[31] Barragy E. and Carey G.F., “Streamfunction-Vorticity Driven Cavity Solution Using *p* Finite Elements”, Computational Fluids, 26, 453-468, 1997.

[32] Bye J.A.T.,”Numerical Solutions of The Steady-State Vorticity Equation in Rectangular Basins”, Journal of Fluid Dynamics, 26, 577-598, 1966.

[33] Kumagai M., “A Numerical Study of Wind-Driven Circulation in Rectangular Cavities”, Journal of Computational Physics, 47, 130-145, 1982.